ABSTRACT

Title of Dissertation: Photon-Mediated Interactions
in Lattices of
Coplanar Waveguide Resonators

Maya Amouzegar
Doctor of Philosophy, 2024

Dissertation Directed by: Professor Alicia Kollár
Department of Physics

Circuit quantum electrodynamics (circuit QED) has become one of the main platforms for quantum simulation and computation. One of its notable advantages is its ability to facilitate the study of new regimes of light-matter interactions. This is achieved due to the native strong coupling between superconducting qubits and microwave resonators, and the ability to lithographically define a large variety of resonant microwave structures, for example, photonic crystals. Such geometries allow the implementation of novel forms of photon-mediated qubit-qubit interaction, cross-Kerr qubit-mediated interactions, and studies of many-body physics. In this dissertation, I will show how coplanar waveguide (CPW) lattices can be used to create engineered photon-mediated interactions between superconducting qubits. I will discuss the design and fabrication of a quasi one-dimensional lattice of CPW resonators with unconventional bands, such as gapped and ungapped flat bands. I will then present experimental data characterizing photon-mediated interactions between tunable transmon qubits and qubit-mediated non-linear photon-photon in-

teractions in the said lattice. Our results indicate the realization of unconventional photon-photon interactions and qubit-qubit interactions, therefore, demonstrating the utility of this platform for probing novel interactions between qubits and photons. In future design iterations, one can extend the study of these interactions to two-dimensional flat and hyperbolic lattices.

Photon-Mediated Interactions in Lattices of Coplanar Waveguide Resonators

by

Maya Amouzegar

Dissertation submitted to the Faculty of the Graduate School of the
University of Maryland, College Park in partial fulfillment
of the requirements for the degree of
Doctor of Philosophy
2024

Advisory Committee:
 Professor Alicia Kollár (Chair/Advisor)
 Professor Mohammad Hafezi (Dean's Representative)
 Professor Sarah Eno
 Professor Steven Rolston
 Professor Trey (James V.) Porto

Dedication

To the memory of Gholamali Tajbakhsh and Simin Dokht Lotfi-Tajbakhsh.

Acknowledgments

I would like to express my gratitude to all those who were by my side during my journey as a PhD student. This work would not have been possible without their support. While I cannot list everyone here, I am grateful to every single person who encouraged and supported me.

First of all, I would like to thank my PhD advisor, Professor Alicia Kollár, for dedicating the time to train and mentor me. I had a wonderful experience in her lab, even in the early days of the COVID-19 pandemic when physical presence on campus was restricted. I will always remember our daily COVID-19-era Zoom meetings that taught me so much. She is a caring mentor, and an amazing scientist. I am very fortunate to have worked with and learned from her.

I thank my committee members, Professors Alicia Kollár, Sarah Eno, Steven Rolston, Trey Porto, and Mohammad Hafezi. Their invaluable advice and feedback are deeply appreciated. I will always cherish what I learned from them during this process.

I would not have been able to do this without the help and mentorship of my undergraduate research advisor, Professor Sarah Eno, with which she was always generous. I was first exposed to scientific research outside of classrooms in her lab, and found the joy of experimental work.

I would also like to thank my colleagues, Martin Ritter, Sandesh Kalantre, Kellen O'Brien, Zhiyin Tu, Ibukunoluwa Adisa, Won Chan Lee, Ben Cochran, Theo Gifford, and Jeffrey Wack for their support and friendship. I enjoyed working with and learning from every one of them. Martin and I (once referred to as M&M by Professor Andrew Houck) spent months building up

the lab, some of which were during the early days of the COVID-19 pandemic. We made a great team, which made graduate school all the more enjoyable, and I am grateful for that.

The work presented in this dissertation is the result of hard work in a collaborative environment. The design and simulation of the lattice and qubits were done by Alicia Kollár and Maya Amouzegar. Developing recipes for device fabrication and performing fabrication was done by Maya Amouzegar. Programming of measurement instruments and developing control codes was done by Martin Ritter. Data presented from the lattice device was collected by Kellen O'Brien and Maya Amouzegar. Analysis of measurement data was done by Maya Amouzegar, Alicia Kollár, Kellen O'Brien, and Won Chan Lee. The cross-Kerr calculation was performed by Alexey Gorshkov, Ali Fahimniya, and Alexandra Behne. The cross-Kerr data was collected by Kellen O'Brien and Won Chan Lee. Jeffrey Wack and Theo Gifford performed simulations testing the effect of resonator shapes on frequency. I appreciate the hard work of every person contributing to this project.

I specifically am grateful to Kellen and Ali. Kellen and I spent spent a lot of time collecting data together. He is brilliant and dedicated, and working with him was a true joy. Ali always patiently discusses theoretical aspects of this work with me. He is generous with sharing his knowledge of condensed matter physics and quantum optics.

I appreciate the help of FabLab staff at the UMD Nanocenter. John Abrahams and Dr. Nam Kim kindly advised me on fabrication issues and patiently trained me on various instruments. The fabrication aspect of this work would not have been possible without their insight.

I would like to thank the Graduate School Writing Center at UMD, and especially Dr. Linda Macrí, for the support and resources with which they provide graduate students. Their guidance has been essential in shaping the clarity and coherence of this dissertation.

I would like to acknowledge and extend my gratitude to my parents, Marjan Tajbakhsh and Fred Amouzegar, without whom I would not have been able to reach this stage of my career. Their unconditional love and support are beyond anything for which I could have asked. They encouraged my curiosity as a child and provided me with the best education possible.

I thank my husband, Alireza Seif, for his love, encouragement, and patience. I could not imagine completing this journey without him by my side. He helped me grow as a person and scientist, and never doubted me. His knowledge of physics, quantum computing, and cooking helped me get through some difficult days. I also appreciate our cat, Eevee Amouzegar, for the emotional support she provided throughout college and graduate school.

I am grateful for my siblings, grandparents, and friends. Their unwavering encouragement has always been a source of strength. I am very fortunate for having such a strong support system.

Table of Contents

List of Figures

List of Abbreviations

BCS	Bardeen-Cooper-Schreiffer
BF	Blue Fors
CPB	Cooper-Pair Box
CPW	Coplanar Waveguide
CW	Continuous Wave
FBL	Flux Bias Line
HEMT	High Mobility Electron Transistor
LO	Local Oscillator
PCB	Printed Circuit Board
QED	Quantum Electrodynamics
QHO	Quantum Harmonic Oscillator
QND	Quantum Non-Demolition
RF	Radio Frequency
RT	Room Temperature
RWA	Rotating Wave Approximation
SEM	Scanning Electron Microscope
SQUID	Superconducting Quantum Interference Device
TAMI	Toluene, Acetone, Methanol, Isopropanol
VNA	Vector Network Analyzer
JQI	Joint Quantum Institute
UMD	University of Maryland

List of Symbols

α	Anharmonicity
c	Lattice Constant
C_c	Coupling Capacitance
C_g	Gate Charge
Δ	Detuning between Cavity and Qubit Frequencies, $\omega_q - \omega_r$
Δ_s	Superconducting Energy Gap
ϵ_{eff}	Effective Permittivity
$\hat{\varphi}$	Generalized Flux Coordinate, Reduced Flux
$\hat{n}$	Generalized Charge Coordinate, Reduced Charge
$\hbar$	Planck Constant
κ	Cavity Decay Rate
ω_d	Semi-Classical Drive Frequency
ω_q	Qubit Frequency
ω_r	Cavity Frequency
Ω_r	Rabi Frequency
$\sigma_x, \sigma_y, \sigma_z$	Pauli X, Y, and Z Matrices
$a^\dagger, a$	Photon Creation and Annihilation Operators
$b^\dagger, b$	Atom Raising and Lowering Operators
C_Σ	Total Effective Capacitance of Transmon
C_g	Gate Capacitance
E_C	Charging Energy
E_J	Josephson Energy
g	Interaction Rate (Coupling) between Cavity and Qubit
H_{int}	Interaction Hamiltonian between Cavity and Qubit
H_{JC}	Jaynes-Cummings Hamiltonian
R_n	Resistance Across a Junction in Normal State of the Metal
t	Hopping Rate
T_1	Qubit Relaxation Time
T_2	Qubit Transverse Relaxation or Dephasing time
T_φ	Qubit Pure Dephasing Time
T_c	Critical Temperature of a Superconductor
χ	Cavity Shift Depending on Qubit State, or Cross-Kerr Coefficient

Chapter 1:   Introduction

Quantum simulations emerge as a promising tool for studying and solving complex problems across various domains, from materials science to quantum chemistry [1]. These applications promise an exciting future, supported by a deeper understanding of the quantum nature of our universe. For instance, the interaction between light and matter forms an essential aspect of quantum simulations [2].

Superconducting circuits offer a practical platform for conducting these simulations [3]. Notably, it has been observed that two qubits, when coupled to a photonic mode, can exchange second-order virtual interactions through photons [4]. Furthermore, lattices of coplanar waveguide (CPW) resonators provide a natural framework for realizing artificial photonic materials in the tight-binding limit [5]. These lattices provide the freedom to design various geometries with unconventional unit cells [6, 7]. When coupled to qubits, CPW resonator lattices facilitate the emergence of rich interacting physics, such as the formation of photonic bound states [8–10].

1.1   Structure

We would like to build the foundation necessary to study light-matter interactions in a quasi one-dimensional lattice of resonators coupled to multiple qubits. To do so, we start by deriving the Jaynes-Cumming Hamiltonian in Ch. 2 [11–13]. This Hamiltonian, which is valid across

several platforms, describes a system comprised of a single atom and a cavity mode coupled to each other. We explore the dispersive limit of the Jaynes-Cumming Hamiltonian mathematically, which is essential to performing quantum non-demolition (QND) measurements [14].

As we are interested in studying systems with multiple cavities, we look at band structures in Sec. 2.3. When multiple cavities are coupled to one another to form a lattice, they create a band structure [15]. Lattices enable the study of interactions between atoms and photons through the band structure. One phenomenon that emerges in such systems is the photonic bound state, explained in Sec. 2.4 [8, 10]. We first study the emergence of a bound state for a single qubit coupled to a lattice. We then show that multiple qubits coupled to a lattice may result in interacting bound states [16, 17].

In Sec. 2.5, we study higher order and non-linear interactions in systems with multiple photonic modes. These interactions, which are caused by Kerr non-linearities, can facilitate qubit-mediated photon-photon interactions [18].

Since the experiment described in this work is performed on superconducting circuits, we use Ch. 3 to introduce the building blocks of our systems. Sec. 3.1 starts by formulating coplanar waveguide (CPW) resonators as LC oscillators [19]. These resonators carry photonic modes, and form the "light" part of light-matter interactions. As for "matter", we introduce the transmon qubit in Sec. 3.2. The transmon is approximately a two-level system, and acts as an artificial atom [20].

Once we are familiar with the transmon and CPW resonators, we use Sec. 3.3 to formulate the coupling between them and calculate its value as a function of the resonator and qubit frequency. We then calculate the rate of photon hopping between CPW resonators in a lattice in Sec. 3.4.

After being familiarized with the components used in quantum superconducting circuits, we explore the apparatus in Ch. 4. We explain the general framework for device fabrication in Sec. 4.1. We then look at the setup for the dilution refrigerator in Sec. 4.2. The dilution refrigerator is the piece of equipment which cools devices down to low temperatures, well below the critical superconducting temperature of the metals used in our circuits. The dilution refrigerator allows the operation of superconducting circuits in temperatures that minimize the number of thermal photons.

In Sec. 4.3 we introduce the standard microwave measurement setup used for characterizing superconducting qubit devices. In this section, we describe two main types of measurements: continuous wave (CW) and pulsed measurements. In Sec. 4.4, we take note of the amplifiers and filters used in our measurements.

Armed with the information in preceding chapters, we move onto Ch. 5, where we present the quasi one-dimensional lattice, which we designed, fabricated, and characterized. In Sec. 5.1 we explain the design of the device and the considerations that had to be made in order to optimize the design. In Sec. 5.2 we review the theory underlying the device. Lastly, in Sec. 5.3, we present data collected from the lattice device introduced in this work. This data includes transmission of photonic modes, their interactions with qubits, qubit-mediated photon-photon interactions, and photon-mediated qubit-qubit interactions. Through the data, we show that this device is an appropriate prototype for studying such interactions.

Finally, in Ch. 6 we summarize this work and explain the next steps and possible future devices that are of interest. More complex lattices can be made to study qubit-qubit interactions in two-dimensions, and possibly non-Euclidean spaces.

Chapter 2:   Theory Background

This chapter lays the foundational theory required to understand interactions in lattice devices, which is elaborated upon in Ch. 5. Initially in Sec. 2.1, we review light-matter interactions in cavity Quantum Electrodynamics (QED) and circuit QED frameworks, and compare such systems. The subsequent section (Sec. 2.2) is dedicated to mathematically formulating such interactions, leading to the derivation of the Jaynes-Cummings Hamiltonian. Furthermore, we explore the dispersive limit of the Jaynes-Cummings Hamiltonian, which enables quantum non-demolition (QND) measurements. The Jaynes-Cummings Hamiltonian describes a system with one qubit and one cavity. However, richer physics can be achieved when multiple qubits are coupled to multiple cavity modes. To treat such a system, we need to understand that a chain of coupled cavities results in a band structure. Therefore, in Sec. 2.3 we delve into the band structure of systems comprised of multiple interconnected cavities forming a lattice. In Sec. 2.4, we focus on the atom-photon bound state that arises from the coupling of a qubit to a bosonic lattice. We then extend this treatment to investigate interactions that emerge when multiple qubits are coupled to a lattice. Finally, Sec. 2.5 is dedicated to studying cross-Kerr interactions, which are non-linear atom-mediated interactions between photons. Such interactions may be observed when a qubit is coupled to multiple cavities.

2.1 Cavity and Circuit Quantum Electrodynamics

The study of interactions between light and matter is essential for developing quantum computers, simulating complex quantum systems, exploring new quantum phenomena, and understanding the nature of quantum physics [21]. There are different platforms that are used for studying light-matter interactions on a quantum level. Initially, such systems were studied in the context of cavity QED, which traditionally involves a Fabry-Perot cavity, made of two mirrors, coupled to a two-level atom [22]. In recent decades, circuit QED, which is comprised of artificial systems, has become another popular platform for studying such interactions. These systems are often made of circuits that are lithographically defined on superconducting metals, and are cooled to low temperatures [23]. In this section, we explore the similarities and differences between cavity and circuit QED platforms. We will also outline the advantages and drawbacks of different platforms in this section.

Cavity QED, which emerged in the late 1980s, and the study of light-matter interactions on a quantum level gained David Wineland and Serge Haroche the 2012 Nobel Prize [24, 25]. In such systems, one couples a two-level atom to photons in a Fabry-Perot cavity - which is an optical cavity made with mirrors [22] - with coupling strength g. For cavity QED systems, g can be as large as 100 MHz [26]. Fig. 2.1 illustrates an atom, shown in orange, coupled to a cavity shown in blue. The photons inside the cavity decay at a rate κ due to decoherence processes, and set the linewidth of the cavity. The parameter $\gamma_\perp$ facilitates the decay of the qubit into modes external to the cavity. This phenomenon may arise from factors such as the cavity free space radiation.

The main type of light-matter interaction that can occur in such a setup is often referred

5

to as Rabi oscillation, named after Isaac Rabi. In this process, the photon in the cavity can be absorbed by the atom and and excite it. The excitation will then oscillate back and fourth between the atom and the cavity [27]. In the strong coupling regime, where $g > \kappa, \gamma_\perp$, many Rabi cycles can be completed before the photon leaks out of the cavity. These oscillations are completed at a Rabi frequency of $\Omega_r/2\pi$ [12]. As we will see in Sec. 2.2, with n excitations in the system, the Rabi frequency is given by $\Omega_n = 2g\sqrt{n}$ [28].
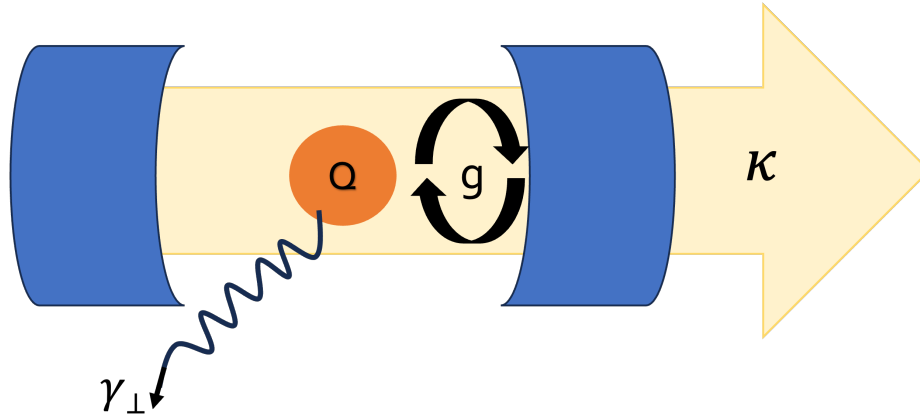
Figure 2.1: **Cartoon of a Cavity QED System** A qubit shown in an orange circle is coupled to a Fabry-Perot cavity depicted in blue. The coupling strength between the two is g. The qubit can decay out of the cavity into lossy modes at a rate $\gamma_\perp$. Photons in the cavity decay at a rate κ.

In circuit QED, one uses lithographically defined circuits to achieve interactions between light and matter. The Fabry-Perot cavity now becomes a superconducting resonator, such as a coplanar waveguide (CPW) resonator, and the two-level atom is now a transmon qubit, which is an anharmonic oscillator [29, 30] (we will study these elements in detail in Ch. 3).

While circuit QED poses challenges such as uniformity in device fabrication, it has certain advantages over conventional cavity QED systems, which have made it a popular platform in the recent decades. For instance, in circuit QED, variations in fabrication can lead to discrepancies in qubit and cavity frequencies, and coupling strengths. However, the inherent design of circuit

QED systems facilitates stronger interactions between qubits compared to their cavity QED coun-

terparts. Such strong interactions are crucial for the development of more efficient and scalable

quantum computing architectures, offering a significant advantage despite fabrication challenges.

So while there are variations in properties of circuit QED elements, it is still a scalable alternative

to cavity QED. Additionally, the cooperativity in circuit QED systems, given by $C = g^2/\kappa\gamma_\perp$,

is large compared to the relaxation time of the qubit (dissipation or T_1). This allows for many

operations to be completed before the qubit relaxes to its ground state [12, 30].

2.2   Light-Matter Interactions

We would like to start by deriving the Hamiltonian for the semi-classical atom and field.

In the semi-classical limit, we first consider an atom with frequency ω_q that is being driven by

a semi-classical field. The drive has frequency ω_d and amplitude Ω. The Hamiltonian of this

system is given by

$$\hat{H} = \frac{\hbar}{2}\omega_q\sigma_z + 2\hbar\Omega\cos{(\omega_d t)}\sigma_x. \tag{2.1}$$

To write the Hamiltonian in the frame rotating at ω_d, we start by applying a unitary transformation

$U = \exp\left(\frac{i\omega_d t}{2}\sigma_z\right)$. The Hamiltonian would transform as

$$\hat{H}_I = i\frac{\partial U}{\partial t}U^\dagger + UHU^\dagger. \tag{2.2}$$

The first term simply yields $-\omega_d \sigma_z / 2$. The second term can be calculated as

$$U\hat{H}U^\dagger = U \left(\underbrace{\hbar \frac{\omega_q}{2} \sigma_z}_{A} + \underbrace{2\hbar\Omega \cos\left(\omega_d t\right) \sigma_x}_{B} \right) U^\dagger, \tag{2.3}$$

where

$$
\begin{aligned}
UAU^\dagger &= \hbar \frac{\omega_q}{2} \sigma_z \\
UBU^\dagger &= \hbar\Omega \left(e^{2i\omega_d t} \sigma_- + \sigma_+ + \sigma_- + e^{-2i\omega_d t} \sigma_+ \right).
\end{aligned}
\tag{2.4}
$$

Hence,

$$\hat{H}_I = \hbar \frac{\sigma_z}{2} \left(\omega_q - \omega_d \right) + \hbar\Omega \left[\sigma_+ \left(e^{-2i\omega_d t} + 1 \right) + \sigma_- \left(e^{2i\omega_d t} + 1 \right) \right]. \tag{2.5}$$

Now the Hamiltonian in Eq. 2.5 has time dependent terms. We can perform a rotating wave approximation (RWA) by going into the rotating frame of the driving field, and dropping the "counter-rotating" terms [15, 31]. This approximation holds well in the weak-coupling regime and in near-resonant cases. Using RWA, our resulting Hamiltonian is

$$
\begin{aligned}
\hat{H}_{RWA} &= \hbar \frac{\sigma_z}{2} \left(\omega_q - \omega_d \right) + \hbar\Omega \left[\sigma_+ + \sigma_- \right] \\
&= \hbar \frac{\sigma_z}{2} \left(\omega_q - \omega_d \right) + \hbar\Omega \sigma_x.
\end{aligned}
\tag{2.6}
$$

To go beyond the semi-classical theory, we consider Eq. 2.7, which is the Rabi Hamiltonian. Then by performing a similar RWA approximation for quantized light, we can derive the atom-light Hamiltonian known as the Jaynes-Cummings Hamiltonian seen in Eq. 2.8. The Jaynes-Cummings Hamiltonian is derived by taking the full Hamiltonian of this system in the interaction picture with respect to the field evolution, and taking it into the Schrödinger picture, by perform-

ing an RWA and dropping the counter-rotating terms [15,31]. The interaction term, known as the Rabi model, has the form

$$\hat{H}_{int} = \hbar g \left(a + a^\dagger \right) \left(\sigma_+ + \sigma_- \right), \qquad (2.7)$$

which includes the $a^\dagger \sigma_+$ and $a\sigma_-$ counter-rotating terms. After performing RWA, we arrive at the Jaynes-Cummings Hamiltonian

$$\hat{H}_{JC} = \hbar \omega_r a^\dagger a + \frac{\hbar}{2} \omega_q \sigma_z + \hbar g \left(a^\dagger \sigma^- + a\sigma^+ \right), \qquad (2.8)$$

where the first, second, and third terms describe the cavity, the atom, and their interactions, respectively. This Hamiltonian describes simple systems consisting of one atom and a cavity with one photonic or bosonic mode [15,32].

We now take the Jaynes-Cummings Hamiltonian in Eq. 2.8, and diagonalize it in the $|n,\uparrow\rangle$, $|n+1,\downarrow\rangle$ basis in order to find its eigenvalues. Here, $0 \leq n \leq N$ is the number of excitations in the cavity. We write the Hamiltonian in the block-diagonal form [18]

$$H_n^{JC} = \begin{pmatrix} n\omega_r + \frac{\omega_q}{2} & g\sqrt{n+1} \\ g\sqrt{n+1} & (n+1)\omega_r - \frac{\omega_q}{2} \end{pmatrix}, \qquad (2.9)$$

but as the total number of excitations in the system is conserved, the blocks are not coupled. Hence, we can find their eigenvalues by diagonalizing each 2×2 block separately [18]. We find

that the eigenvalues of the nth submatrix are given by

$$E_{\pm,n} = \hbar n \omega_r \pm \frac{\hbar}{2}\sqrt{4ng^2 + \Delta^2}$$

$$E_{g,0} = -\hbar\frac{\Delta}{2},$$

(2.10)

where $\Delta = \omega_q - \omega_r$ is the atom-cavity detuning. We find that the un-normalized eigenstates are given by

$$|\overline{+,n}\rangle = A\left(-\frac{\Delta + \sqrt{4g^2 n + \Delta^2}}{2g\sqrt{n}}\,|g,n\rangle + |e, n-1\rangle\right)$$

$$|\overline{-,n}\rangle = B\left(-\frac{\Delta - \sqrt{4g^2 n + \Delta^2}}{2g\sqrt{n}}\,|g,n\rangle + |e, n-1\rangle\right).$$

(2.11)

But we can simplify the eigenstate expressions by defining an angle

$$\theta_n = \frac{1}{2}\arctan\left(\frac{2g\sqrt{n}}{\Delta}\right).$$

(2.12)

The eigenstates then become (see Fig. 2.2)

$$|\overline{+,n}\rangle = \sin\theta_n\,|g,n\rangle + \cos\theta_n\,|e,n-1\rangle$$

$$|\overline{-,n}\rangle = \cos\theta_n\,|g,n\rangle - \sin\theta_n\,|e,n-1\rangle$$

(2.13)

The dressed state levels are separated by $\Omega_n = 2g\sqrt{n}$, which are the n photon Rabi frequencies. In the single excitation manifold (i.e $|g,1\rangle$ and $|e,0\rangle$), we get vacuume Rabi oscillations and a splitting of $\Omega_1 = 2g$ between the exact dressed eigenstates, which is referred to as vacuum Rabi splitting [28]. Adding photons increases the Rabi frequency, which can be seen in Ω_n (see Fig. 2.2).
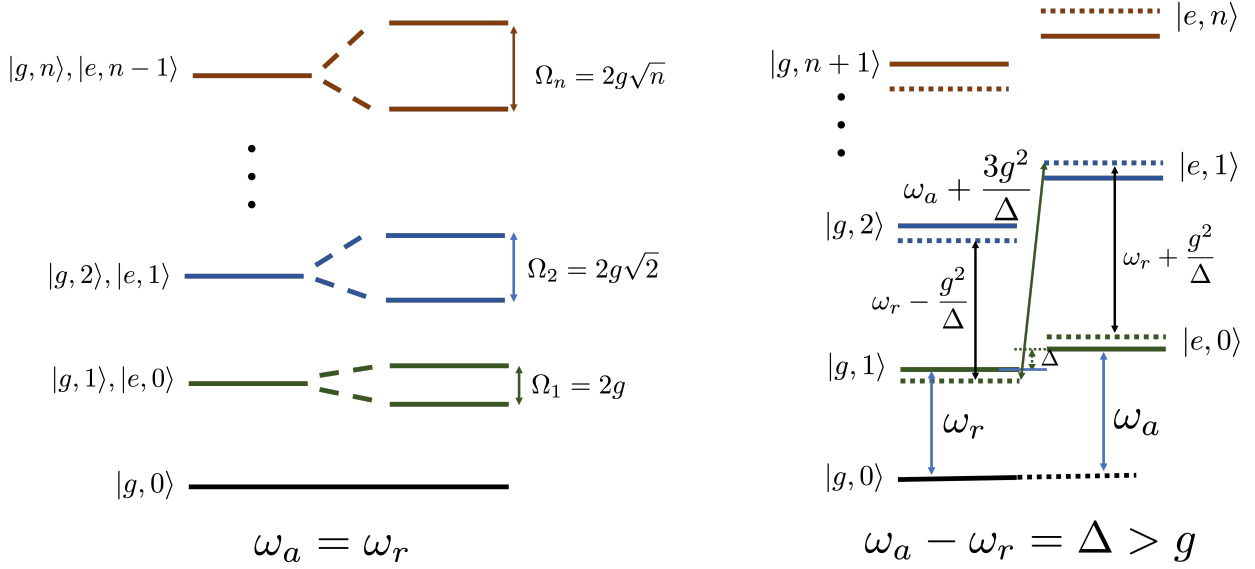
Figure 2.2: **Dressed State Energies of the Jaynes-Cummings Model** In this figure, the solid lines represent the eigenstates of the uncoupled Hamiltonian, while the dashed lines show the energies when the atom and photon are coupled. $|g, n\rangle$ ($|e, n\rangle$) represents the state in which the qubit is in its ground (excited) state and the cavity has n photons. The panel on the left shows the energy levels for the resonant atom-photon case, and the one on the right shows the levels in the dispersive regime. In the resonant case, the atom and cavity hybridize perfectly and result in a Rabi splitting of the levels. In the dispersive case however, the atom and the cavity preserve their natures for the most part, but cause a frequency shift in one another.

2.2.1   The Dispersive Limit

In the "near-resonant" regime, where the detuning between a coupled atom and a cavity is small, such that $\Delta \ll g$, the energy levels of the atom and the cavity hybridize. We would then observe a Rabi splitting of the size $2\hbar\sqrt{n}g$ in the dressed energy levels, where $n = 1, 2, 3, ...$ are the energy levels of the resonator cavity. In this regime, the cavity and atom exchange interactions, thus realizing a swap operation. However, as the eigenstates are coherent superpositions of atoms and photons, energy measurements cannot be used to measure atom and photon excitations separately. In this regime, any measurement of the qubit through the cavity would affect the state of the qubit. However, in the "dispersive limit", where $\Delta \gg g, \kappa$, photons are not absorbed by

the atom. Instead, the cavity and the qubit cause a shift in each other's frequencies. The qubit imposes a dispersive shift χ on the cavity, and the cavity shifts the qubit frequency through a vacuum Lamb shift of the same size. There is also a photon number dependent Stark shift on the qubit of the size $2ng^2/\Delta$, where n is the photon number. But in this regime, the qubit and the atom do not exchange interactions. In our setup, this allows us to perform quantum non-demolition (QND) measurements of the system [14]. This means that we can readout the state of the qubit through the cavity, without altering its own state, as the eignestates almost perfectly retain their qubit or bosonic nature. Therefore, the measurements of cavity energy shift can reliably reveal the state of qubit [12, 13, 33–35].

In the dispersive regime, the energy shift for a single cavity mode can be calculated using non-degenerate perturbation theory, where $E_{\text{pert}} = g^2/\Delta$. The wave function including the first order correction is given by $|\psi_1\rangle = |\psi_0\rangle + \alpha |\psi_b\rangle$, where $|\psi_0\rangle = |0, e\rangle$ and $|\psi_b\rangle = |1, g\rangle$ are the zeroth order eigenstates, and $\alpha = \langle\psi_b|H_{int}|\psi_0\rangle / (E_b - E_0)$. Therefore, the first-order wave function is given by

$$|\psi_1\rangle = |0, e\rangle + \left(\frac{\langle 1, g|H_{int}|0, e\rangle}{\Delta} \right) |1, g\rangle = |0, e\rangle + \frac{g_0}{\Delta} |1, g\rangle . \tag{2.14}$$

The Hamiltonian is then given by [12, 13, 33, 34, 36]

$$H_{disp,r} \approx \hbar \left(\omega_r + \frac{g^2}{\Delta}\sigma_z \right) \left(a^\dagger a + \frac{1}{2} \right) + \hbar\omega_q \frac{\sigma_z}{2}, \tag{2.15}$$

We can see in the first term that now the frequency of the resonator shifts by $\chi = g^2/\Delta$, depending on the state of the atom. As mentioned before, this provides a way to measure the qubit state

through measuring the energy shift of the cavity. This is essential to our measurements, as we cannot readout the state of the qubit directly. We will explain how this type of measurement can be experimentally executed in Ch. 4.3.

We can also group the terms differently to see how the qubit behaves as a result of the interaction. The Hamiltonian now becomes [13]

$$H_{disp,q} \approx \hbar \omega_r \left(a^\dagger a + \frac{1}{2} \right) + \frac{\hbar}{2} \left(\omega_q + \frac{2g^2}{\Delta} a^\dagger a + \frac{g^2}{\Delta} \right) \sigma_z. \tag{2.16}$$

The two terms that are grouped together with ω_q and are shifting the qubit frequency are called the AC Stark shift and Lamb shift respectively. We can see that the AC Stark shift depends on the number of photons in the cavity [20, 33].

To understand the limits of the dispersive regime we can refer back to Eq. 2.10 and perform a Taylor expansion in $n (g/\Delta)^2$ to find the eigenvalues in this limit

$$E_{\pm,n} \simeq \hbar n \omega_r \pm \left(\Delta + \hbar \frac{ng^2}{2\Delta} \right). \tag{2.17}$$

We can then approximate the eigenstates in the dispersive limit (see Fig. 2.2)

$$\begin{aligned}
\overline{|+,n\rangle} &= \frac{g\sqrt{n}}{\Delta} |g,n\rangle + |e,n-1\rangle \\
\overline{|-,n\rangle} &= |g,n\rangle - \frac{g\sqrt{n}}{\Delta} |e,n-1\rangle.
\end{aligned} \tag{2.18}$$

The eigenstates are approximately the unperturbed eigenstates

$$\overline{|+,n\rangle} \approx |e,n\rangle$$

$$\overline{|-,n\rangle} \approx |g,n+1\rangle\,.$$

(2.19)

In this section, we treated the qubit as a perfect two-level system. However, in experiment, the qubits are not perfect two-level systems, but multi-level systems with different spacing between energy levels. This means that the actual qubits are only approximately two-level systems, and are more complex. We will discuss one such qubit, the transmon [20], in Ch. 3.2.

2.3 Band Structure

As we know, the band structure of a material describes its energy dispersion relation. There are several methods for calculating the band structure, the simplest of which is the tight-binding model explored in Sec. 2.3.1.

2.3.1 Tight-Binding Model for a One-Dimensional Chain

The band structure of many systems can be approximated using the tight-binding model. The simplest system that can be solved using this method is a one-dimensional lattice [37]. A very simple example of this is particles hopping in overlapping harmonic potentials. However, this simple model has a direct analog in circuit QED systems, i.e. chain of coplanar waveguide resonators (see Ch. 3.1), as photons in a cavity resemble harmonic oscillators that can weakly hop to neighboring potential wells compared to their confinement. The photons in one cavity can hop to an adjacent one. The physics of such a system can be modeled using the tight binding

Hamiltonian [5, 38]

$$H = \hbar \sum_n \omega_n a_n^\dagger a_n + \hbar \sum_n t_{n,n+1} \left(a_n^\dagger a_{n+1} + a_{n+1}^\dagger a_n \right), \qquad (2.20)$$

where the first term is the Hamiltonian of a harmonic oscillator with frequency ω_n, and the second term represents the photon hopping between neighboring sites n and $n+1$ at rate $t_{n,n+1}$. Here, a_n and $a_n^\dagger$ are annihilation and operators operators, respectively, and satisfy the canonical commutation relations $[a_n, a_n^\dagger] = 1$.

To simplify the model, we assume that the hopping is constant throughout the lattice, such that $t_{n,n+1} = t$ for all n. We also assume that the frequencies of all resonators are equal, i.e., $\omega_n = \omega$. In the limit of large number of sites, one can show that the eigenmodes of the system are waves. The dispersion relation, which is energy or frequency of these eigenmodes as a function of wavevector k, is of the form $\omega(k) \propto \cos k$, where k represents momentum [39]. Note that near $k = 0$, the dispersion is approximately quadratic (see Fig. 2.4).
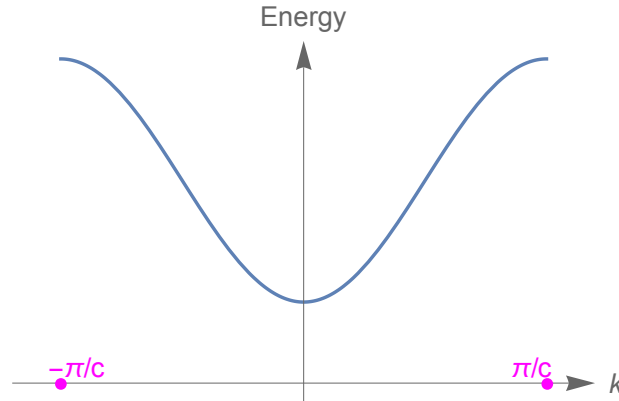

Figure 2.3: **Cosine Dispersion Relation** A one-dimensional chain of atoms has a *cosine* dispersion relation. Here, we have shown the dispersion relation in the first Brillouin zone.

This band structure (for a one-dimensional lattice with a single resonator in each unit cell) can be obtained as follows. The following calculation can be found in Ref. [37, 39, 40]. We

15

assume that the lattice sites are identical. We would like to solve the Schrödinger equation $H\ket{\psi} = E\ket{\psi}$, with tha Hamiltonian from Eq. 2.20

$$\ket{\psi} = \sum_m \psi_m \ket{m}, \tag{2.21}$$

where $\ket{m}$ is an eigenstate of $a^\dagger a$, such that $a^\dagger a \ket{m} = n\ket{m}$. Expressing the time-independent Schrödinger equation in the above basis yields

$$E_0 \sum_m \psi_m \ket{m} - t\left(\sum_m \psi_{m+1}\ket{m} + \psi_m \ket{m+1}\right) = E\sum_m \psi_m \ket{m}. \tag{2.22}$$

We can now write the overlap with a state $\bra{n}$. The overlap looks like $\bra{n}H\ket{\psi} = E\braket{n|\psi}$. This yields a set of linear equations for ψ_n

$$E_0\psi_n - t\left(\psi_{n+1} + \psi_{n-1}\right) = E\psi_n, \tag{2.23}$$

where the equation can be solved by the following ansatz

$$\psi_n = \frac{e^{iknc}}{\sqrt{N}}, \tag{2.24}$$

where c is the lattice constant, which specifies the size of a single unit cell, and $\sqrt{N}$ is the normalization factor. In the wavefunction above, k is the wave-number (which we also refer to as momentum), and it takes values

$$k \in \left(-\frac{\pi}{c}, +\frac{\pi}{c}\right], \tag{2.25}$$

16

Here, k is known as the Brillouin zone, and the domain above is the first Brillouin zone [15]. We impose a periodicity condition and require that $\psi_{n+1} = \psi_1$. This means that $e^{ikNc} = 1$. Thus, k needs to be quantized in units of $2\pi/cN$.

For now, if we ignore the normalization factor in Eq. 2.24, we can see that the states have the following property

$$\psi_{n\pm1} = e^{\pm ikc}\psi_n. \tag{2.26}$$

This means that the eigenenergies of Eq. 2.23 for all k is given by

$$E = E_0 - 2t\cos(kc). \tag{2.27}$$

In a regime where the momentum is small, such that $k \ll \frac{\pi}{c}$, we are able to perform a Taylor series expansion on Eq. 2.27 and approximate the energies as

$$E(k) \approx (E_0 - 2t) + tc^2k^2, \tag{2.28}$$

which is of the quadratic form shown in Fig. 2.4.

We can also find the band structure by first re-writing the Hamiltonian in the form below, and assuming periodic boundary conditions [41]

$$H = -t\sum_{i}^{N}(|n\rangle\langle n+1| + |n+1\rangle\langle n|). \tag{2.29}$$

Having periodic boundary conditions means that the last term becomes $|N\rangle\langle 1|$, as the first and the last lattice site are coupled to each other as well. Since the Hilbert space of the tight binding
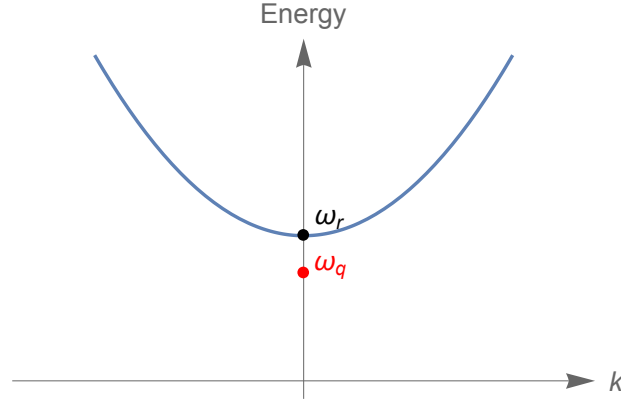
Figure 2.4: **Quadratic Dispersion Relation** We place a qubit at frequency ω_q, and assume that we are in the dispersive limit in order to solve for the wave function correction using perturbation theory. For calculation, refer to Sec. 2.4

model is finite, we can write $H = \langle n \,|\, M \,|\, m \rangle$,where M is

$$
M = \begin{pmatrix}
\omega & t & 0 & \cdots & & & t \\
t & \omega & t & 0 & \cdots & & \\
0 & t & \omega & t & 0 & \cdots & \\
& & & \ddots & & & \\
t & 0 & & \cdots & 0 & t & \omega
\end{pmatrix}.
\tag{2.30}
$$

We would like to find the eigenvalues and eigenvectors for Eq. 2.29, and derive the solution for

$H \,|\psi\rangle = E \,|\psi\rangle$. We assume that the lattice has translational invariance. The eigenstates can

be written in the n basis as $|\psi\rangle = \sum_n \psi_n \,|n\rangle$. The matrix M can be diagonalized by Fourier

transforming into the k basis

$$
a_n = \frac{1}{\sqrt{N}} \sum_k e^{ikx_n} a_k,
\tag{2.31}
$$

where N is the number of sites, and

$$k = \frac{2\pi L}{Nc}, \quad -N/2 < \ell < N/2 \quad \Rightarrow \quad k \in \left(-\frac{\pi}{c}, \frac{\pi}{c}\right].$$ (2.32)

We now plug in Eq. 2.31 into Eq. 2.20 and diagonalize the matrix, and drop the first term in the Hamiltonian to get

$$
\begin{aligned}
H &= -\frac{t}{N} \sum_{k,q} \left[a_k^\dagger a_q \left(e^{iq} + e^{-ik} \right) \right] \sum_n e^{-i(k-q)x_n} \\
&= -t \sum_{k,q} \left[a_k^\dagger a_q \left(e^{iqc} + e^{-ikc} \right) \right] \delta_{k,q} \\
&= -2t \sum_k \cos\left(kc\right) a_k^\dagger a_k
\end{aligned}
$$ (2.33)

Now we can solve for the energy $E_k = -t \sum_n e^{ikx_n}$. This yields a diagonal Hamiltonian

$$H = \sum_k E_k \left| k \right\rangle \left\langle k \right|.$$ (2.34)

Thus, the dispersion relation is

$$E_k = -2t \cos\left(k\right).$$ (2.35)

In Ch. 3, we explore circuit QED systems and see that in such systems we can achieve photon hopping between adjacent CPW resonators. The hopping strength depends on the capacitance at the junction where the resonators meet one another [42], as explained in Ch. 3.4.

2.4 Photonic Bound States

While the previous example of a one-dimensional lattice was linear, adding nonlinear elements such as an anharmonic oscillator to the lattice can create a rich interacing system. This is directly relevant to circuit QED system where we can place qubits in resonator lattices (see Ch. 3.1). An example of an interesting phenomenon that emerges in such systems is the formation of photonic bound states [8, 9, 16, 17, 43]. To study bound states experimentally, we can engineer bosonic lattices with variety of band structures using photonic crystals. Photonic crystals are of interest due to having tailorable band structures [16].

A photonic bound state forms around a qubit that is coupled to the band-edge of a photonic crystal. These dressed qubit-photon bound states form in the strong coupling regime [16, 17]. The strong coupling regime occurs when the interaction strength exceeds decoherence rates. In a one-dimensional quadratic band, the coupling between the qubit and the photonic band edge gives rise to an exponentially localized photonic mode, whose center lines up with the qubit [8, 16, 17, 43].
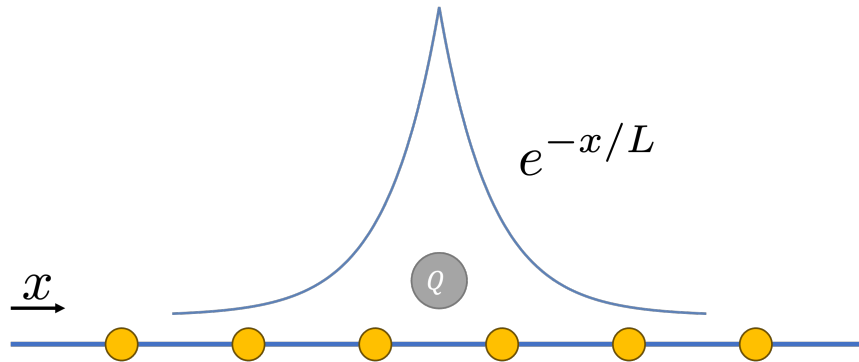
Figure 2.5: **Photonic Bound State** In this figure, we have a one-dimensional chain of resonators shown with horizontal blue lines, coupled to each other using yellow circles. This structure, which forms a photonic crystal, is coupled to a qubit shown with a gray circle. In this setup, a photonic bound state with an exponentially decaying envelop forms around the qubit. Here, x is the position along the one-dimensional lattice structure, and L is the localization length [16, 17].

In the strong coupling regime, the photon and the atom hybridize to form a polariton state, which is a quantum state that is part light and part matter. These states are mostly qubit-like in the band-gap and more photon-like near the band-edge [8]. The photonic part of this dressed state is exponentially localized around the qubit [8, 10, 44].

In Fig. 2.5, the horizontal blue lines alternating with yellow circles represent a photonic crystal, and the gray circle represents the qubit. In this type of photonic crystal, the blue lines symbolize resonators that are capacitively coupled to each other at the location of yellow circles. The photonic bound state is localized centered around the qubit. The amplitude of its envelope decays as $\sim e^{-x/L}$, with x being the distance from the qubit, and L being the localization length [16]. This can be obtained by performing a perturbative calculation as follows: for a simple quadratic band structure, such as the one shown in Fig. 2.4, one can place a single qubit in the band gap with frequency ω_q. The Hamiltonian of a such system is given by

$$H = \hbar \sum_k \omega_k a_k^\dagger a_k + \frac{\hbar}{2} \omega_q \sigma^z + \hbar \sum_k g_k \left(a_k^\dagger \sigma^- + a_k \sigma^+ \right), \qquad (2.36)$$

where g_k are the rates at which an atom absorbs and emits a photon, and a_k and $a_k^\dagger$ are the annihilation and creation operators for mode k satisfying canonical commutation relations. ω_k are the mode frequencies [8, 9].

We also assume that we are in the dispersive regime, i.e. the detuning is larger than the coupling strength: $\Delta = \omega_q - \omega_k \gg g_k$, so we can use perturbation theory. The interaction part of the Hamiltonian (2.36) is $H_{\text{int}} = \sum_k g_k (a_k^\dagger \sigma^- + a_k \sigma^+)$. By generalizing Eq. (2.14) to a lattice

of CPW resonators we find that

$$|\psi_1\rangle = |0, e\rangle + \sum_k \frac{g_k}{\Delta_k} |1_k, g\rangle, \tag{2.37}$$

where the second term is the first order correction, $|\psi_b\rangle$. We now perform Fourier transform (FT) to express the photonic part of the wave function in position space. Specifically, we can assume that the spatial component of $|1_k\rangle$ have a plane wave $E_k(x) = \langle x \,|\, 1_k\rangle$ with momentum k, where

$$E_k(x) = E_0 e^{ikx}. \tag{2.38}$$

Noting that the cos dispersion relation is approximately quadratic where k is small, we have $\Delta_k = \omega_k - \omega_q = \omega_r + \alpha k^2 - \omega_q$. Therefore, we find the first order correction to the wave function to be

$$
\begin{aligned}
|\psi_b\rangle &= \int dx \int dk \frac{g_k}{\Delta_k} |x\rangle \langle x|1_k\rangle \otimes |g\rangle \\
&= \int dx \int dk E_0 e^{ikx} \frac{g_k}{\Delta_k} |x\rangle \\
&= \int dx \int dk E_0 e^{ikx} \frac{g_k}{\Delta + \alpha k^2} |x\rangle.
\end{aligned} \tag{2.39}
$$

When the bandwidth is narrow enough so that $g_k = g \approx constant$, we can factor out Δ, g, and E_0 to find

$$|\psi_b\rangle = \frac{E_0 g}{\Delta} \int dx \int dk e^{ikx} \frac{1}{1 + \frac{\alpha k^2}{\Delta}} |x\rangle. \tag{2.40}$$

22

This is the FT of a Lorentzian, which simply yields

$$\psi_b(x) = \langle x \,|\, \psi_b \rangle = \frac{E_0 g e^{-|b|x}}{\Delta},$$

(2.41)

where $|b| = \sqrt{\frac{\Delta}{\alpha}}$. Therefore, we find that the photonic bound state has the expected exponentially decaying envelope.

The localization length of the photonic envelop is given by [8, 9, 16, 17]

$$L = c\sqrt{\frac{\alpha}{\delta}},$$

(2.42)

where δ is the detuning between the band edge and the qubit. Moreover, the linewidth of the bound state is given by $\gamma \sim e^{-d_0/2L}$, where d_0 is the length of the device. The localization length increases as the bare qubit frequency (ω_q) is tuned closer to the band-edge. This means that the linewidth becomes larger as well [8]. This is due to the device being finite and having physical boundaries. At these boundaries, there is significant photon loss due to imperfections that couple the device to the environment. As the localization length increases, the state extends further, and become more susceptible to these boundary losses. This loss is manifested in broader linewidth of the state. It has been experimentally observed that there exists a localized state in the band gap when ω_q is in the passband (states above the band-edge frequency) [8]. However, the state becomes less localized if the bare qubit frequency is tuned closer to the band-edge [16].

This can be generalized to multi-qubit setups to explore the interactions between the bound states in photonic crystals [16, 17, 44, 45]. For instance, two atoms in a photonic crystal each form a bound state, or they can hybridize to form a single bound state. We assume that x_i denotes the

location of an atom. As an example, in a system where the quadratic band edge is near $k = \pi$, the flip-flop interaction Hamiltonian between the two bound states is [16]

$$\hat{H} \propto \sum_{i,j} \sigma_+^i \sigma_-^j \, (-1)^{|x_i - x_j|/c} \, e^{-|x_i - x_j|/L}. \tag{2.43}$$

The Schrödinger equation for this system can be solved exactly in the one-excitation subspace, and the energies would depend on $d = |x_1 - x_2|$. If the qubits are far away in terms of the lattice constant, so that $d > L$, then two degenerate ground states form, with energies approximately equal to the energy of a single-atom bound state. But if the distance between the qubits is smaller than the localization length L, the qubits start to hybridize with one another. This can result in an effective flip-flip interaction [44], i.e. $\sigma_x \sigma_x + \sigma_y \sigma_y$.

2.5   Non-Linear Interactions

In a lattice of resonators, a qubit can be utilized to facilitate non-linear photon-photon interactions, a phenomenon rooted in the Kerr effect. This effect is fundamentally characterized by the presence of four boson operators, signifying its non-linear nature [18]. One can observe a non-linear shift in the resonator frequency according to the number of photons in the mode, which yields a "self-Kerr" coefficient. [18,46]. Similarly, when there are more than one photonic modes, the qubit can mediate interactions between bosons resulting in $n_a n_b$ interactions, the coefficient of which is referred to as the "cross-Kerr" coefficient. The Kerr effect can be strong in circuit QED systems, as one can engineer strong couplings in the dispersive limit [18,47].

Let us first explore the self-Kerr of the cavity by recalling Eq. 2.10. Remembering that we are in the dispersive limit where $\Delta \gg g$, and assuming that the qubit remain in its ground state,

we expand the square-root term of the eigenvalues in g/Δ and obtain [18]

$$E_n^{JC} \simeq \left(\omega_r - \frac{g^2}{\Delta} + \frac{2g^4}{\Delta^3} \right) n + \frac{g^4}{\Delta^3} n^2. \tag{2.44}$$

For a perfect two level system, the last term, which is an n^2 term, is the self-Kerr coefficient of the cavity, whose sign is clearly determined by the sign of the detuning [18].

Similarly, in systems with more than one bosonic mode, qubits can mediate interactions between the modes. We can derive these effects, known as the cross-Kerr interaction. To simplify matters, lets consider the case of two cavities coupled to a single two-level atom. The Hamiltonian for such a system is given by

$$\hat{H}_{2C1Q} = \hbar \sum_{i=1}^{2} \omega_{r,i} a_i^\dagger a_i + \frac{\hbar}{2}\omega_q b^\dagger b + \hbar \alpha b^\dagger b^\dagger bb + \hbar g \sum_{i=1}^{2} 2 \left(a_i b^\dagger + a_i^\dagger b \right), \tag{2.45}$$

where α is the non-linearity of the transmon qubit, and b and $b^\dagger$ are the raising and lowering operators for the transmon [18] (for more information on the transmon qubit see Ch. 3.2). We are also assuming that the coupling strength between the first mode and the qubit is the same as that between the second mode and the qubit.

By integrating out the qubit part and ignoring self-Kerr, we find the simplified cross-Kerr Hamiltonian for a mode a_1 and a mode a_2 up to the fourth order to be

$$H_{cK} = \hbar \omega_{a1} a_1^\dagger a_1 + \hbar \omega_{a2} a_2^\dagger a_2 + \hbar \chi a_1^\dagger a_1 a_2^\dagger a_2. \tag{2.46}$$

Here, χ is the cross-Kerr coefficient. Now we can rearrange the terms such that

$$H_{cK} = \hbar\omega_{a1}a_1^\dagger a_1 + \hbar\left(\omega_{a2} + \chi a_1^\dagger a_1\right)a_2^\dagger a_2. \tag{2.47}$$

Here, we see that there is a shift in the frequency of mode a_2, which depends on the number of photons in mode a_1. For a perfect two-level system in the RWA, which is simpler than the transmon, the cross-Kerr coefficient can be written as

$$\chi_{a1,a2} = -2g_{a1}^2 g_{a2}^2 \frac{\Delta_{a1} + \Delta_{a2}}{\Delta_{a1}^2 \Delta_{a2}^2}, \tag{2.48}$$

where Δ_{a1} and Δ_{a2} are detunings of the qubit from modes a_1 and a_2, respectively, and g_{a1} and g_{a2} are the coupling strength of the qubit to those modes.

In this chapter, we discussed light-matter interactions broadly without specifying how the qubit or the photon are realized in circuit QED systems. In the next chapter, we introduce these elements.

Chapter 3: Hardware Theory

In this section, we look at the building blocks necessary for making a system that facilitates light-matter interactions using superconducting circuits. We first study the coplanar waveguide (CPW) resonator, which is the equivalent of an optical cavity. The circuit QED counterpart of the two-level atom is the transmon qubit, which is capacitively coupled to the CPW resonator to form a circuit. When we couple a qubit to a CPW resonator, we have an artificial atom interacting with microwave photons, which is similar to cavity QED.

We then explore the formalism of the coupling between the qubit and the CPW resonators. When multiple resonators are coupled to each other, photons can hop between them. Therefore, lastly, we study the hopping of photons between different sites in lattices of CPW resonators.

3.1 Coplanar Waveguides

In superconducting circuits, CPW resonators can be used to make cavities similar to a Fabry-Perot optical cavity [22]. The CPW is analogous to a 2-D coaxial cable. We see an example of such a resonator in Fig. 3.1, where the gray strips are made of metal. The outer gray strips are ground planes and the strip in the middle is the center-pin of the CPW resonator. In circuit QED systems, these CPW resonators are typically between 3 mm - 15 mm long and operate in the microwave (GHz) regime [19, 33]. Specifically, for a half-wave resonator, which is

open at both ends and which we will study in the following, the frequency for CPWs with these lengths ranges from ~ 2 GHz to ~ 10 GHz.

Microwave photons traveling through a CPW cause the voltage across the center-pin to oscillate, and create an electric field in the gaps of the CPW. The CPW resonator can be modeled as a transmission line. In this model, we write a capacitance per length C_ℓ and an inductance per length L_ℓ. The impedance of the CPW seen in Fig. 3.1 can then be written as [19]

$$Z = \sqrt{\frac{L_\ell}{C_\ell}}, \tag{3.1}$$

and its phase velocity can be formulated as

$$\nu = \frac{1}{\sqrt{L_\ell C_\ell}}. \tag{3.2}$$

It is important to note that like many RF circuits, we design our circuits with $50\ \Omega$ characteristic impedance, which is the common environmental impedance [12, 13, 19].

Considering the CPW as a one-dimensional dielectric, we can re-write the phase velocity as [19]

$$\nu = \frac{c}{\sqrt{\epsilon_{eff}}}, \tag{3.3}$$

where c is the speed of light, and ϵ_{eff} is the effective permittivity of the transmission line.

Now we can find the frequency of the fundamental mode for every CPW by simply using $\nu = \lambda f$. Combined with Eq. 3.2 this yields

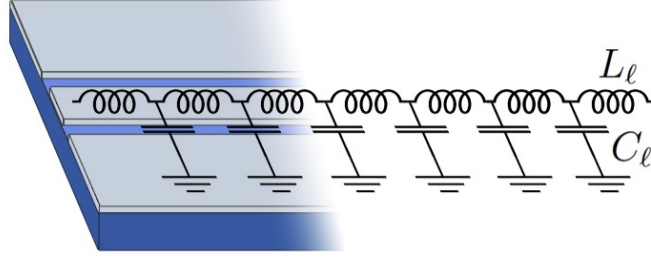$$f = \frac{1}{\sqrt{L_\ell C_\ell}} \frac{1}{\lambda}. \tag{3.4}$$

Figure 3.1: **CPW Resonator** The light blue regions indicate where there is metal, and the dark blue regions show the dielectric substance. One can illustrate the CPW as LC oscillators, and use a distributed model for CPW feedlines Figure made by Jeffrey Wack [48].

A resonator of length ℓ can either be shorted to the ground plain on one side and open on the other, or it can be open on both ends. The first case is a quarter-wave resonator, where $\ell = \lambda/4$, and the second one is called a half-wave resonator where $\ell = \lambda/2$. This is because at the short end the voltage is zero, while it has its maximum value at the open end. Armed with this information, we can re-write the frequency from Eq. 3.4 for these two types of resonators as [19]

$$
\begin{aligned}
f_{1/4} &= \frac{1}{\sqrt{L_\ell C_\ell}} \frac{1}{4\ell}, \\
f_{1/2} &= \frac{1}{\sqrt{L_\ell C_\ell}} \frac{1}{2\ell},
\end{aligned}
\tag{3.5}
$$

for a quarter-wave and a half-wave resonator, respectively.

The information above is essential for designing a CPW resonator. Additionally, formulating the CPW resonator as an LC oscillator allows us to find the Hamiltonian for such a structure.

To find Hamiltonian of a resonator by treating it as an LC oscillator, we start by defining

node flux Φ as the time integral of voltage

$$\Phi(t) = \int_{-\infty}^{t} V(t')\, dt', \tag{3.6}$$

where $V(t)$ is the branch voltage across each element, and $V(t) = \dot{\Phi}$ [13]. We will derive the Hamiltonian from the Lagrangian of the system. By treating the circuit as a lumped element, we can write the Lagrangian of the LC oscillator. We choose flux as our natural coordinate. We then write the potential energy stored on the capacitor (U) and the kinetic energy in the inductor (T) according to

$$
\begin{aligned}
U &= \frac{1}{2}CV^2 = \frac{1}{2}C\dot{\Phi}^2 \\
T &= \frac{1}{2}LI^2 = \frac{1}{2L}\Phi^2.
\end{aligned}
\tag{3.7}
$$

Thus, the Lagrangian simply becomes

$$\mathcal{L} = U - T = \frac{1}{2}C\dot{\Phi}^2 - \frac{1}{2L}\Phi^2. \tag{3.8}$$

Now the conjugate momentum to the flux is

$$Q = \frac{\partial \mathcal{L}}{\partial \dot{\Phi}} = C\dot{\Phi}. \tag{3.9}$$

So far we have been looking at classical treatment of the LC oscillator. To quantize, we promote

Φ and Q to quantum operators by writing their commutation relation, which is

$$\left[\hat{Q}, \hat{\Phi}\right] = \hat{Q}\hat{\Phi} - \hat{\Phi}\hat{Q} = -i\hbar. \tag{3.10}$$

From this point on, we should keep in mind that $\hat{Q}$ and $\hat{\Phi}$ are quantum operators. The Hamiltonian is now written as

$$\begin{aligned}
\hat{H} = \hat{Q}\dot{\hat{\Phi}} - \mathcal{L} &= \frac{\hat{Q}^2}{2C} + \frac{\hat{\Phi}^2}{2L} \\
&= \frac{1}{2}C\hat{V}^2 + \frac{1}{2}L\hat{I}^2.
\end{aligned} \tag{3.11}$$

We can now write the Hamiltonian above in terms of creation and annihilation operators

$$\hat{H} = \frac{\hbar\omega_r}{2}\left(\hat{a}^\dagger\hat{a} + \hat{a}\hat{a}^\dagger\right) = \hbar\omega_r\left(\hat{a}^\dagger\hat{a} + \frac{1}{2}\right), \tag{3.12}$$

where $\omega_r = 1/\sqrt{LC}$. $\left[\hat{a}, \hat{a}^\dagger\right] = 1$ as the two operators are

$$\begin{aligned}
\hat{a} &= +i\frac{1}{\sqrt{2\hbar\omega_r C}}\hat{Q} + \frac{1}{\sqrt{2\hbar\omega_r L}}\hat{\Phi} \\
\hat{a}^\dagger &= -i\frac{1}{\sqrt{2\hbar\omega_r C}}\hat{Q} + \frac{1}{\sqrt{2\hbar\omega_r L}}\hat{\Phi}.
\end{aligned} \tag{3.13}$$

We have now introduced the circuit equivalent of a cavity, which is a harmonic oscillator. CPW resonators can be capacitively coupled to each other to form lattices with engineered band structures [5, 38]. The next element we need to introduce is the artificial atom. In Ch. 2, we saw that coupling atoms to modes in lattices can yield interesting interactions and photonic bound states. The artificial atoms used in circuit QED systems are often transmon qubits. Although other types of qubits, such as "fluxonium" [49] have been popularized more recently, this work utilizes the

transmons. As such, in the next section we look at the its physics and structure.

3.2   Transmon

The transmon qubit, which is currently the leading qubit design in circuit QED, is made of a Josephson junction shunted by a capacitor. The Josephson junction acts as a non-linear inductor. It is a good approximation for a two-level system as it is an anharmonic oscillator [13, 20]. To derive the Hamiltonian for the transmon, we start by considering an LC circuit once again, which acts like a quantum harmonic oscillator (QHO). This derivation, which is found in Sec. 3.1, along with the theory of Josephson junctions, found in Sec. 3.2.1, allows us to derive the transmon Hamiltonian.

Before we move onto exploring Josephson relations, we need to further manipulate the Hamiltonian in Eq. 3.11. We define a reduced charge $\hat{n} \equiv \hat{Q}/2e$, and a reduced flux $\hat{\phi} = 2\pi\hat{\Phi}/\Phi_0$, where $\Phi_0 = h/2e$ is the magnetic flux quantum in a superconductor. We can then write re-write the Hamiltonian in terms of $\hat{n}$ and $\hat{\phi}$ [13]

$$\hat{H} = 4E_C\hat{n}^2 + \frac{1}{2}E_L\hat{\phi}^2, \tag{3.14}$$

where $E_C = e^2/2C$ is the Coulomb charging energy, and $E_L = \frac{1}{L}\left(\Phi_0/2\pi\right)^2$ is the inductive energy [11, 13]. $\hat{n}$ is analogous to $\hat{p}/\hbar$ and $\hat{\phi}$ is similar to $\hat{x}$.

The Hamiltonian in Eq. 3.14 is harmonic. In the next subsection, we show how anharmonicity can be introduced by modifying the second term of the Hamiltonian above to reflect the behavior of a non-linear inductor.

3.2.1 Josephson Junction and the Transmon Qubit

Eq. 3.14 is the Hamiltonian of the quantized LC oscillator. By replacing the inductor with a Josephson junction, which is a non-linear element, we introduce a nonlinear inductance to the conventional LC hamiltonian. The transmon, which is a Josephson junction shunted with a capacitor, is approximately a two-level system and can act as a qubit. In this section, we study the Josephson junction and derive the transmon Hamiltonian.

Fig. 3.2 shows the side-view sketch, the circuit representation, and an SEM image of a Josephson junction. The Josephson junction itself consists of two layers of superconducting islands separated by an insulator. In our case, the superconducting metal is made of aluminum and the insulator is made of aluminum oxide. The fabrication process is explained in Appendix 4.1.
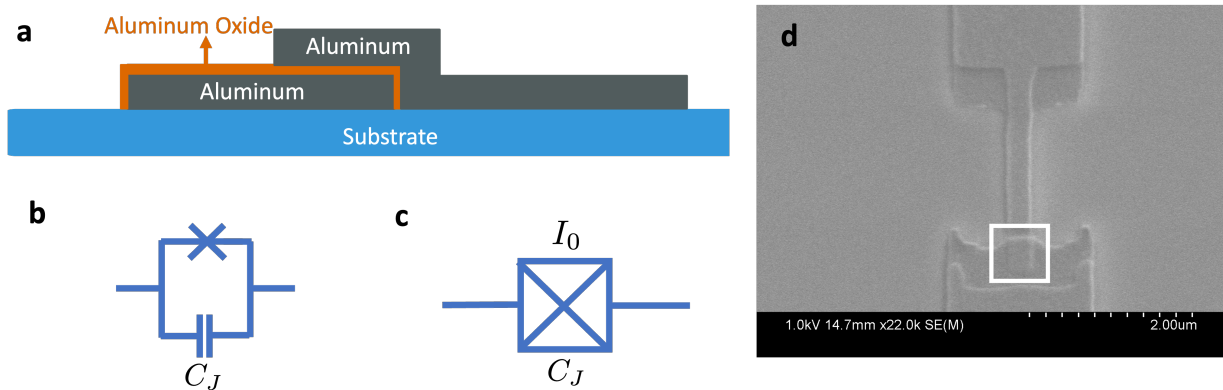

Figure 3.2: **Josephson Junction a-** Side-view sketch of a Josephson junction. The junction consists of two superconducting islands separated by an insulating layer. **b-** Circuit representation of a Josephson junction. The cross represents an ideal junction, and is always in parallel with intrinsic capacitance [50]. **c-** This symbol is equivalent to the circuit in panel **b**, and shows a Josephson junction [50]. **d-** SEM image of a Josephson junction made by the author. The white box reflects where the junction forms.

The Josephson junction allows for cooper pairs (pairs of electrons that form in low temperatures in superconductors) to tunnel from one island to the other. The cooper pairs need an energy of $2\Delta_s$ to be broken apart into two separate quasi-particles, where $\Delta_s\left(T < T_c\right) = 1.764 k_B T_c$ is

the excitation gap predicted by the Bardeen-Cooper-Schreiffer (BCS) theory [51,52]. In this relationship, k_B is the Boltzmann constant, and T_c is the critical temperature of a superconductor, at which the electrical resistance of the superconductor vanishes. The critical temperatures of aluminum and tantalum are ~ 1.2 K and ~ 4.48 K, respectively [53,54]. Thus, the energy gap is $\sim 3.4 \times 10^{-4}$ eV for aluminum and $\sim 14 \times 10^{-4}$ eV for tantalum [55].

In 1962, Josephson predicted that if two pieces of metal separated by a thin insulating layer have a zero voltage difference, then a supercurrent I flows between them [51,56]

$$I = I_c \sin(\phi), \tag{3.15}$$

Here, I_c, which is a critical current, is the maximum current that can be supported by a Josephson junction, and ϕ is the superconducting phase difference. If there is to be a voltage difference across the superconducting islands, then the phase would evolve in time according to [51]

$$\frac{d(\phi)}{dt} = \frac{2e}{\hbar}V. \tag{3.16}$$

But now, using Eq. 3.15 and Eq. 3.16, we can perform the integration below to find the free energy of the Josephson junction [51]

$$F = \int VIdt = \int \frac{\hbar}{2e} Id(\phi)$$
$$= constant - E_J \cos(\phi), \tag{3.17}$$

where $E_J = I_c \Phi_0/2\pi$ is the Josephson energy. Using Eq. 3.17 and the capacitance term of

Eq. 3.14, we find that the Hamiltonian for a transmon shown in Fig. 3.2 is given by [11, 13, 33]

$$\hat{H} = 4E_C \hat{n}^2 - E_J \cos\left(\hat{\phi}\right). \tag{3.18}$$

Now the charging energy is given by $E_C = e^2/2C_\Sigma$, where $C_\Sigma = C_J + C_B + C_g$. Here, C_J is the self-capacitance of the junction, and C_B is the effective shunting capacitance, and C_g is the gate capacitance, as shown in Fig. 3.4 [13, 20].

At this point, we can compare Eq. 3.18 with Eq. 3.14 to see that a $\cos\hat{\phi}$ term has replaced the $\hat{\phi}^2$ term. We can expand the $E_J \cos\hat{\phi}$ term into a power series, up to a constant term that is not relevant, as it is a global energy shift

$$E_J \cos\hat{\phi} = \frac{1}{2}E_j\hat{\phi}^2 - \frac{1}{24}E_J\hat{\phi}^4 + \mathcal{O}\left(\hat{\phi}^6\right), \tag{3.19}$$

where the $\hat{\phi}^2$ term is the linear inductor term, which we saw in the LC harmonic oscillator as well. $\hat{\phi}^4$ is the term that adds non-linearity to the system when a Josephson junction replaces a conventional inductor. This non-linearity results in anharmonicity in the energy levels, which can be seen in Fig. 3.3. The anharmonicity in such a system is given by $\alpha = \omega_{q,1\to 2} - \omega_{q,0\to 1} < 0$. $\omega_{q,1\to 2}$ is the qubit transition frequency between the $|1\rangle$ and $|2\rangle$ levels, and $\omega_{q,0\to 1}$ is the transition frequency between the $|0\rangle$ and $|1\rangle$ levels.

The dispersive shift, χ introduced in Sec. 2.2.1 can be expressed in terms of the transmon nonlinearity, α. Going beyond the two-level approximation, we modify this shift for a system with three levels $|g\rangle$, $|e\rangle$, and $|f\rangle$, where $|f\rangle$ is the second excited state [13]. Note that we are

using $|0\rangle$, $|1\rangle$, and $|2\rangle$ interchangeably with $|g\rangle$, $|e\rangle$, and $|f\rangle$.

$$\chi = \chi_{ge} + \frac{\chi_{ef}}{2} = -\frac{g_{ge}^2}{\Delta}\left(\frac{1}{1 + \Delta/\alpha}\right). \qquad (3.20)$$

We see that for a transmon qubit (which has a negative α), the dispersive shift depends on detuning [13]. We can observe that in the limit of $\alpha \to \infty$, we recover the two-level system limit.

We should note that for the transmon, Eq. 2.17 yields a photon number n_c, which if exceeded, would cause the Taylor expansion to diverge. This number imposes an upper limit on the input power that can be used for QND measurements [12, 13, 33, 34].

$$n_c \equiv \left(\frac{\Delta}{2g}\right)^2 \qquad (3.21)$$

If the power is too large, then the cavity and qubit decouple from each other, and the cavity shifts back to its bare frequency. This is sometimes referred to as the "punch-out regime" [57], as the transmon would be "punched out" to higher energy levels..

Now to find E_J, one can use the Ambegaokar-Baratoff relationship [11, 51, 58]

$$E_J = \frac{1}{2}\frac{h}{(2e)^2}\frac{1}{R_N}\Delta_s. \qquad (3.22)$$

As before, Δ_s is the superconducting energy gap. R_N is the resistance across a junction when the metal is in its normal state. This value can be found by probing junctions using a digital multimeter (DMM) at room temperature. Hence, it is easy to estimate E_J according to Eq. 3.22. For a transmon qubit, the qubit frequency is given by $\omega_q \approx \sqrt{8E_J E_C}$.

To reduce susceptibility to charge noise, the transmon operates in the $E_J \gg E_C$ regime
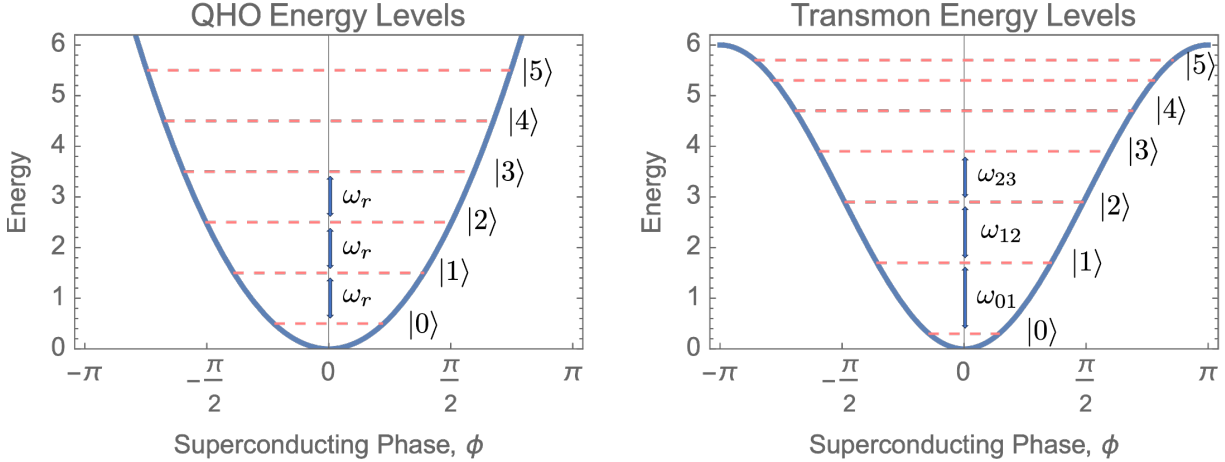
Figure 3.3: **Energy Levels for a Quantum Harmonic Oscillator vs. a Transmon Qubit** Figure on the left shows the energy levels for a QHO, where all the energy levels are resonant with one another. Figure on the right shows the energy levels for the transmon qubit, which is an anharmonic oscillator. As we go to higher levels, transition frequencies decrease by $n\alpha$ for $|n\rangle \rightarrow |n+1\rangle$ transitions.

[20]. Earlier realizations of superconducting qubits [59] such as the Cooper-pair box (CPB) [60], which operate outside this regime, were strongly affected by charge noise and had inferior relaxation times (T_1). The qubit relaxation time is the time that it takes for the qubit to relax from its excited state to its ground state due to exchange of energy between the qubit and its environment [13].

Charge noise is strongest when there is a large charge dispersion. This causes the qubit frequency to change more as the gate charge fluctuates [20]. The transmon is delocalized in charge space, and therefore it is immune to local charge noise. However, even the transmon has some sensitivity to charge noise, and its T_1 decreases when there is more charge fluctuations [61].

In the transmon regime, the charge dispersion decreases exponentially in E_J/E_C. However, its anharmonicty only goes down as a slow power law compared to the CPB [20]. This ensures that we still have the necessary anharmonicity to approximate the transmon as a two-level system.

3.2.2 Tunable-Frequency Transmon

In the previous section, we assumed that the transmon qubit in question consisted of one Josephson junction shunted by a capacitor. We will now explore what happens when we have a "split" transmon loop as shown in Fig. 3.4. This setup, called a Superconducting Quantum Interference Device (SQUID), can be used for tuning the frequency of the qubit. To do so, we will thread a magnetic flux through the SQUID loop, and observe a change in the transmon frequency [62].
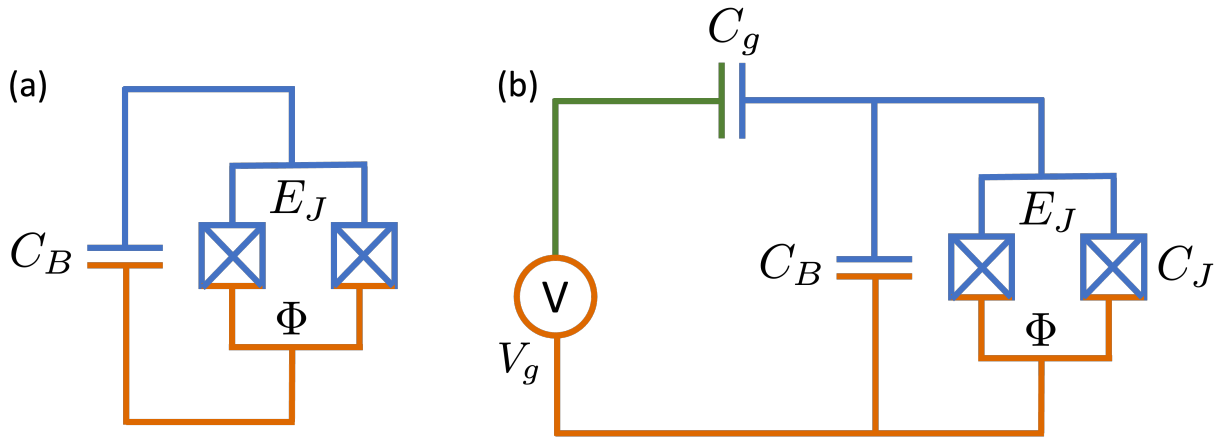

Figure 3.4: **Circuit Representation of a Frequency Tunable Transmon Qubit a-** This figure shows the circuit illustration of a Transmon qubit that is frequency tunable. It contains two Josephson junctions shunted with a capacitor, each shown by an "x" in a box. The loop that the two Josephson junctions form is referred to as a "Superconducting Quantum Interference Device (SQUID)" loop. **b-** The capacitance network of a tunable transmon qubit coupled to a ground plane and a center-pin. C_B is the effective shunting capacitance, C_g is the gate capacitance, and C_J is the self capacitance of the Josephson junctions. We define the total capacitance as $C_\Sigma = C_B + C_g + C_J$. Panel **b** inspired by Koch et al. [20].

We can mathematically formulate this flux-tuning by assuming that now there is a current I_1 through the first junction, and a current I_2 through the second junction, so that $I_{tot} = I_1 + I_2$. The two junctions may have different E_J energies if they are not identical, and now we define a parameter $\gamma = E_{J,2}/E_{J,1}$ as the ratio of the two Josephson energies. Now we can use this in

addition to the DC Josephson effect described in Eq. 3.15 and write the total current [51]

$$I_{tot} = I_{c,1} \sin{(\phi_1)} + \gamma I_{c,1} \sin{(\phi_2)} \,. \tag{3.23}$$

We also define a "junction asymmetry" parameter $d \equiv \frac{E_{J,2}-E_{J,1}}{E_{J,2}+E_{J,1}}$ [13]. If we introduce a reduced external flux to the circuit $\phi_{ext} = 2\pi\Phi_{ext}/\Phi_0$, the total flux across the inductive components would become $\phi_1 - \phi_2 + \phi_{ext} = 2\pi n$, where n is an integer [13, 20]. This is due to the fact that the phase in a superconducting loop is definite and unique at every point, so that the total phase shift take values that are multiples of 2π [62, 63]. We can now define an effective phase difference $\varphi = \frac{\phi_1+\phi_2}{2}$ and write the junction Hamiltonian as [20]

$$\begin{aligned}
\hat{H}_J &= -\left(E_{J,1} + E_{J,2}\right) \left[\cos\left(\frac{\phi_{ext}}{2}\right) \cos{(\hat{\varphi})} + d\sin\left(\frac{\phi_{ext}}{2}\right) \sin{(\hat{\varphi})}\right] \\
&= \underbrace{-\left(E_{J,1} + E_{J,2}\right) \cos\left(\frac{\phi_{ext}}{2}\right) \sqrt{1 + d^2 \tan^2\left(\frac{\phi_{ext}}{2}\right)}}_{E'_J} \cos{(\hat{\varphi} - \varphi_0)} \,,
\end{aligned} \tag{3.24}$$

where $\varphi_0 = \pi\frac{\Phi}{\Phi_0} \tan^{-1}(d)$.

We have now shown that E_J becomes E'_J, and that the new Josephson energy can now be altered using an external magnetic flux [20]. In the case where the SQUID loop is symmetric and the junctions are identical, $d = 0$ and $\gamma = 1$ as $E_{J,1} = E_{J,2}$. Then we would simply get $E'_J = 2E_{J,1}\cos{(\phi_{ext}/2)}$, which ensures maximum flux tunability [64]. However, this also increases susceptibility to flux noise. This occurs when noise in the external magnetic field causes fluctuations in E_J [13, 20, 65, 66]. The flux noise, which is generally of the type $1/f$ noise, is discussed in depth in Ref. [67].

The magnetic flux noise affects the pure dephasing time of the qubit T_φ, except where when the $\Phi_{ext} = n\Phi_0$, where n is an integer. This points, referred to as "integer flux" points, is where the qubit spectrum reaches its minimum and becomes insensitive to flux noise to the first order [13]. Pure dephasing refers to the loss of phase coherence in a qubit, without taking into consideration qubit energy relaxation [68].

3.3 Dependence of Coupling Strength on Frequency

In this section, we discuss the coupling strength between a qubit and a CPW resonator, g, and its dependence on frequency. In this treatment, the qubit and the CPW resonator are capacitively coupled. While we usually think of capacitance forming between parallel plates of metal, it can also occur between sheets of metal adjacent to one another, as seen in Fig. 3.5-a. In Fig. 3.5-b we see a transmon qubit coupled to a CPW resonator. In both figures, there is a capacitance between the metal islands shown in yellow and blue. There is also an effective capacitance between the transmon paddles and the center-pin of the CPW resonator, which couples them to one another, and allows for light-matter interactions.

To find the coupling strength between the qubit and the cavity, we start from the generalized Jaynes-Cummings Hamiltonian seen in Eq. 2.36, re-writing it in the basis of uncoupled transmon states $|i\rangle$ [20]

$$\hat{H} = \hbar\omega_r\hat{a}^\dagger\hat{a} + \hbar\sum_j \omega_j |j\rangle\langle j| + \hbar\sum_{i,j} g_{i,j} |i\rangle\langle j| \left(\hat{a} + \hat{a}^\dagger\right), \tag{3.25}$$

and find that the coupling energies can be written as

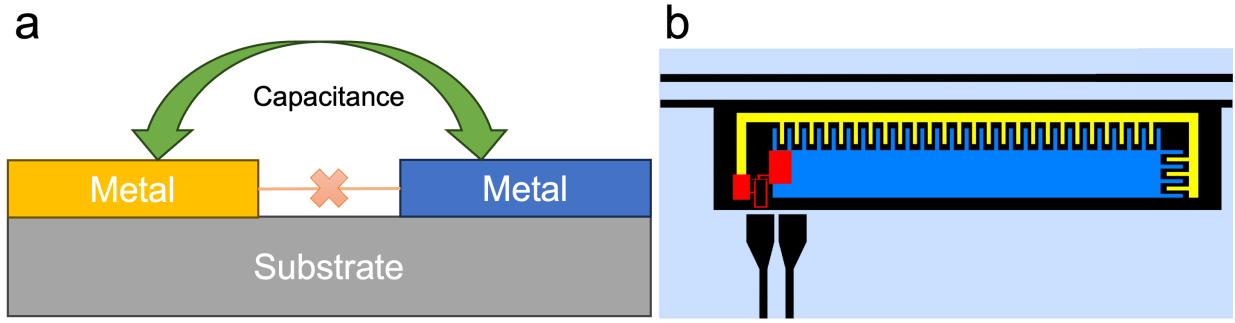$$\hbar g_{i,j} = 2\beta e V_{rms}^0 \langle i|\hat{n}|j\rangle, \tag{3.26}$$

Figure 3.5: **Capacitively Coupled Qubit and CPW Resonator a-** While we normally think of capacitance between two parallel metal plates, there is also a capacitance between two thin metal islands that are flat on a substrate. **b-** The light blue regions indicate metal and the black region indicates dielectric gap. The narrow strip of light blue represents a small portion of the center-pin of the CPW resonator. The yellow and the dark blue regions show the capacitor paddles for the transmon, which are also made of metal. The red region is where the SQUID loop has been placed. There is a capacitance between the yellow and dark blue transmon paddles and the light blue center-pin of the CPW resonator, similar to that seen in panel a. The effective capacitance between the transmon and the CPW resonator couples them to one another, and allows for light-matter interactions.

where $\beta = C_g/C_\Sigma$ is the ratio of the gate capacitance to the total capacitance. The gate capacitance is defined as the effective capacitance between the transmon and the voltage source (see Fig.3.4-b). For a resonator of frequency $\omega_r = 1/\sqrt{L_r C_r}$, the V_{rms}^0, which is the root mean square (RMS) voltage of the local oscillator [20], is given by

$$V_{rms}^0 = \sqrt{\frac{\hbar \omega_r}{2 C_r}}. \tag{3.27}$$

Similar to Ch. 2.2, we perform RWA on the Hamiltonian in Eq. 3.25. We will also simplify Eq. 3.26 by writing

$$\hat{n} = -i \left(\frac{E_J}{8 E_C} \right)^{1/4} \left(\hat{b} - \hat{b}^\dagger \right) / \sqrt{2}, \tag{3.28}$$

so that

$$|\langle j+1|n|j\rangle| \simeq \sqrt{\frac{j+1}{2}} \left(\frac{E_J}{8E_C}\right)^{1/4}. \tag{3.29}$$

But, we remember that for a transmon qubit, $\omega_q = \sqrt{8E_J E_C}$, so we can write

$$\hbar g = 2\beta e \sqrt{\frac{\hbar \omega_r}{2C_r}} \sqrt{\frac{\omega_q}{8E_C}}, \tag{3.30}$$

clearly showing the dependence of coupling on frequency, so that $g \propto \sqrt{\omega_r \omega_q}$ [69].

Coupling strength varies based on where along the resonator the qubit is placed. This is because the voltage profile of the resonator is a function of position, and for a resonator that is open at both ends, the profile is sinusoidal. Thus, for a half-wave resonator and a qubit placed at Δx along that resonator, coupling varies according to [70].

$$g(\Delta x) = g_{max} \sin\left(\pi \frac{\Delta x + x_0}{\ell_r}\right), \tag{3.31}$$

where ℓ_r is the length of the resonator, g_{max} is the maximum coupling.

3.4   Hopping Strength between Transmission Line Resonators

In this section, we are considering a transmission line resonator coupled to other systems on its either side, and calculating the photon hopping between them. This calculation is mainly based on the work of Nunnenkamp et al. found in Ref. [42]. We start by writing the Lagrangian for a system that has a transmission line resonator capacitively coupled to another one on its left and one on its right, similar to that in Fig. 3.6.

We treat these resonators as a series of N LC oscillators, similar to Sec. 3.1. In the lumped
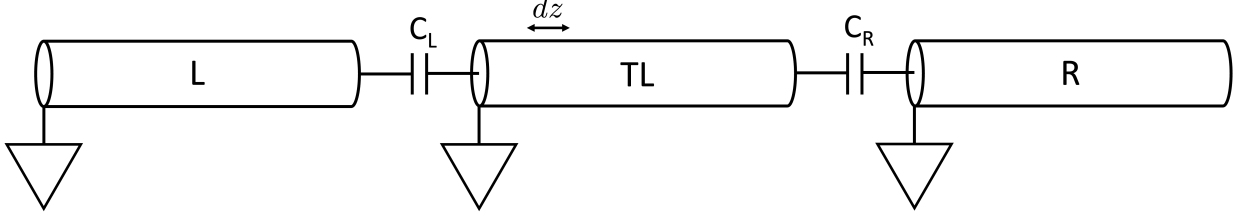
Figure 3.6: **Capacitively Coupled Transmission Lines** A transmission line labeled TL, is capacitively coupled to other transmission lines on either side of it. The resonator on the left (right) of it is called L (R). The coupling capacitance on the left (right) side is labeled C_L (C_R).

element approximation of the CPW resonator, we assume that the oscillators have a capacitance of cdz and an inductance of ℓdz , where c and ℓ are the capacitance per unit length and the inductance per unit length, respectively [71]. The general Lagrangian of a transmission line coupled to two arbitrary elements $\mathcal{L}'_L$ and $\mathcal{L}'_R$ on its either end is given by [71]

$$
\begin{aligned}
\mathcal{L} = {} & \mathcal{L}'_L + \mathcal{L}'_R + \frac{1}{2}C_L\left(\dot{\phi}_1 - \dot{\phi}_L\right)^2 + \frac{1}{2}C_R\left(\dot{\phi}_N - \dot{\phi}_R\right)^2 + \frac{1}{2}\sum_{i=1}^{N}cdz\dot{\phi}_i^2 - \frac{1}{2\ell dz}\sum_{i=2}^{N}(\phi_i - \phi_{i-1})^2 \\
= {} & \underbrace{\sum_{\alpha=L,R}\left(\mathcal{L}'_\alpha + \frac{1}{2}C_\alpha\dot{\phi}_\alpha^2\right)}_{\mathcal{L}_L+\mathcal{L}_R} - \underbrace{C_L\dot{\phi}_1\dot{\phi}_L - C_R\dot{\phi}_N\dot{\phi}_R}_{\mathcal{L}_{int}} \\
& + \underbrace{\frac{1}{2}C_L\dot{\phi}_1^2 + \frac{1}{2}C_R\dot{\phi}_N^2 + \frac{1}{2}\sum_{i=1}^{N}cdz\dot{\phi}_i^2 - \frac{1}{2\ell dz}\sum_{i=2}^{N}(\phi_i - \phi_{i-1})^2}_{\mathcal{L}_{TL}} .
\end{aligned}
$$

(3.32)

Here, L (R) represents the element on the left (right) of the transmission line, and is coupled to it with coupling strength C_L (C_R). ϕ_L and ϕ_R are the generalized flux variables adjacent to the transmission line resonator, while ϕ_1 and ϕ_N are the generalized flux variables at either end of it.

In our lattices, we couple transmission line resonators to one another. So now we will assume that the L and R elements, whose Lagrangians are given by $\mathcal{L}_L$ and $\mathcal{L}_R$, are also transmission lines. We also further simplify the Lagrangian above by assuming that $C_R = C_L \equiv C_c$

43

is the coupling capacitance between adjacent resonator pairs, and defining $\Phi^T = (\phi_1, \cdots, \phi_N)$. Similar to Sec. 3.1, $\dot{\Phi}$ is the voltage profile in the resonator. By imposing a continuum limit and assuming that all the elements in the system are transmission line resonators, we can now modify the Lagrangian in Eq. 3.32 [42]

$$\mathcal{L} = \frac{1}{2} C_c \sum_j \dot{\Phi}_j^2 \Big|_{ends} + \frac{c}{2} \sum_j \int dz \left(\dot{\Phi}_j^2 - \frac{1}{\ell c} \left(\partial_x \Phi_j \right)^2 \right) - C_c \sum_{\langle j,j' \rangle} \dot{\Phi}_j \dot{\Phi}'_j \Big|_{ends}, \qquad (3.33)$$

where j denotes the resonator index, and $\langle j, j' \rangle$ are nearest neighbor resonators. We find that the internal eigenmodes that diagonalize the Lagrangian are of the form [42, 71]

$$\Phi_j(x,t) = \sum_\mu \xi_{j\mu}(t) e^{i\omega_\mu t} \phi_{j\mu}(x), \qquad (3.34)$$

and yield [42]

$$\mathcal{L} = \frac{1}{2} \sum_{j,\mu} \left(\dot{\xi}_{j\mu}^2 - \omega_\mu^2 \xi_{j\mu}^2 \right) - C_c \sum_{\langle j,j' \rangle} \sum_{\langle \mu,\mu' \rangle} \phi_{j\mu}(x) \phi_{j'\mu'}(x') \Big|_{ends} \dot{\xi}_{j\mu} \dot{\xi}_{j'\mu'}, \qquad (3.35)$$

where μ denotes mode indices. Typically the coupling capacitance is small, such that $C_c \ll C_{res} = cdz$. In such a case, we can look at a single mode, and therefore one μ only. For convenience, we can write the Lagrangian in matrix notation. Let us define a matrix T to contain the coupling between resonators [71]

$$T_{jj'} = \delta_{\langle jj' \rangle} C_c \phi_j(x) \phi_{j'}(x') \Big|_{ends}, \qquad (3.36)$$

where $\delta_{\langle jj' \rangle}$ is the adjacency matrix, where all the elements are 0, except when two resonators

are capacitively coupled to each other, in which case the matrix element is 1. The resulting Lagrangian using the equation above is [42]

$$\mathcal{L} = \frac{1}{2}\dot{\vec{\xi}} \cdot (1-T)\dot{\vec{\xi}} - \frac{1}{2}\omega^2\vec{\xi}^2. \tag{3.37}$$

We can perform Legendre transformation to find the Hamiltonian. Note that if a Lagrangian is a function of $(\vec{q}, \dot{\vec{q}}, t)$, the Hamiltonian will be a function of $(\vec{p} = \frac{\partial \mathcal{L}}{\partial \dot{\vec{q}}}, \vec{q}, t)$. Recall that the Legendre transform is given by $\mathcal{H}(\vec{p}, \vec{q}, t) = \sum_{i=1}^{N} p_i \dot{q}_i - \mathcal{L}(\vec{q}, \dot{\vec{q}}, t)$ [72]. In our case, let us write the Hamiltonian in terms of conjugate pairs $\vec{\xi}$ and $\vec{\pi}$, where $\vec{\pi}$ contains conjugate momenta $\pi_j = \partial \mathcal{L}/\partial \dot{\xi}_j$. Therefore, $\dot{\vec{\xi}} = (1-T)^{-1}\vec{\pi}$. So the Hamiltonian simply becomes [71]

$$\begin{aligned}
\mathcal{H} &= \vec{\pi}\dot{\vec{\xi}} - \mathcal{L} \\
&= \frac{1}{2}\vec{\pi}(1-T)^{-1}\vec{\pi} + \frac{1}{2}\omega^2\vec{\xi}^2 \\
&\approx \frac{1}{2}\left(\vec{\pi}^2 + \vec{\pi} \cdot T\vec{\pi} + \omega^2\vec{\xi}^2\right).
\end{aligned} \tag{3.38}$$

The approximation performed in the last line is simply using a Taylor series expansion for $\frac{1}{1-T}$. Now we can write the quantized Hamiltonian by writing ξ_j and π_j in terms of creation and annihilation operators: $\xi_j \to \frac{\hat{a}_j + \hat{a}_j^\dagger}{\sqrt{2\omega}}$ and $\pi_j \to i\sqrt{\frac{\omega}{2}}\left(\hat{a}_j^\dagger - \hat{a}_j\right)$ [42]

$$\begin{aligned}
\hat{H} &= \frac{\omega}{4}\sum_j\left(-\left(\hat{a}_j^\dagger - \hat{a}_j\right)^2 + \left(\hat{a}_j^\dagger + \hat{a}_j\right)^2\right) - \frac{\omega}{4}\sum_{\langle j,j'\rangle} C_c\left(\phi_j(x)\phi_{j'}(x')\right)\Big|_{ends}\left(\hat{a}_j^\dagger - \hat{a}_j\right)^2 \\
&= \omega\sum_j \hat{a}_j^\dagger\hat{a}_j - \frac{\omega}{4}C_c\left(\phi_j(x)\phi_{j'}(x')\right)\Big|_{ends}\sum_{\langle j,j'\rangle}\left(\hat{a}_j^\dagger\hat{a}_{j'} + \hat{a}_{j'}^\dagger\hat{a}_j\right) + \text{h.c.} \\
&= \omega\sum_j \hat{a}_j^\dagger\hat{a}_j - t\sum_{\langle j,j'\rangle}\left(\hat{a}_j^\dagger\hat{a}_{j'} + \hat{a}_{j'}^\dagger\hat{a}_j\right) + \text{h.c.}.
\end{aligned} \tag{3.39}$$

We can now extract the amplitude and sign of photon hopping for capacitively coupled resonators from t, the coefficient of $\hat{a}_j^\dagger \hat{a}_{j'}$. It is useful to express this hopping in terms of the frequency of the resonator $\nu = \omega/2\pi$. The sign of hopping is equal to the sign of $\phi_j(x)\phi_{j'}(x')\big|_{ends}$, and its amplitude is [42]

$$
\begin{aligned}
\frac{t}{2\pi} &= \frac{1}{2}\nu C_c |\phi_j(x)\phi_{j'}(x')|\Big|_{ends} \\
&\approx \frac{C_c}{C_{res}}\nu,
\end{aligned}
\tag{3.40}
$$

In this chapter, we formulated the CPW resonator as a series of LC oscillators and derived its Hamiltonian. We then studied the transmon, which is a non-linear resonator that we use as our qubit. We saw that the coupling strength between a transmon qubit and a CPW resonator depends on their frequencies. Lastly, we calculated the photon hopping strength for a system of coupled transmission lines. Now that we are familiar with the theoretical background for these elements, we can discuss the fabrication and measurement of such systems. In Ch. 4, we first explain the general fabrication process for making CPW resonators, lattices, and transmons. We then explain the setup of our dilution refrigerator, study measurement chains, and explain how these measurements work. Lastly, we discuss certain troubleshooting measures that we took when collecting data.

Chapter 4: Device Fabrication, Apparatus, and Measurement

4.1 Fabrication Overview

The fabrication of such a large device takes time, patience, and state-of-the-art equipment. The fabrication of this device consisted of three main steps. The first step is to use photo-lithography to define larger features. This includes the resonators, coupling capacitors, qubit pockets, and alignment marks used for the next step, which is electron beam (e-beam) lithography. This next step is used to define the Josephson junctions. Due to their small size, Josephson junctions cannot be defined using photo-lithography, as the resolution of the machine is only $1~\mu$m. After writing the junctions using e-beam lithography, we perform an angled Aluminum deposition from two directions to make the junctions. After fabrication, a chip is prepared for measurement by wire-bonding it to a customized PCB board that has standard SMA connectors. The chip is protected using copper packaging. In the next three subsections we will take a closer look at each of these steps and the challenges they pose. Detailed fabrication recipes can be found in Appendix A.

4.1.1 Photo-Lithography

Photo-lithography works by exposing a polymer, called photo-resist, to UV light. The chemical properties of the resist change during the exposure, allowing for selective removal to define the desired pattern. One will start with a substrate that is coated in a layer of metal. In our case, we send out our sapphire wafers to Star Cryoelectronics and they deposit tantalum on the substrate.

After dicing the wafer into small chips, we spin-coat a chip in a positive photo-resist. We then expose the regions from which we wish to remove the metal with UV light. Once we immerse the chips into a developer, the photo-resist is removed where it was exposed by light. We then immerse the chip in acid to remove the metal where the photo-resist was removed. The rest of the chip is protected by the remaining photo-resist. Fig. 4.1 shows a cartoon image of this process.

The actual exposure of the photo-resist can be done using two different instruments. One is a conventional mask-aligner, which uses a photo-mask (a glass metal with patterned metal on it, acting as a stencil), as well as a UV light bulb to form a shadow pattern on the resist. The other, is a direct-write maskless aligner made by Heidelberg (model MLA150). This system uses a laser to directly expose the resist, removing the need for a photo-mask. The MLA150 has a better resolution compared to the mask-aligner. It also allows the user to control the exposure dosage with precision. While the mask aligner allows the user to set the exposure time, the MLA150 lets the user to set the dosage directly in software. In Fig. 4.2 we see the results of exposure by the mask aligner on the left, and the MLA150 on the right. The sharp edges are rounded in the chip made by the mask aligner, while they look crisp in the one made using the MLA150.
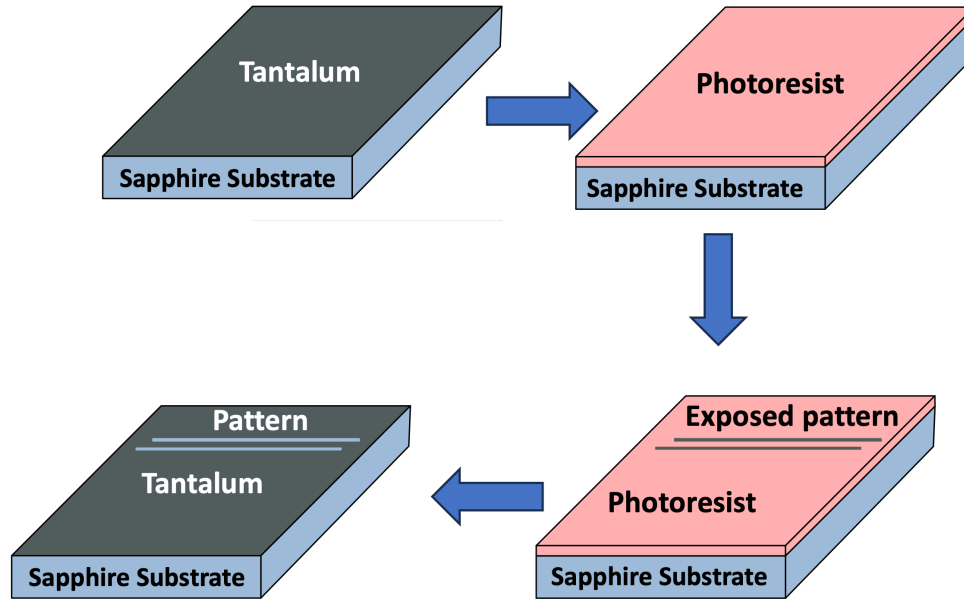
48

Figure 4.1: **Photo-Lithography** To define patterns larger than 1 μm one can use photo-lithography. We start preparing and cleaning a sapphire substrate coated in tantalum. We then spin photo-resist on the sample and bake it. Then, we expose the regions from which we desire metal to be removed using UV light, and we develop the resist in a "developer" chemical to remove the resist in those regions. Lastly, we etch the metal using an acid (HF in this case). The remaining resist will protect the metal on the rest of the chip. After etching, we remove the remaining photoresist using solvents.

Photo-lithography of such a large chip poses challenges other than dose-optimization. One challenge is that when one spins photo-resist on a chip, the photo-resist becomes thicker on the edges of the chip. This phenomenon, called the edge-bead, depends on the spin speed and the viscosity of the resist. The quasi-1D lattice device is fabricated on a 1 inch $\times$ 1 inch chip, and the design extends to the edges of the chip. Due to edge-beads, the pattern was not being exposed all the way through closer to the edges of the chip, as it was thicker and needed a larger dosage. To overcome this issue, I manually performed a proximity correction, and used a larger dose for the coupling capacitor at the bottom-left of the chip. Fig. 4.3 is of an early attempt of fabricating this device, where the gaps in the three-way coupler were not fully cleared.

Such a large device needs to be fabricated in an extremely clean environment. Otherwise,
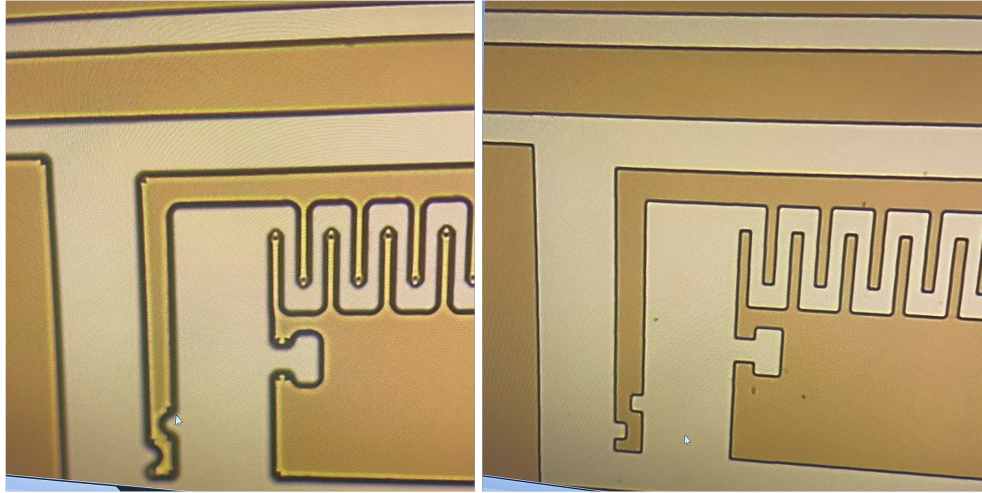
Figure 4.2: **Photo-Lithography Resolution Comparison** The same pattern was created using a mask aligner, shown on the left, and using the Heidelberg MLA150 on the right. The corners of the pattern are rounded due to over-exposure and poor resolution when a mask aligner was used. The finer resolution and the stable dosage in the MLA150 allows one to create a pattern that has less variations compared to the CAD design. The darker tan region is made of Tantalum with photo-resist on top, and the lighter areas only contain bare sapphire with photo-resist.

dust particles can land on the chip and prevent photo-lithography from exposing all desired areas.

Fig. 4.4 shows a CPW resonator whose center-pin is shorted to the ground-plane, as a dust particle on the mask prevented the defective area from being exposed. The dark region is bare sapphire, while the lighter region is made of tantalum. As such, it is important not to take the chip out of the clean-room before photo-lithography is completed. One should also take care to clean the chip (and the mask, if using the mask-aligner) properly. The cleaning procedure is outlined in Appendix A. The mask can be cleaned using acetone and isopropanol.

4.1.2   e-Beam Lithography and Double-Angle Evaporation

e-beam Lithography is used in conjunction with a double-angle evaporation to create Josephson junctions. The process is similar to photo-lithography. However, instead of UV rays, one uses beams of electrons to clear the e-beam resist.
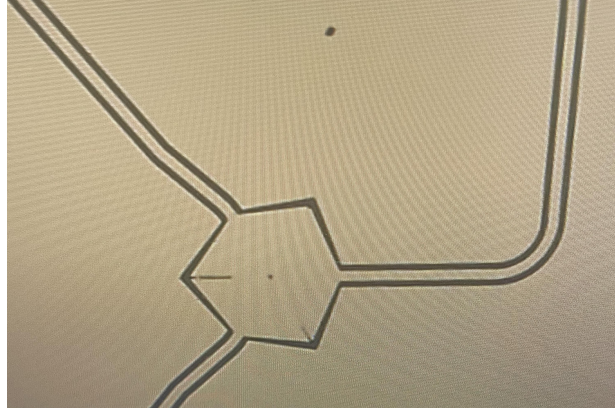
Figure 4.3: **Edge-Bead Effect** Thicker areas of resist that form on the edges of the chip, known as edge-beads, change the dosage required for clearing patterns in the resist. This pattern is on the edge of the chip, and we used the dosage required for clearing resist at its usual thickness at the center of the chip. However, the three lines in the center of the design were not fully cleared. It is possible to see portions of the lines that were cleared. These lines are very fine (2 μm in thickness), and the dose was too small to clear them through the edge-bead.

There are two types of Josephson junctions, and their methods of fabrication differ slightly from each other. The first type, called the Manhattan junction, is more forgiving towards fabrication errors and variations in dosage. The second type, called the Dolan bridge, while being more difficult to fabricate, is useful when making other types of qubits that require many Josephson junctions to be in series with one another. While we will not discuss such qubits (e.g. the fluxonium), it is important to understand their method of fabrication, as they are becoming more popular due to their insensitivity to offset charges [49]. This helps the fluxonium have long decoherence times, which in certain regimes exceeds 1.4 ms [73]. Another lure of the fluxonium is its large anharmonicity [49].

The Manhattan junction simply consists of two aluminum fingers crossing one another at a 90 degree angle, with a layer of AlOx in between them. One first spins a stack of MMA and PMMA (two types of e-beam resists with different clearing energies) on the chip, and then clears the desired areas using e-beam lithography. Then by evaporating aluminum in the cleared
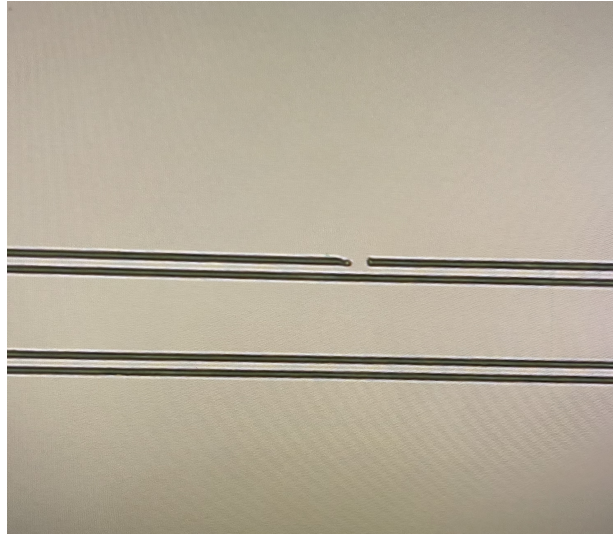
51

Figure 4.4: **Effect of Dust in Photo-Lithography** Here we see portions of two CPW resonators parallel to each other. The lighter regions are made of tantalum, and the dark areas are the CPW gaps made of bare sapphire. The uppermost CPW gap was not fully cleared, and as a result, the CPW center-pin was shorted to the ground plane of the chip. The defect in the gap was formed due to a dust particle preventing that small region of resist from being exposed to UV light.

regions, one can make Josephson junctions. This is achieved by evaporating aluminum along the first finger, letting oxygen in to form the insulating AlOx layer, and then rotating the chip to evaporate aluminum along the second finger. The small square where the two fingers overlap forms the Josephson junction. The area of interest is shown with a dark blue circle in the left hand side image in Fig. 4.5.

The reason for using a stack of MMA and PMMA is that it allows one to form "undercut" regions, meaning that the MMA region is cleared, while the PMMA remains hovering over the undercut region. When making a Manhattan junction, the undercut region prevents aluminum from creeping up the side walls during evaporation. However, the purpose of the undercut is two-fold when making a Dolan bridge.

The Dolan bridge is formed by making a floating resist bridge by clearing out the MMA underneath a section of PMMA, and using its shadow to perform the double-angle evaporation.
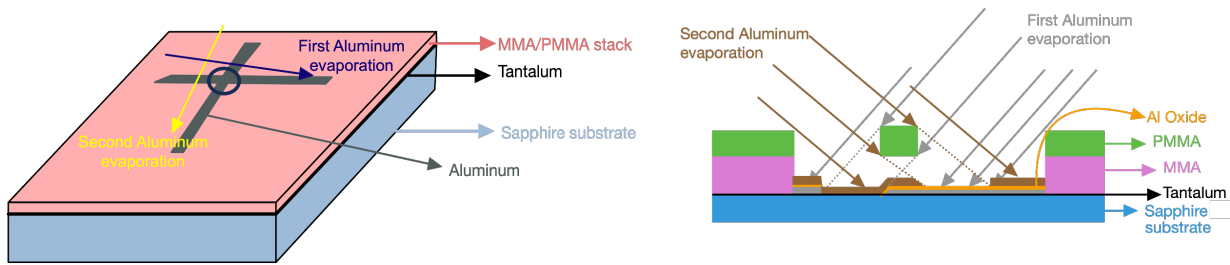
Figure 4.5: **Dolan Bridge vs. Manhattan Junction** This figure shows the double-angle evaporation that forms Josephson junctions. The panel on the left shows evaporation for a Manhattan style junction. For a Manhattan junction, one clears two alleyways, perpendicular to one another, in the resist, then evaporates aluminum along each of them. After depositing the first layer of aluminum, we allow oxygen into the system to form the insulating layer, made of aluminum oxide. The junction forms in the region circled in dark blue. In the panel on the right we see the evaporation method used for making Dolan bridge junctions. For this type of junction, one creates an undercut in the resist. Then evaporating from two opposite directions we can form a Josephson junction in the undercut region, under the green piece of resist that is semi-floating.

The Josephson junction forms below the PMMA hovering over the undercut region. In the right hand side image in Fig. 4.5 we show the two directions of evaporation forming a Josephson junction in the undercut region. Fig. 4.6 is an SEM image of a Dolan bridge I made using the described method. The Josephson junction itself is outlined with a white rectangle.

When doing e-beam lithography, one can only use up to four alignment marks at a time. While using the same four alignment marks for different qubits would be fine on a smaller chip where the qubits are close to one another, chips larger than $10 \text{ mm} \times 10 \text{ mm}$ are more sensitive to alignment errors. However, by writing each qubit separately with the 4 alignment marks closest to it, we avoid misalignment between the qubit pocket and Josephson junctions. Fig. 4.7 shows the type of misalignment that can occur if all qubits are written in the same run, using the same four alignment marks. We can see that the junctions have run into the ground plane of the chip (lighter regions are tantalum, and darker regions are sapphire). For the lattice device discussed in
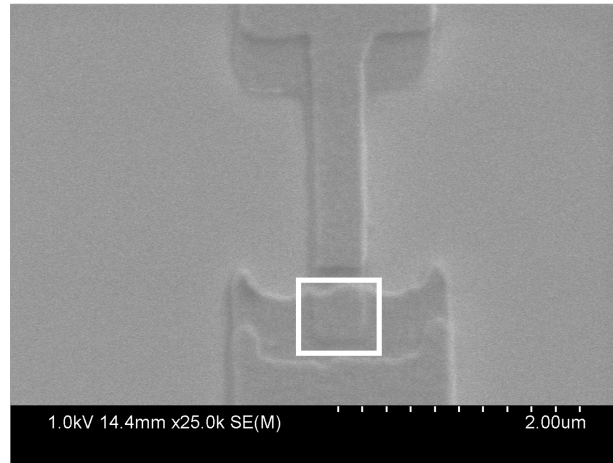
Figure 4.6: **SEM Image of a Josephson junction** SEM image of a Dolan bridge Josephson junction made by the author. The junction forms in the area highlighted with a white rectangle. The darker gray areas that are raised are made of aluminum, and the flat, lighter gray region is made of bare sapphire.

Ch. 5 (where the chip measures 1×1 inch^2), I place thirty-three alignment marks on the chips to avoid alignment issues.

It is important to keep in mind that during e-beam lithography there may be a build up of charge on the device. This charging effect would cause "breaks" in the write, as shown in Fig. 4.8. To prevent a build up of charges on insulating substrates, one needs to evaporate an anti-charging layer of metal on the MMA/PMMA resist stack before the e-beam write, and use the "anti-charging tab" in the e-beam lithography system to ground the chip to the machine.

4.1.3 Wire-Bonding and Packaging

Our chips are packaged in copper packaging, which creates excellent thermal contact between the chips and the dilution refrigerator. The chip is placed in a puck, connected to a printed circuit board (PCB) that is placed over it using wire-bonding, and covered by a copper lid. The packaged chip is then connected to the dilution refrigerator using a copper rod and adapter. Lastly,
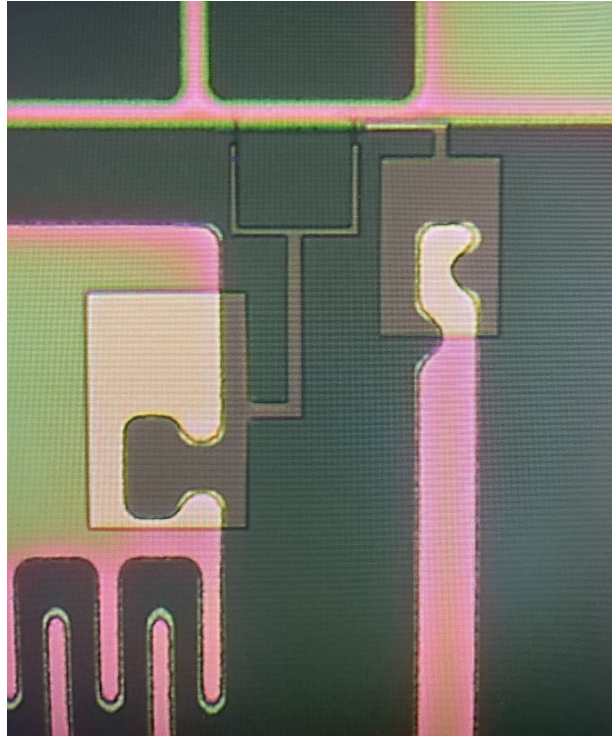
Figure 4.7: **Misalignment in the e-beam Layer** The qubits on a large chip (1×1 inch^2) were exposed in the same write, using the same four alignment marks, that were not very close to all the qubits. The uncertainty in the alignment is larger in such a situation, and the result was that the junctions overlapped with the ground plane of the chip due to this poor alignment. The junctions were meant to be in the dark green region, made of bare sapphire. For large designs it is essential to have a set of four alignment marks near each qubit, and write each qubit separately using the set of marks closest to it.

the setup is enclosed in an aluminum can and a μ-metal can to protect the device from stray magnetic fields. Fig. 4.9 shows different stages of packaging a chip, and includes the cross-sectional image of the three-dimensional CAD model for the assembly.

Wire-bonding is a process that uses sonic waves to adhere microscopic aluminum wires to other metal surfaces. We use wire-bonds across CPW resonators to connect different portions of the ground plane in order to eliminate slot-line modes. We also place wire-bonds connecting the ground plane of the PCB to that of the chip. Most importantly, we use wire-bonds to connect the input and output of the circuit to the PCB. In Fig. 4.10 we see stitch-like lines across two devices,
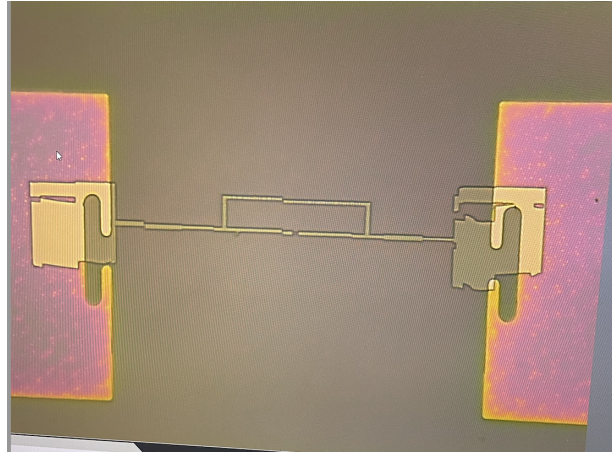
Figure 4.8: **Charging Effect in e-Beam Lithography** In this write, the chip did not contain an anti-charging layer of metal and was not grounded to the e-beam lithography system. Since the substrate (sapphire) is an insulator, charge was built up on the chip during the write and resulted in glitches in the pattern.

which are the wire-bonds.

A wire-bond that is 1 mil in diameter and 1 mm in length has an approximate inductance of 1 nH, and an impedance of $40\ \Omega$ at 6 GHz [74, 75]. When two wire-bonds are placed, slot-line modes are attenuated by ~ 4 dB for frequencies up to 30 GHz [74]. Hence, placing several wire-bonds can effectively suppress slot-line modes. It is important to keep in mind that the placement of wire-bonds is also important. Bonds that are placed in the center of a CPW resonator are more effective than those placed on the edges.

Once connected to a PCB and packaged in its copper packaging, a device is connected to the base-plate of the BF, then shielded by an aluminum can, and a μ-metal can to prevent stray magnetic fields from entering the device.
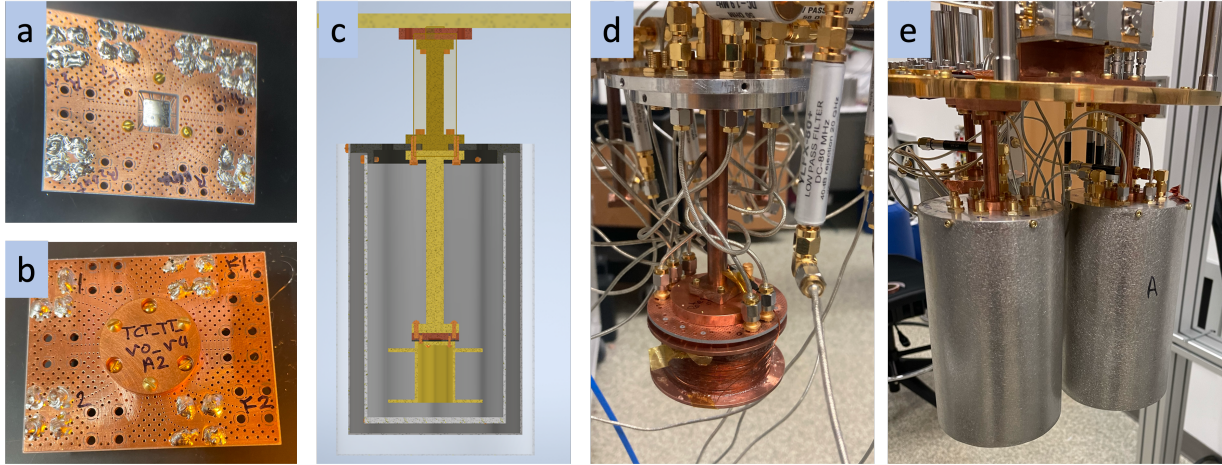
Figure 4.9: **Device Packaging a-** A chip placed in a puck and covered by a PCB. **b-** A similar setup to the one seen in Fig. **a** is covered by a copper lid. **c-** Cross section of a three-dimensional CAD model of the assembly. The horizontal plate at the top represents the base plate of the dilution refrigerator. From top to bottom, a rod connects to the outer μ-metal shield and the aluminum can. A longer rod is then attached to the inside of the cans, connecting the packaged chip to the rest of the setup. An optional magnet is placed at the bottom for flux-biasing the qubits. **d-** Image of the assembly inside the can. The puck, PCB, and magnet lid can be seen at the bottom of the image. **e-** The full assembly is connected to the base plate of the dilution refrigerator. Coaxial cables are routed from the lid of the cans to the dilution refrigerator.

4.2 Dilution Refrigerator Setup

The dilution refrigerator used for this project is a Blue Fors LD400. From here on, we will refer to this dilution refrigerator as BF.

The BF has a few different temperature stages, with various cooling mechanisms. The different stages are at approximately room temperature (RT), 50 K, 4 K, 1 K, 100 mK, and 15 mK. While the temperature of the base-plate, to which the devices are attached, is advertised to be around 15 mK, its actual reading often reaches 7 mK. The base temperature is achieved by the heat of mixing of a helium-3 and helium-4 mixture [76].

The BF has sixteen RF lines for input signal and four for output signal. The lines are made of semi-rigid stainless steel coaxial cables. We have set up 61 dB of attenuation on eight of the RF
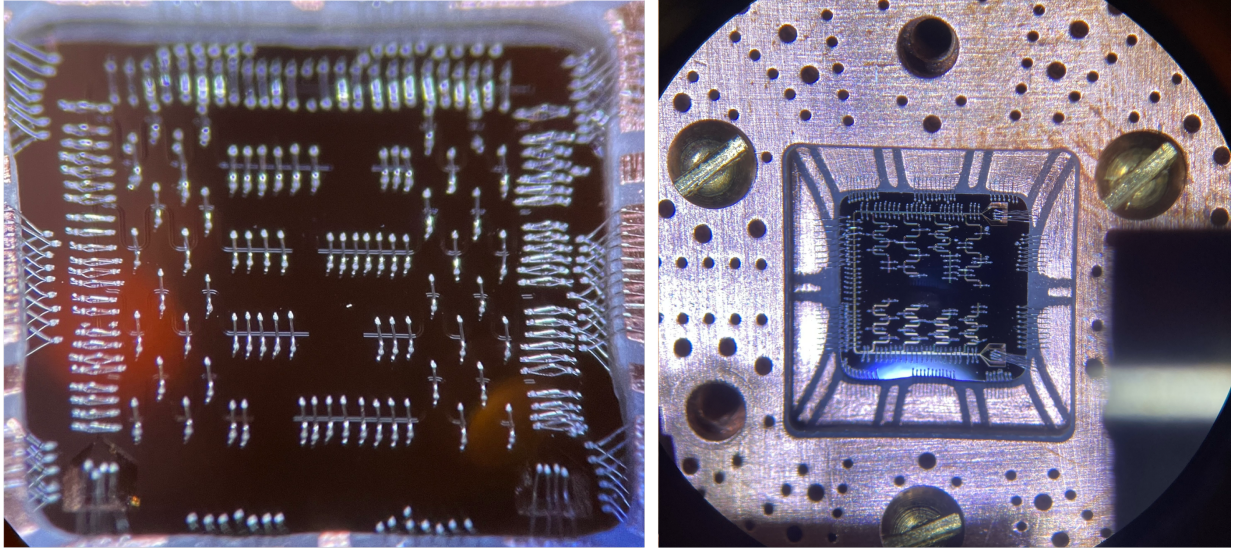
Figure 4.10: **Wire-Bonded Devices** Wire-bonds are fine threads of metal (aluminum in our case), that are placed on a chip using a wire-bonder. The wire-bonder uses sonic waves to make the metal thread adhere to the chip. In this figure we see two wire-bonded devices made by the author. The wire bonds are the light silver lines. They are used to connect a chip to a PCB for readout. Additional wire-bonds are placed to eliminate box modes, and ensure that different areas of the chip and the PCB are properly grounded to each other.

lines, which are used as input. Out of the remaining eight lines, four have 38 dB of attenuation, while the other four have only 32 dB of attenuation. These lines are used for flux biasing the devices, and we refer to them as flux aggresive (Fa) and flux mild (Fm) respectively. They are either attached directly to the flux bias lines (FBLs) of devices, or to the magnets that are used for frequency-tuning the qubits.

Each output line has a 1 dB attenuation at the 50 K stage, and a High Mobility Electron Transistor (HEMT) at the 4 K stage to amplify the signal. An isolator is placed on the output lines at the base-plate to prevent noise from the HEMT leaking back into the device.
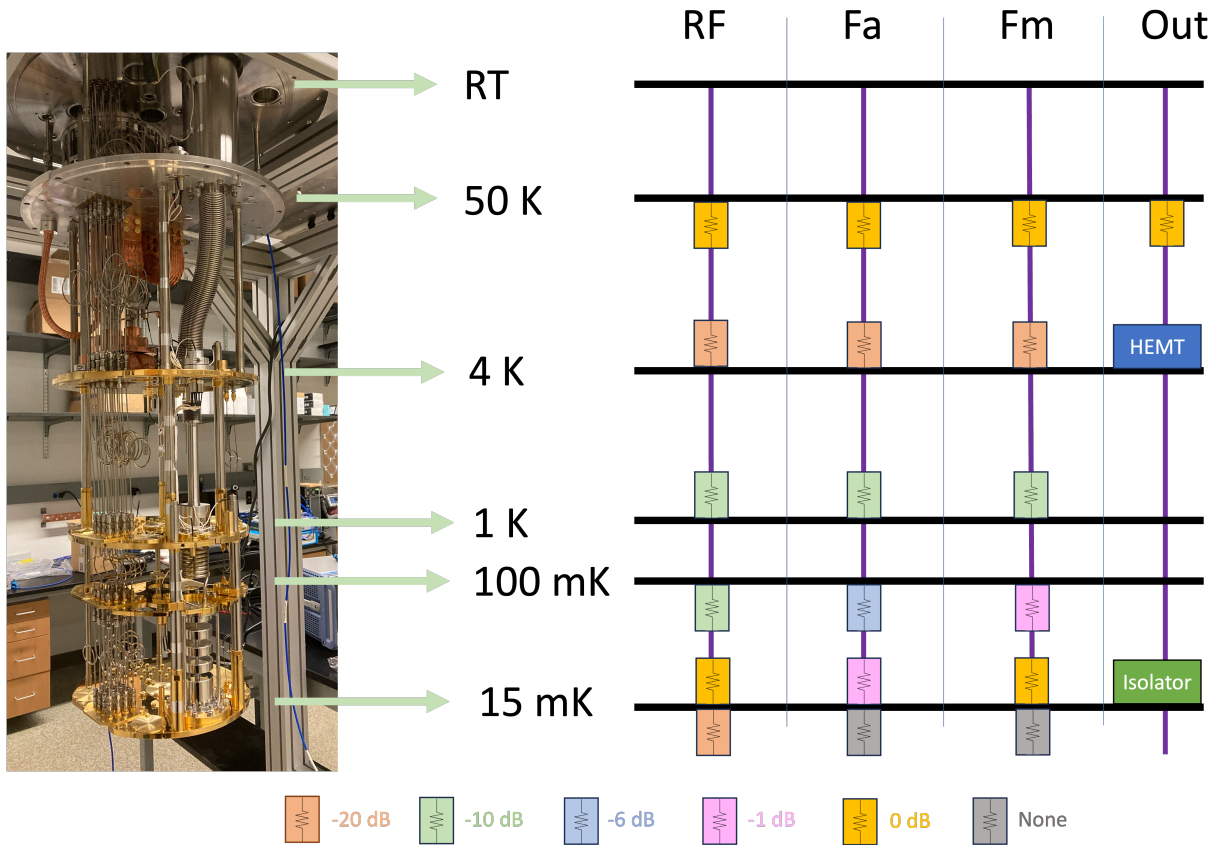
Figure 4.11: **Dilution Refrigerator Stages and Wiring** The panel on the left shows the inside of the BF dilution refrigerator. Each plate reaches a different temperature. All plates have been labeled with their corresponding temperatures. In the panel on the right, each horizontal black line represents the plate to which it is closest (the temperature labels are shared between both panels). The vertical dark purple lines represent coaxial cables. The attenuation at every stage is shown for RF line, flux bias lines, and output lines. Each color represents a different attenuation power, and the legend at the bottom shows the explicit values. We also see the HEMT and the isolator placed on each output line in this figure.

4.3   Measurement Chain

Circuit QED experiments make use of two general types of measurements: continuous wave (CW) and pulsed measurements. To perform the simpler CW measurement, which is used to collect the data from the lattice data, we use a Vector Network Analyzer (VNA). The VNA is a two or four channel piece of instrument, which generates signal from one port and reads out the

response through another port. Our specific VNA is a four channel Rhode and Schwarz model ZNB 20, and has a frequency range of 100 kHz - 20 GHz.

We measure the cavity response by performing an S21 measurement, which gives the amplitude and phase of a probe signal. For such measurements, one can make use of two ports, and perform transmission measurements. Here, port 1 inputs a signal into the device, and port 2 reads out the transmission response. Similarly, S11 uses port 1 to measure the reflection signal. These S-parameters, are a part of a scattering matrix, referred to as the S-matrix [77]. However, to measure a qubit, we need to make use of three ports. This type of measurement is called two-tone spectroscopy, and can be ideally carried out in the dispersive regime (which was discussed in Sec. 2.2), and practically in a regime where the qubit and the cavity are closer to each other. In the two-tone spectroscopy, port 1 of the VNA continuously outputs a signal at the cavity frequency (we call this the monitor frequency), port 3 sweeps all frequencies in a range set by the user (we refer to this as the drive frequency), and port 2 reads out the response of the cavity. Once the drive frequency becomes resonant with the cavity frequency, the cavity shifts by χ, and the signal at the monitor frequency drops as the cavity is no longer at the monitor frequency. This creates a dip in the signal at the qubit frequency. Fig. 4.13 illustrates the mechanism of two-tone spectroscopy, where a Lorentzian signal illustrates the cavity peak in two different positions: when the qubit is in its ground state $|g\rangle$ (shown in pink), and when the qubit is in its excited state $|e\rangle$ (shown in red).

The other type of measurement, called the pulsed measurement, can be used to observe Rabi oscillations, and to measure the relaxation time and the dephasing time of a qubit. In this method, the measurement period is chosen such that the qubit has relaxed back down to the ground state before the start of the next measurements. A rough heuristic is to operate at a
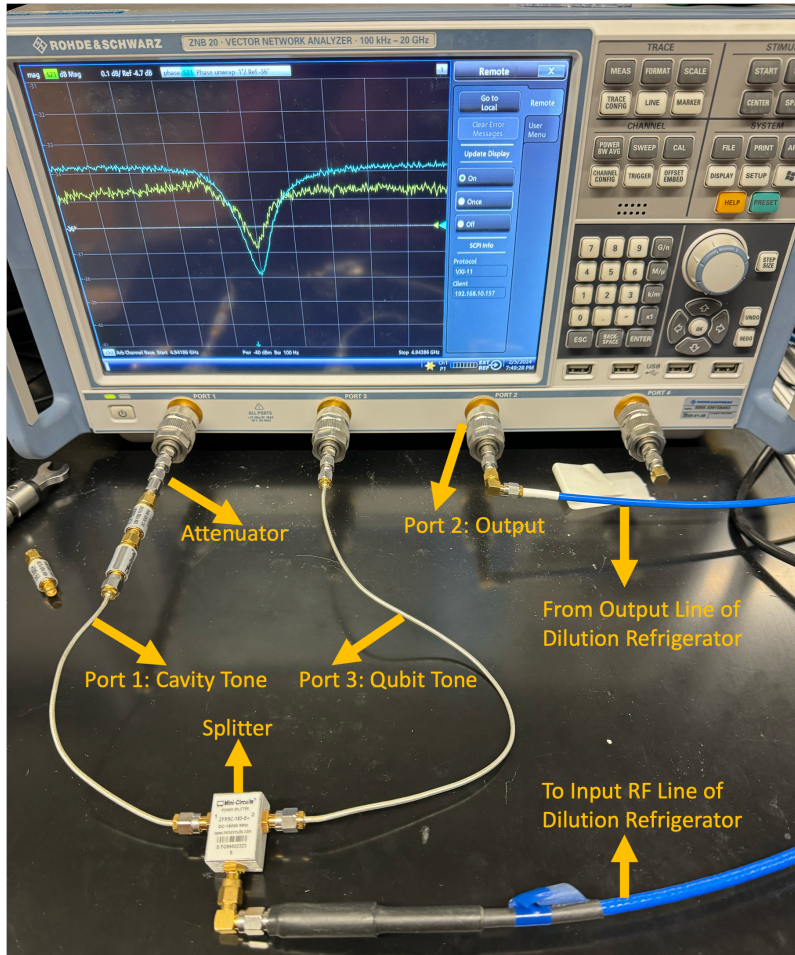
Figure 4.12: **CW Measurement Setup Using a Vector Network Analyzer** A Rhode and Schwarz VNA is used for performing CW measurements here. Port 1 controls the cavity and port 3 controls the qubit. They are connected using a signal splitter (Mini-Circuits ZFRSC-183-S+). The resulting signal is directed into the dilution refrigerator and into the input port of the device. The output signal coming out of the device and the output port of the dilution refrigerator is directed into port 2. The splitter has 10 dB of attenuation, and we place an additional 20 dB of attenuation on the cavity port.

repetition rate corresponding to $10 \times T_1$, such that the probability of the qubit being in its excited state is exponentially small. This is known as "passive reset" of the qubit. Then, one can apply a different sequence of pulses to perform operations on the qubit. For instance, to measure T_1, after waiting for the qubit to be initiated in its ground state we apply a π-pulse around the x-axis to fully excite the qubit. Then, we wait a time τ before measuring the state of the qubit. by varying τ, we observe that the measured signal amplitude drops in an exponential manner. We then can
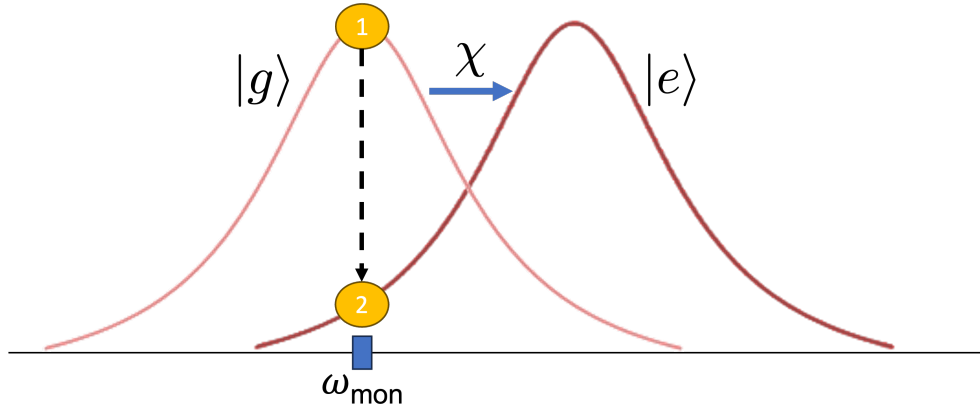
Figure 4.13: **Two-Tone Spectroscopy** When the qubit is in its ground state, the cavity is at some frequency $\omega_{r,g}$. The transmission for this position is shown by a pink Lorentzian. We pick the center frequency and constantly monitor it, and we call this frequency ω_{mon}. We have chosen $\omega_{mon} = \omega_{r,g}$. When the qubit is in its ground state, we have a peak at this frequency, and the transmission value we read out is shown by the yellow circle labeled 1. Then, we will use a different tone and drive the qubit. As soon as the frequency of the drive tone becomes resonant with that of the qubit, the qubit goes into its excited state. The cavity will then shift by the dispersive shift, χ, and will move to the location shown by the dark red Lorentzian on the right. The monitor frequency is now outputting a much smaller value, shown by the yellow circle labeled 2. At this point, the transmission value dips, and allows us to find the qubit frequency.

fit an exponential to the data, and extract the T_1 of the device.

To find the dephasing time (T_2), we perform a Ramsey experiment. We first apply a $\pi/2$ pulse to a qubit in its ground state and take it to the equator. The qubit will then precess in the x-y plane. After a time τ, we apply another $\pi/2$ pulse and immediately perform a measurement, which projects the state into one of z basis eigenstates. From the distribution of measurement outcomes we can infer the dephasing time. We readout the state of the qubit through the cavity. When detuned from the qubit frequency, the T_2 measurement yields oscillations, and looks like a damped cos wave. Fig. 4.14 shows the measurement protocols for T_1 and T_2 measurements.

Now that we understand how pulsed measurements can be used to characterize devices, we can discuss the chain of instruments required for such measurements. The main element for these measurements is an IQ mixer, with four ports, one for each of the following: RF, local oscillator
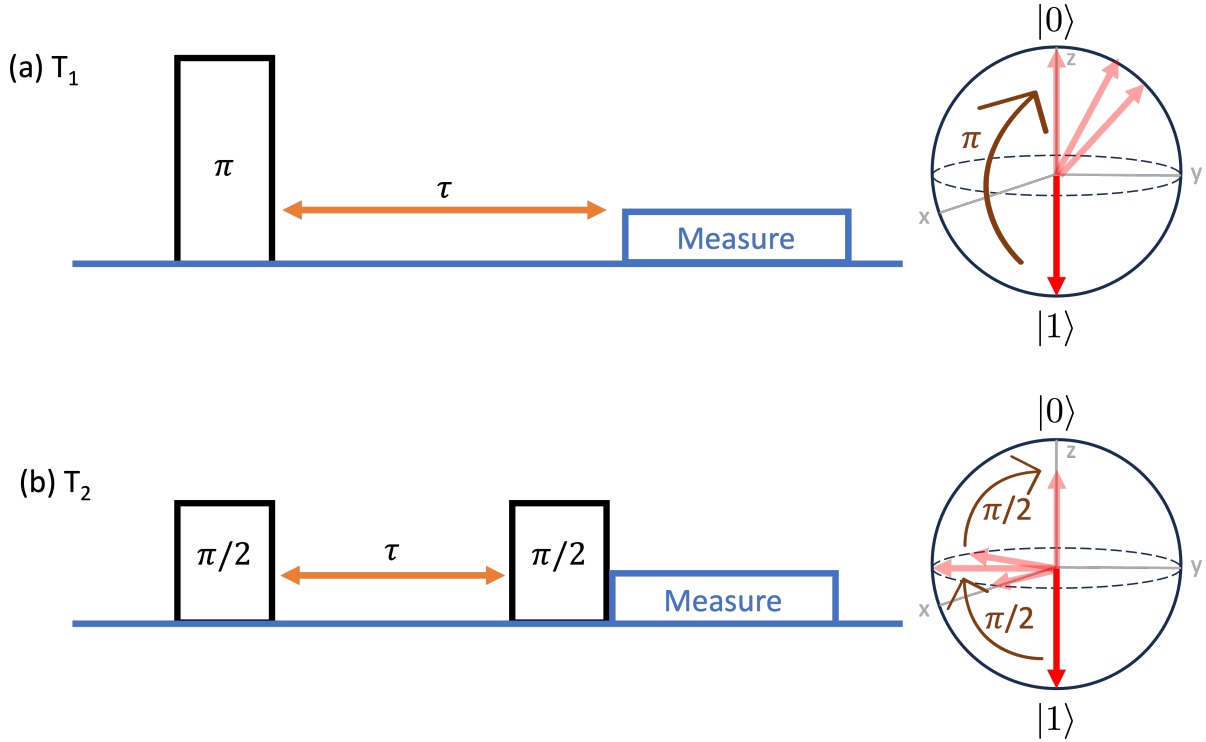
Figure 4.14: T_1 **and** T_2 **Pulse Sequences a-** To measure the relaxation time of a qubit we initiate it in its ground state. We then apply a π pulse to fully excite the qubit. We then wait a time τ before measuring the state of the qubit. We vary τ, and fit the resulting signal to an exponential. The fit parameter yields T_1. **b-** To measure dephasing time of a qubit, we first apply a $\pi/2$ pulse to take the qubit to the equator. We then wait a time τ before applying another $\pi/2$ pulse and measuring immediately. The result will be a damped cosine, and the fit parameter yields T_2.

(LO), in-phase (I), and quadrature (Q). The mixer will take the RF signal (in our case this is the cavity tone that we measure), multiplies it with a sinusoidal signal generated by the LO, and outputs an I and a Q signal.

The RF and the LO signals are of the form [13]

$$s_{RF}(t) = A_{RF}(t)\cos\left(\omega_{RF}t + \varphi_{RF}(t)\right)$$

$$(4.1)$$

$$s_{LO}(t) = A_{LO}(t)\cos\left(\omega_{LO}t\right)$$

where $A(t)$ is the amplitude and $\varphi(t)$ is the phase of the signal. The mixer takes the LO and RF signals, splits them equally into two $s_{RF}(t)/2$, and respectively multiplies them for I and Q
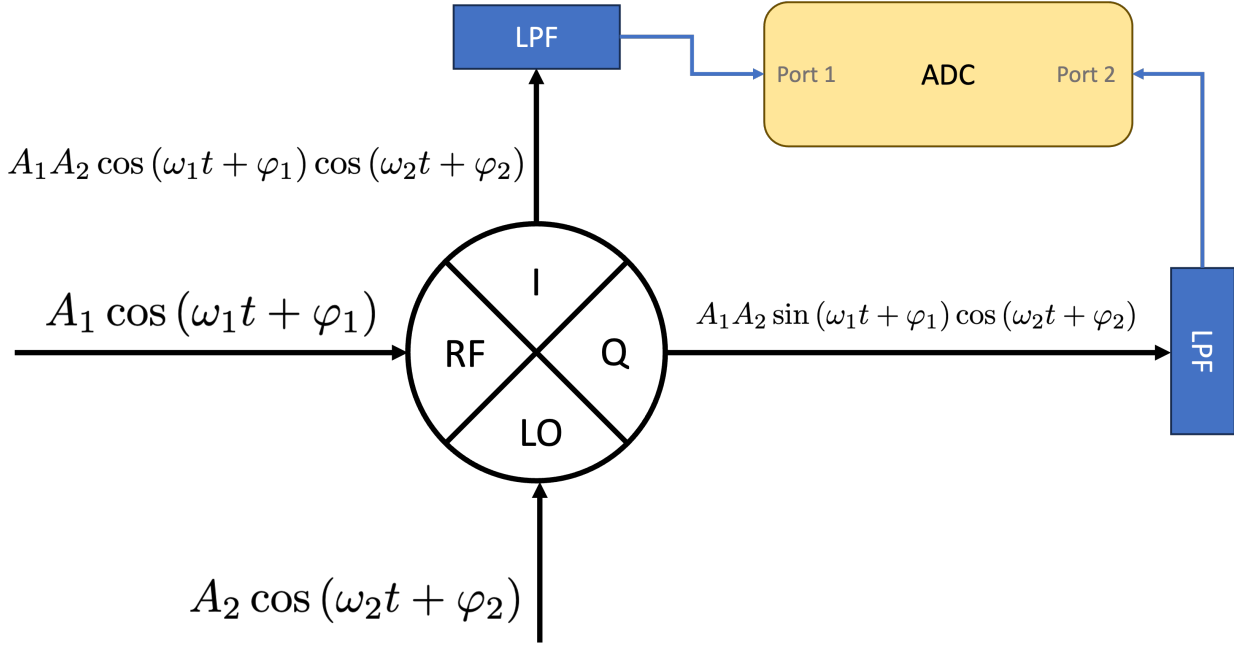
Homodyne: $I : A_1 A_2 \cos(\varphi_1 - \varphi_2), Q : A_1 A_2 \sin(\varphi_1 - \varphi_2)$
Heterodyne: $I : A_1 A_2 \cos(\Delta \omega t + \Delta \varphi), Q : A_1 A_2 \sin(\Delta \omega t + \Delta \varphi)$

Figure 4.15: **IQ Mixer** To measure a signal using an IQ mixer, we send in the output signal through the RF port of the mixer, and a signal from a local oscillator through the LO port. The RF and LO signals are split into two equal signals and multiplied by $\cos(\omega_{LO} t)$ and $\sin(\omega_{LO} t)$ to yield I and Q. The I and Q quadrature are then fed through low pass filters and into a digitizer card for readout. The IQ mixer used in our experiments is by Marki Microwave, model number IQ-4509LXP, and the digitizer card is by Acqiris, model number SA220P-1013. The low-pass filters are by Mini-Circuits, model number BLP-10.7+, and they are connected to a room temperature preamplifier by Stanford Research Systems, model number SR445A (not shown in this figure).

branches by

$$
\begin{aligned}
y_I(t) &= \frac{A_{LO}}{2} \cos(\omega_{LO} t) \\
y_Q(t) &= -\frac{A_{LO}}{2} \sin(\omega_{LO} t).
\end{aligned}
\tag{4.2}
$$

The resulting signals will then contain a sum and a difference frequency, referred to as the intermediate frequency (IF), where $\omega_{IF} = \omega_{RF} \pm \omega_{LO}$. We will then apply a low pass filter (LPF) and only keep the "difference" signal.

We can choose to set the LO frequency equal to the RF frequency and downconvert the IF signal to DC. There will also be an image frequency at $2\omega_{RF} = 2\omega_{LO}$, which can be filtered out. This type of measurement is called homodyne [78]. The resulting homodyne I and Q terms after filtering (averaging over some time T) will look like

$$
\begin{aligned}
I &= \frac{1}{T}\int_0^T \frac{s_{RF}(t)}{2}y_I(t)dt = \frac{A_{RF}A_{LO}}{8}\cos\varphi_{RF} \\
Q &= \frac{1}{T}\int_0^T \frac{s_{RF}(t)}{2}y_Q(t)dt = \frac{A_{RF}A_{LO}}{8}\sin\varphi_{RF}.
\end{aligned}
\tag{4.3}
$$

We can use the I and Q found above to extract the amplitude and phase of the signal

$$
\begin{aligned}
A_{RF} &\propto \sqrt{I^2 + Q^2} \\
\varphi_{RF} &= \arctan\left(\frac{Q}{I}\right).
\end{aligned}
\tag{4.4}
$$

While resulting in reduced complexity of the setup, homodyne demodulation can be difficult to achieve, as one needs precision for matching ω_{LO} and ω_{RF}. Additionally, it yields a lower SNR due to its susceptibility to $1/f$ electronic noise.

However, if we choose to offset the LO frequency from that of the RF signal, we can downconvert to a non-zero value. This demodulation technique, referred to as heterodyne [78], offers a better SNR. Following a similar calculation to that of the homodyne signal, we find the heterodyne I and Q signals

$$
\begin{aligned}
I &= \frac{1}{T}\int_0^T \frac{s_{RF}(t)}{2}y_I(t)dt = \frac{A_{RF}A_{LO}}{8}\cos\left(\omega_{IF}t + \varphi_{RF}\right) \\
Q &= \frac{1}{T}\int_0^T \frac{s_{RF}(t)}{2}y_Q(t)dt = \frac{A_{RF}A_{LO}}{8}\sin\left(\omega_{IF}t + \varphi_{RF}\right).
\end{aligned}
\tag{4.5}
$$

In both cases we are leaving out offset phases from the LO, as we are only interested in the change that the qubit state instills in A_{RF} and φ_{RF}. After finding I and Q components, we will use a digitizer card (ADC) to digitize the signal.

4.4   Amplifier and Filter Chains

During the first few cool-downs of the lattice device discussed in Ch. 5, we were using a low-frequency HEMT on the output line. The operation frequency of this HEMT ranges from $4 - 8$ GHz. Considering that the frequency of the full wave modes of the lattice device is near 10 GHz, we switched to a high-frequency HEMT that has an operation frequency between 4 GHz and 16 GHz. The first HEMT was not allowing us to see the higher frequency modes in full. The original HEMTs are by Amplitech, model number APT5-04000800-0710-D6, and the high-frequency HEMT is from Low Noise Factory, model number LNF-LNC-4-16-C. The high-frequency HEMT is controlled by a power supply from the same company, with model number LNF-PS3b.

Additionally, we use room temperature amplifiers on the output lines. For the lattice device discussed in Ch. 5, we use two such amplifiers. The first one is an Amplitech APT5-04000800-0710-D6, and the other one is a Mini-Circuits ZX60-183A-S+. The Amplitech operates in the $4 - 8$ GHz regime and has a 50 dB gain. The Mini-Circuits operates in the $6 - 18$ GHz regime, and has a 28 dB gain. Both input and output lines have DC blocks on them as well.

We use two different sets of filters on the output lines. The first set, which we use for lower frequencies, contains a Mini-Circuits VHF-3800+ and a Mini-Circuits VLF-5500+. The first filter is a high-pass with a $4.25 - 10$ GHz passband, and the second one is a low-pass with

a DC-5.5 GHz passband. For higher frequencies, we use a Mini-Circuits VHF-8400+ high pass filter, which has a $9 - 13$ GHz passband, as well as a K&L Microwave 6L250-00089, which is a low-pass with its 3 dB cutoff frequency at 12 GHz.

These are in addition to the filters that we use inside of the dilution refrigerator. We use the K&L Microwave filters mentioned above for input and output lines, and we attach them to the Aluminim can around the device.

We use different filters on flux bias lines. These include a Mini-Circuits low-pass filter, SLP-1.9+, which has a DC-1.9 MHz passband, and a Mini-Circuits VLFX-80+ low-pass, with a passband of DC-80 MHz. The flux bias line filters are also attached to the aluminum can inside of the dilution refrigerator.

At room temperature, the flux lines have a different set of filters. For the quasi one-dimensional lattice device these are usually the Mini-Circuits BLP-1.9+, BLP-150+, and Thor-Labs EF110. They are all low-pass filters, with passbands of DC-1.9 MHz, DC-140 MHz, and DC-1 KHz. Keep in mind that one can switch out these filters with other ones that filter out high frequency noise. However, the flux quantum of the qubit will change if the filters are changed.

After switching to the high-frequency HEMT on the output line of the lattice device, we observed a rippling quality in the transmission data. The data was suddenly more noisy than before, and the noise had a periodic quality. Examples of such data sets can be seen in Fig. 4.16. The two data sets show the presence of the issue in two different frequency ranges. The data in the panel on the right is a single-shot measurement, aimed at providing a better sense of the type of noise. For now, we will not worry about what this data represents, but will focus on the presence of this unusual noise. Similar data sets are explained in Ch. 5.

Initially, we hypothesized that the room temperature amplifiers were not suitable for some

of our measurements, as we were measuring outside of their frequency ranges. We tried switching to a new set of amplifiers, but the periodicity in noise was not eliminated. We will discuss what caused this in the next section.
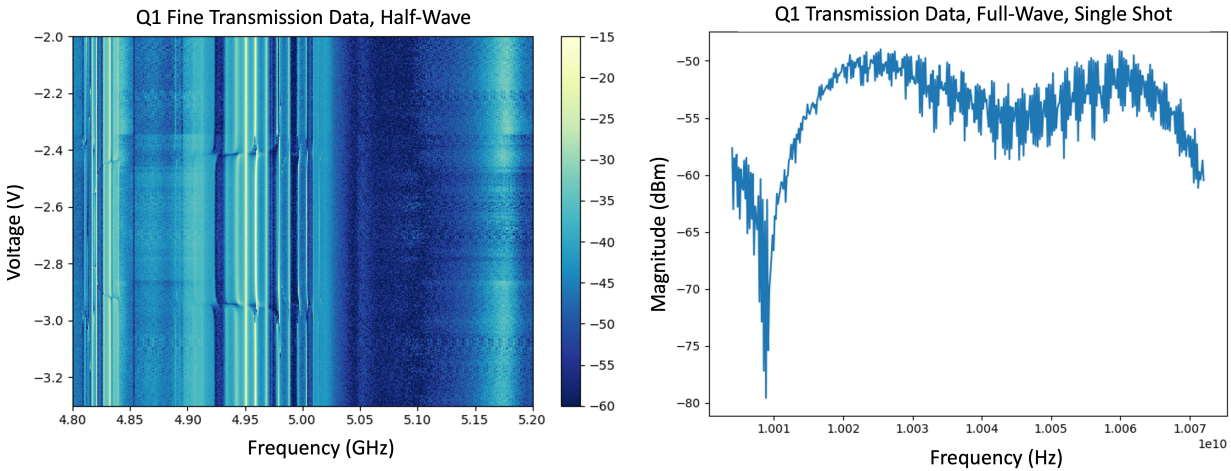

Figure 4.16: **Rippling Noise in Transmission Data** We observed ripples in the S21 data. In a single-shot measurement, these look like periodic noise added to the data. After thoroughly investigating the matter, we concluded that the cause was a loose connection inside the dilution refrigerator on the output of the device.

4.5   Challenges

After carefully searching for the culprit causing periodic noise in the data, we concluded that there was a loose connection inside of the BF refrigerator. The loose connection was between the coaxial cable on output line and the room temperature flange at the top of the BF refrigerator. This was causing ripples in the data as the pulse tube of the refrigerator caused small vibrations near the top plate. One test to confirm this consisted of repeatedly tapping on the frame of the dilution refrigerator using a screwdriver, and observing strong periodic noise appearing in the transmission data in real time while monitoring the VNA.

We temporarily remedied the issue by placing lead shot bags near the room temperature

flange and the pulse tube, securing them in place using zip-ties, and damping the vibrations. We resolved the issue by tightening all connections inside the BF refrigerator once the dilution refrigerator was warmed up. We confirmed that the ripples were eliminated in the next cool down by carefully examining different frequency ranges in transmission scans.
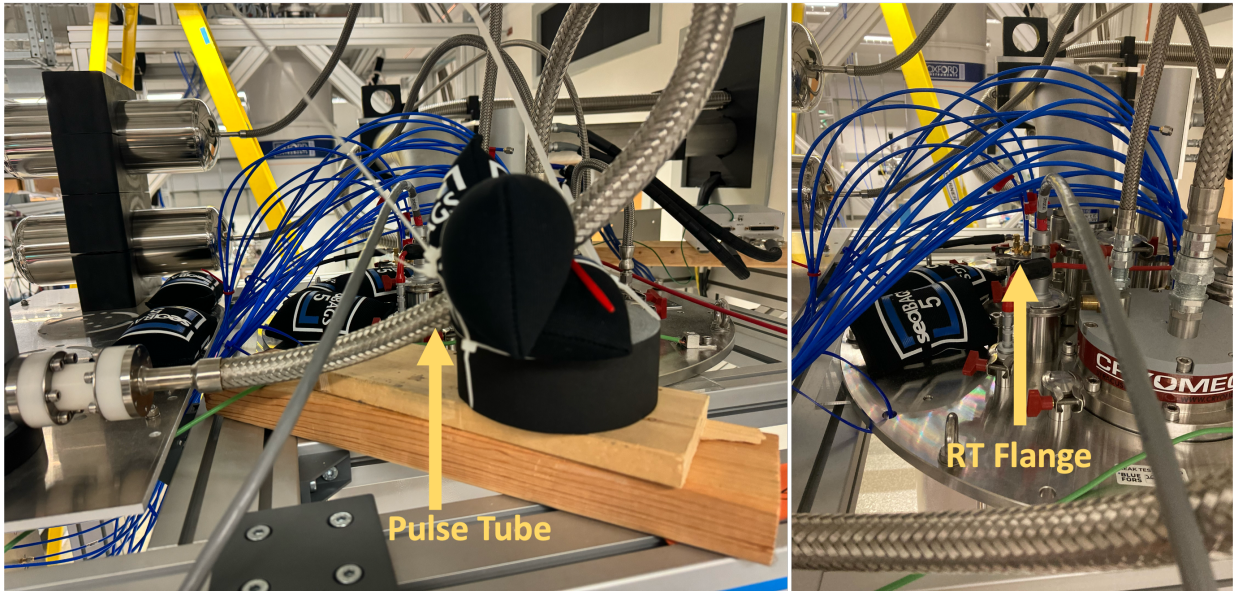

Figure 4.17: **Lead Shot Bags Used for Securing a Loose Connection** A loose connection on one of the output ports of the dilution refrigerator was causing the appearance of ripples in data. As we needed to take more measurements from the device without warming up the dilution refrigerator, we secured the pulse tube, which causes vibrations, and the flange connecting to the loose connection using lead shot bags.

Another challenge that emerged was temperature crosstalk between devices that were in the dilution refrigerator at the same time. We noticed this crosstalk between the lattice device and another device containing qubits. We observed a change in qubit frequency of the second device as the qubits of the lattice device were flux biased. The voltage put in the flux bias line heats up the base plate of the dilution refrigerator, and that change in temperature causes the frequency of the qubit on the other device to drift. Fig. 4.18 shows the frequency of the qubit on the second device as a function of time. The base plate temperature, which was scaled to match

the frequency range of the qubit is plotted in orange. While this data was being taken, the lattice device qubits were flux biased. The frequency of this qubit changes across a ~ 130 MHz span, which prevents one from taking reliable measurements. If devices are being flux biased, it is best to take data on one device at a time. It is additionally advised to wait at least 30 minutes between measuring separate devices in order to allow the temperature of the base plate of the dilution refrigerator to stabilize.
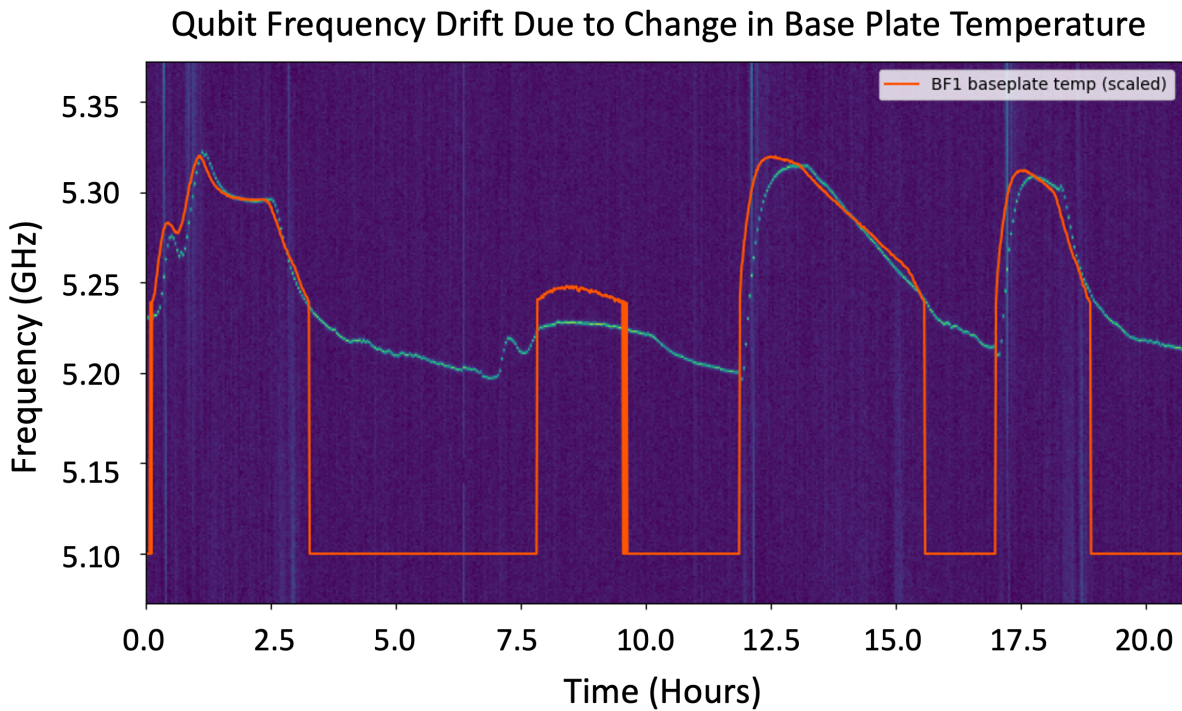

Figure 4.18: **Temperature Cross-Talk Between Devices in BF** The frequency of a qubit (called Q_T) in the BF dilution refrigerator was measured over the course of 21 hours at zero flux bias, and is shown using a teal line. A qubit on a different device (called Q_L) was flux biased during this time range in the same dilution refrigerator. As Q_L was flux biased, the frequency of Q_T drifted by a maximum of more than 120 MHz. The base plate temperature of the dilution refrigerator was scaled to be comparable with the qubit frequency. Higher flux bias voltage increased the base plate temperature more, and resulted in a comparable shift in the frequency of Q_T. There are regions (e.g. between $10 - 12.5$ hours) where we notice that the base plate temperature is perfectly flat and a constant line. This is due to temperature sensors in the dilution refrigerator not being able to read values below 7.5 mK. The reading in these situations is "T Under". We have chosen to assign a value of 5.10 GHz to all such readings in this plot. Note that the vertical edges in temperature are artifacts of crossing the threshold for the minimum readable temperature, and are not representative of real temperature data.

Chapter 5: Lattice Device

We designed and fabricated a quasi one-dimensional lattice device to study photon-mediated qubit-qubit interactions and cross-Kerr interactions between photons. This device is a prototype, enabling us to understand such interactions before designing more complex two-dimensional lattices in Euclidean and non-Euclidean geometries. In Fig. 5.1-a we see a zoomed-out image of the device, and Fig. 5.1-c shows the effective lattice laid onto part of the design. The design of this device will be explored in detail in Sec. 5.1. We will also review the theory of this lattice and its importance in Sec. 5.2. Lastly, in Sec. 5.3 we will present and discuss data from this device.

5.1 Device Design

The device has nine unit cells, each consisting of six CPW resonators. The CPW resonators are capacitively coupled. The coupling capacitors, one of which is shown in Fig. 5.2, connect three resonators and allow for photons to hop between sites (note that the resonators are the lattice sites, and not the three-way couplers).
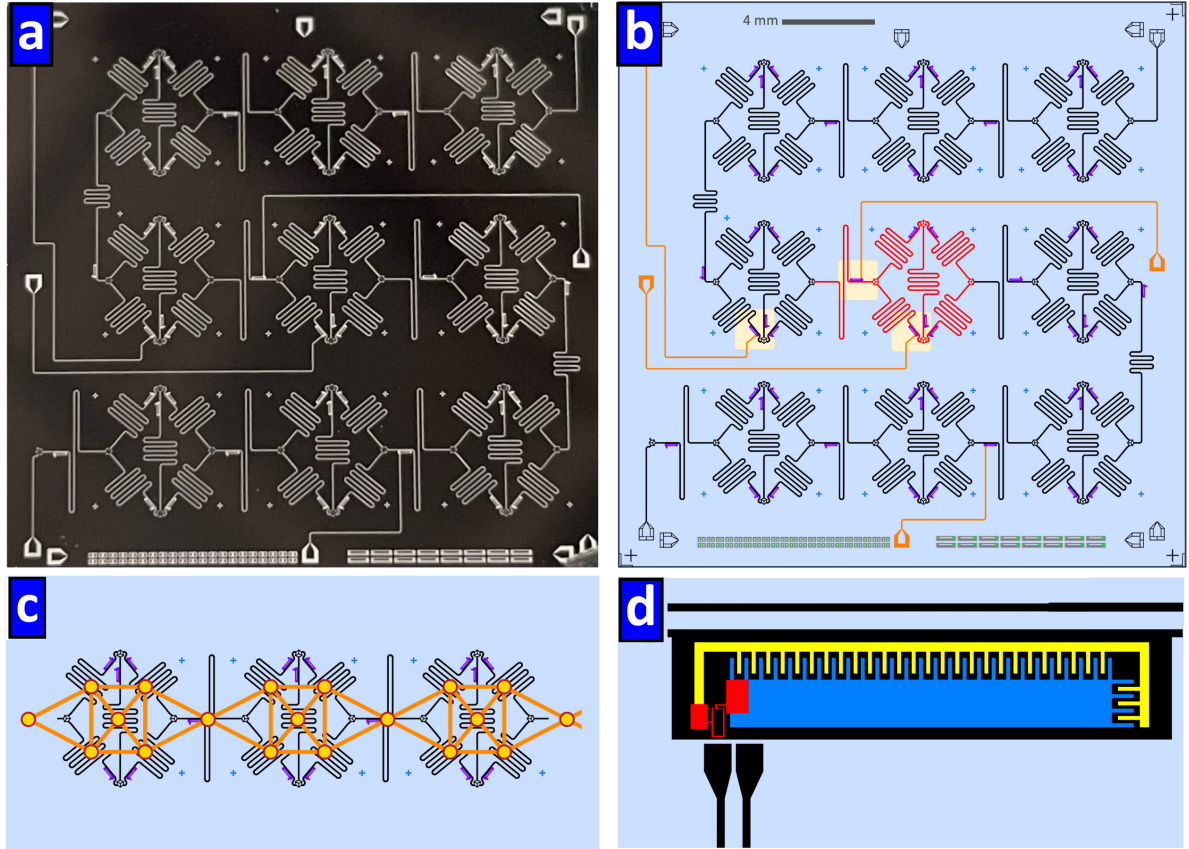
Figure 5.1: **Quasi 1-D Lattice of CPW Resonators a-** An image of the device after fabricating the photo-lithography layer. **b-** CAD image of the device. A single unit cell of the lattice is shown using red CPW resonators. The small purple rectangles on the resonators are the qubit pockets. The location for the three functional qubits has been highlighted using pale yellow squares. The qubits are labeled Q3, Q2, and Q1 from left to right. The orange lines are the flux bias lines used for frequency-tuning the qubits. The blue crosses are alignment marks used for aligning the e-beam layer with the photo-lithography layer during fabrication. **c-** The effective lattice shown in orange is overlaid on the layout lattice. The resonators are the lattice sites, and their centers are shown using yellow circles. **d-** A CAD image of the qubit. As in panels **b** and **c**, the light blue region is metal, and the black regions are dielectric gaps. The darker blue and the yellow sections are the capacitor paddles of the qubit, and made of metal as well. The red region shows the SQUID loop and its contact regions with the capacitor paddles.

The CPW resonators have a centerpin width of 20 μm and gaps of 8.372 μm. Each res-

onator was designed to have a 5 GHz frequency at its first harmonic, and a 10 GHz frequency at

its second harmonic. We are interested in studying the band structure of this lattice. Large differ-

ences in the frequencies of individual resonators may cause localizations that would prevent us
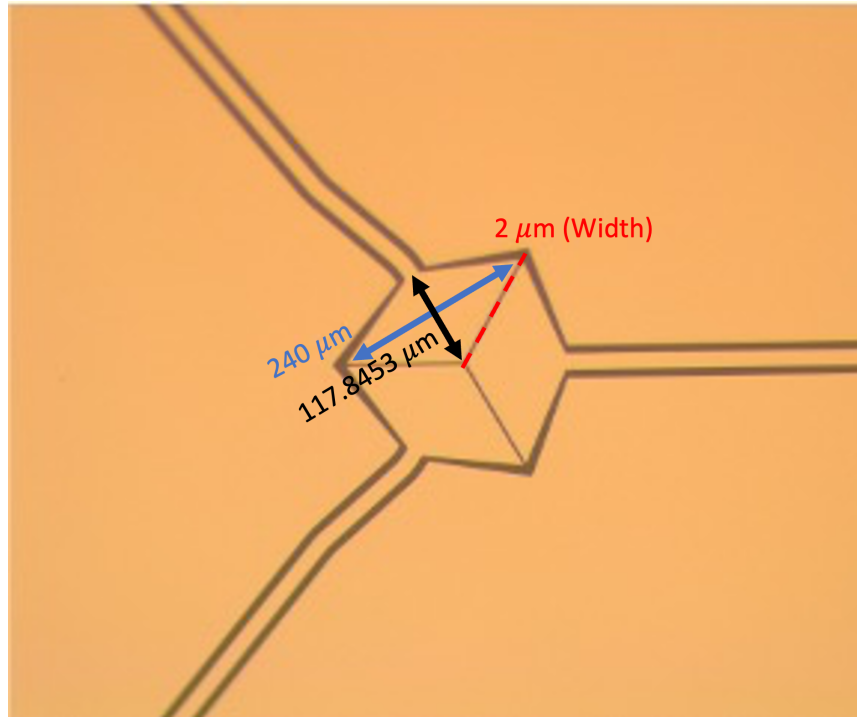
Figure 5.2: **Three-Way Capacitive Coupling** This structure capacitively couples three CPW resonators to one another, and allows for hopping between them. The coupler was designed with a 2 μm gap due to the resolution limitation of the photo-lithography system. Hence, the dimension for the blue arrow and the black arrow had to be quite large, in order to accommodate a capacitance and therefore a larger coupling. The pin-to-pin capacitance with these dimensions is ~ 19 fF according to Maxwell simulations.

from accessing the band structure physics. Thus, it is important for the disorder in frequency to

be minimized. As such, we performed disorder compensation simulations and tests, the results

of which can be found in Appendix B.

As space on the chip is limited, and the design is large, the three-way couplers had to be

made small in order to accommodate the space available. However, we desired large pin-to-pin

capacitances, as we would like to maximize hopping between sites. We utilized Ansys Maxwell

to carry out finite-element simulations to check capacitances for different designs. One constraint

that we had to keep in mind was that the gap separating the three capacitor planes could not be

smaller than 1 μm in width, as the resolution of the MLA150 is 1 μm. For the three-way coupler,

we use a 2 μm gap, width of 117.8453 μm, and length of 240 μm. We find that the pin-to-pin capacitance is ~ 19 fF between pairs of the sections. Utilizing the calculation in Ch. 3.4 and Eq. 3.40, which states $t/2\pi \approx \nu C_c/C_{res}$, and using this value for the capacitance, we find that the hopping should be ~ 47.5 MHz for a 5 GHz mode. Note that we used $C_{res} = cL = L\sqrt{\ell c}/\sqrt{\ell/c} = 1/(2\nu Z_0)$ to find the value for C_{res}. Here, $Z_0 = 50$ Ω is the standard impedance of the circuit, L is the length of the resonator, ν is the bare resonator frequency.

Due to space limitation, we generated multiple designs for this device. For instance, we experimented with different bend radii where the resonators were bent. The three radii we chose were $r = 70$ μm, $r = 90$ μm, and $r = 110$ μm. We were looking for a design that would take the least space, while maximizing the straight portion of the resonator at its end, so the qubit pockets could be placed near the ends of the resonators. This is due to qubit pockets being longer than the spacing between the meanders of the resonators. Additionally, the design had to provide enough space between the resonators so they would not run into one another.

The $r = 110$ μm design had the issue that two of the resonators were getting too close to one another. These are shown in red circles in Fig. 5.3. The other two designs both worked well with slight modifications. We chose the design with $r = 90$ μm for the final device. To fit everything, we chose a qubit distance of 510 μm from the end of the resonators. We also reduced the number of meanders in resonators on the outside of the rhombuses from 8 to 6, and we made the rhombuses slightly longer vertically. Leaving the rhombuses with equilateral sides creates issues such as the resonators running into one another, and wastes a lot of vertical space between unit cells. Fig. 5.4 shows an early version of the design, before making adjustments.
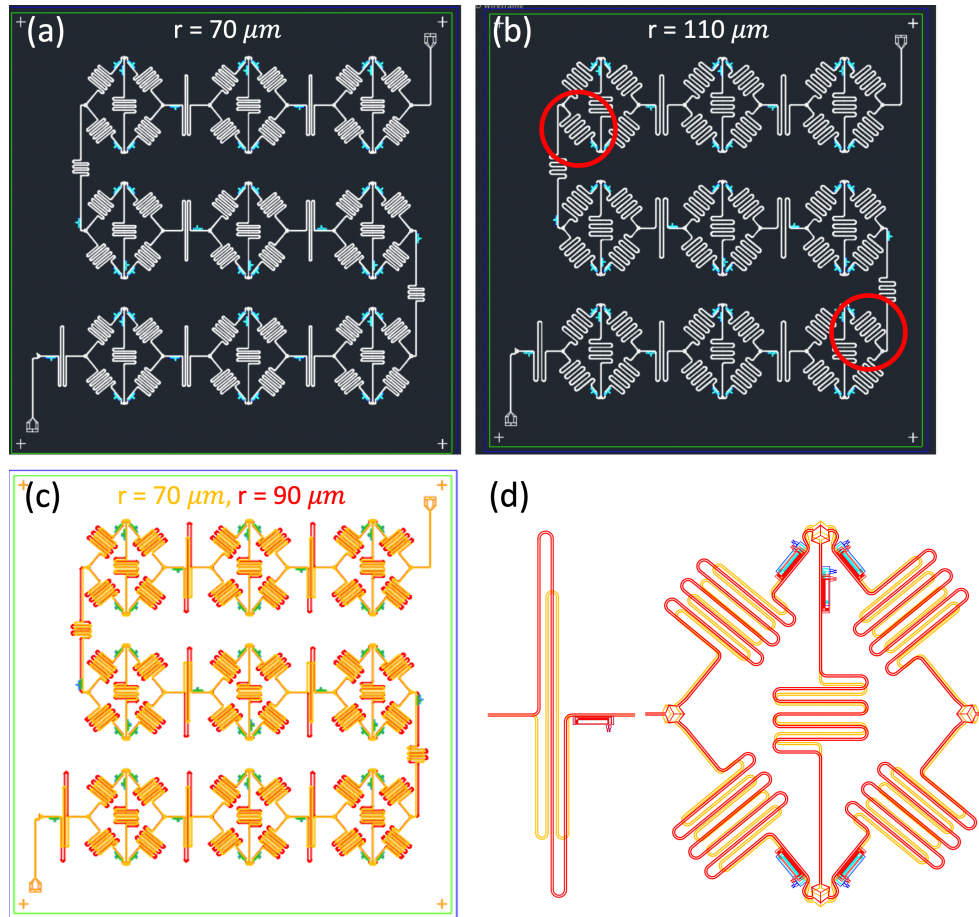
Figure 5.3: **Lattice Device Design Variations a and b-** These panels show the design with 70 μm and 100 μm resonator bend radii respectively. The 110 μm design has the problem that the resonator on the edges of the chip (shown in red circles) get too close to one another. This would make fabrication difficult, and wire-bonding in that region would be impossible. **c-** Comparison between the 70 μm and 90 μm designs, shown in yellow and red respectively. Both designs are reasonable. The 90 μm design makes good use of the vertical space available on the chip, and is the chosen radius for the main device. It also provides slightly more space between the initial bends of the CPW resonators and the coupling capacitors near them. **d-** Zoomed-in figures of different parts of the unit cell from panel **c**.

Additionally, we have placed four qubits on the device by writing SQUID loops at the intended sites. However, once we cooled down the device in the BF dilution fridge, it emerged that one of the qubits was not functioning, and only three of the qubits were measurable. These qubits are highlighted in yellow boxes in Fig. 5.1-b. While we planned on making only four qubits, we have placed a qubit pocket at every lattice site to ensure minimal variations in resonator
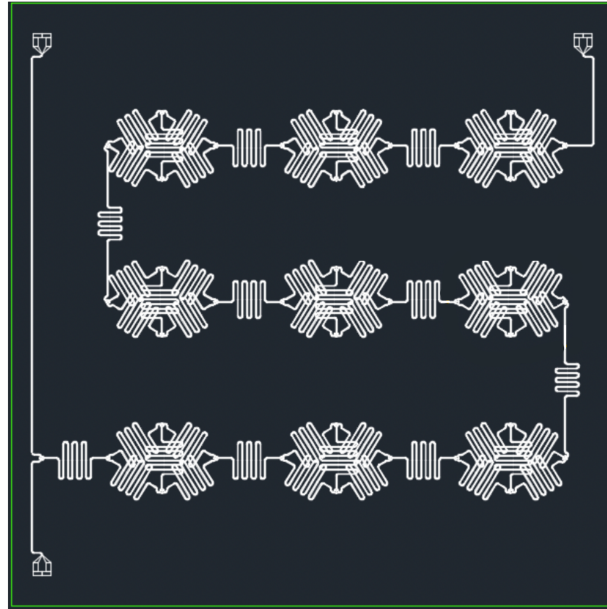
Figure 5.4: **Lattice Design before Modifying Unit Cell Dimensions** Device design before modifications. In this version, the rhombuses are not tall enough, so the resonators run into each other. Vertical space was not being utilized well.

frequencies. Since these pockets couple capacitively to the CPW resonators, these capacitances may affect the frequency of the resonators. Hence, placing them everywhere ensured eliminating large variations in frequency that would arise from the existence of these pockets. Fig. 5.1-d shows the two qubit paddles in yellow and dark blue, and the SQUID loop in red.

Two of the qubit locations that we chose were on horizontal resonators, while the other two were on the edges of rhombuses. The two that were at an angle posed a fabrication challenge at the e-beam lithography stage, as one can perform only a single angled evaporation per chip. Therefore, it was essential to come up with a design that would work for all four qubits. This resulted in an unconventional design for the qubits that are at an angle, by adding arms to force the junctions to be horizontal on the chip. Fig. 5.5 shows the design for both types of qubit. The areas in which the junctions form are shown using white arrows.

The qubit pockets were designed to have digitated teeth to maximize capacitance, and
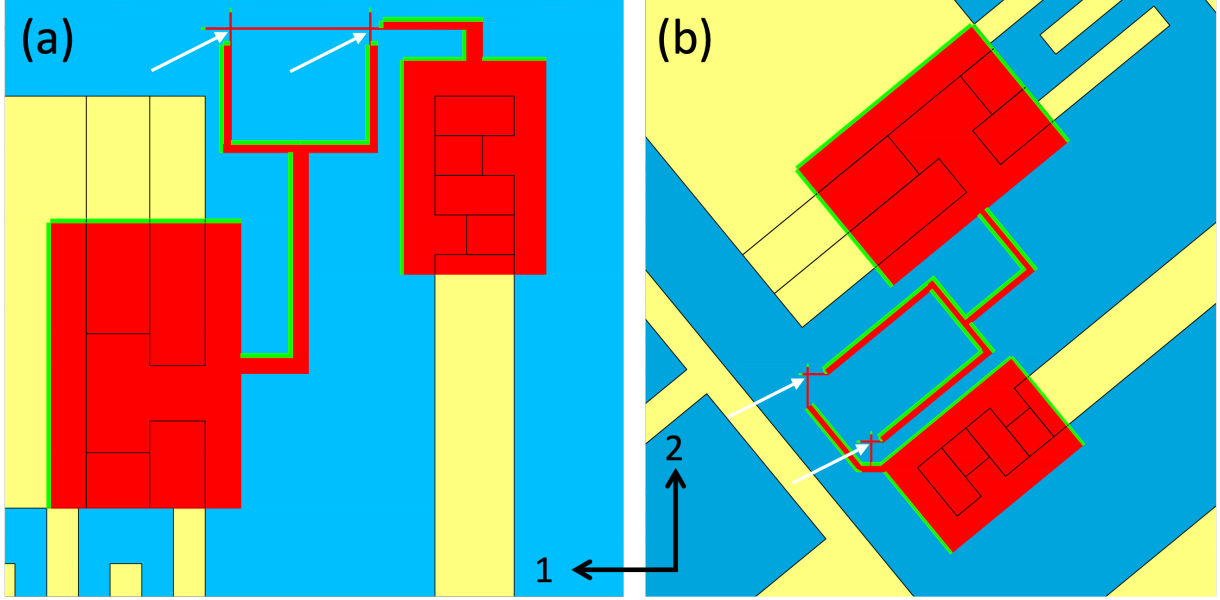
76

Figure 5.5: **Josephson Junctions at Unconventional Angles a-** The qubit pocket in this panel is parallel to the edges of the chip. Therefore, the SQUID loop containing the Josephson junctions is also parallel to the edges of the chip. **b-** This qubit pocket is at an angle compared to the edges of the chip. It is essential for the direction of the junctions to match that of the junctions in panel **a**. Therefore, the design adds small arms to make junction directions uniform across the chip. The evaporation angles for both qubits are now left and up, in that order, and are shown using black arrows.

minimize E_C, so that E_J/E_C would be as large as possible for a certain qubit frequency. It is possible to achieve such large capacitances without the digitated teeth, but the dimensions of the qubit pockets would be very large for such a design. With the digitated teeth we can make the qubit pockets smaller and achieve the desired E_C.

We used Ansys Maxwell to perform the finite-element simulations that yielded the capacitance values, from which E_C was extracted. Based on simulations, the effective capacitance of the qubit pocket is $C_\Sigma = 0.1174$ pF, which yields $E_C \sim 164$ MHz. For a 4 GHz qubit, this would result in $E_J \sim 12.33$ GHz, and $E_J/E_C \sim 75$. These values would be achievable with a junction of size 200 nm. The E_J and E_C values were obtained using two different methods: Qiskit Metal simulations from IBM [79], and equations in Eq. 5.1. The difference in results between the two

methods is 1.09% for E_C and 1.87% for E_J.

$$C_\Sigma = \tilde{C} + C_{transmon}$$

$$\tilde{C} = \left(\frac{1}{C_{hc} + C_{hg}} + \frac{1}{C_{lg} + C_{lc}} \right)^{-1}$$

$$E_C = \frac{1}{2\pi\hbar} \frac{e^2}{2C_\Sigma \times 10^{-12}} \tag{5.1}$$

$$E_J = \frac{\omega_{q,target}^2}{8E_c}.$$

Here, $C_{transmon}$ is the capacitance between the two transmon paddles, which are shown in dark blue and yellow in Fig. 5.1-d. We refer to the yellow portion as the high side, and the dark blue as the low side. C_{hc}, C_{hg}, C_{lg}, and C_{lc} are the capacitances between the high side and the center-pin, high side and ground plane, low side and ground plane, and low side and center-pin respectively, as seen in Fig. 5.6. We have defined $\tilde{C}$ as the geometric sum of the high side and low side capacitances to ground plane and center-pin. e is the charge of the electron, and $\omega_{q,target}$ is the desired qubit frequency.

5.2   Theoretical Description of the Lattice

In this section we will explore the band structure of the lattice. The unit cells of the lattice dictate the type of band structure that emerges. The lattice sites, through which photons propagate, are the resonators. The top panel in Fig. 5.7 shows the layout lattice, where we lay resonators on top of the dark blue lines, and the yellow circles show where the resonators are coupled to one another. The bottom subfigure however, shows the effective photonic model, where the center of each site (resonator) is shown with a blue circle, and each site is connected to its neighbors using a light blue line.
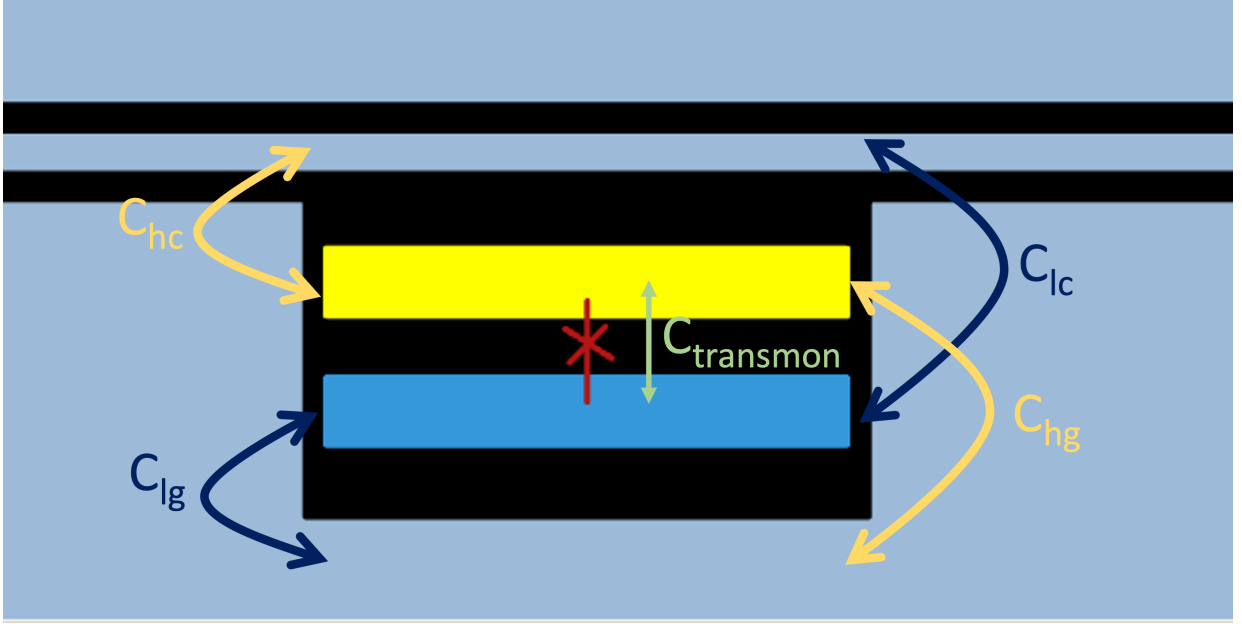
Figure 5.6: **Sketch of Transmon Capacitances** Consider a transmon qubit that is coupled to a CPW resonator. The grayish-blue region indicates the ground-plane, which we will call "g", as well as the center-pin of the CPW, which we will call "c". The black areas represent bare substrate. The yellow and the bright blue areas are the metal transmon paddles (we will call them "h" and "l", respectively.), and the red cross shows the Josephson junction. There is a capacitance between each pair of metal slabs, shown using an arrow. The total effective capacitance of this system is given by C_Σ in Eq. 5.1.

This lattice is unique as its band structure includes a gapped flat band, an ungapped flat band, a linear band, and a quadratic band near 10 GHz. The band structure for this lattice was obtained by numerically solving the tight-binding model, a simpler case of which we explored in Ch. 2.3.1. Examples of such calculations are explored in detail in Ref. [6]. The flat bands can facilitate short-range yet strong interactions between qubits, while the other bands result in long-range interactions that are weaker. In the dispersive regime, the interaction Hamiltonian between two qubits is given by [80]

$$H_{int} \approx \hbar \sigma_+^{(1)} \sigma_-^{(2)} \sum_k \frac{g_k^2}{\Delta(k)} \psi_k(x_1) \psi_k^*(x_2) + h.c. \tag{5.2}$$
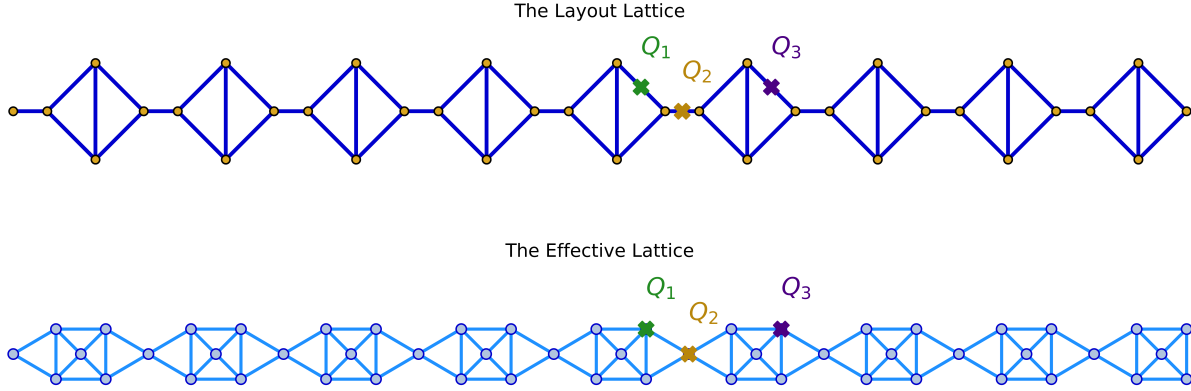
Figure 5.7: **The Lattice Layout and the Effective Lattice** The layout lattice shows the location of CPW resonators in dark blue lines, and the coupling capacitors with yellow circles. The input port of the lattice is on the left end and the output port is on its right end. The locations of qubits have been shown using crosses. Qubit locations were chosen to be in the same or adjacent unit cells to achieve stronger qubit-qubit interactions. While they are close to one another compared to the lattice constant, they are spatially tens of millimeters separated from one another, so direct interactions between them are close to non-existent. The effective photonic lattice at the bottom shows the center of CPW resonators with blue circles, and the connection of each resonator to neighboring lattice sites in light blue lines.

The lattice's band structure, depicted in Fig. 5.8, varies slightly between modes with symmetric and anti-symmetric on-site wave functions [6]. For one thing, the sign of the hopping is different in these two cases. Referring back to Ch. 3.4, we can clearly see from the voltage profile that the full-wave modes have the same sign hopping between sites, while for the half-wave modes the sign of hopping can be positive or negative for neighboring sites.

Having six sites per unit cell means that we should expect 6 normal modes or bands per each distinct value of k. However, in this lattice the flat band with energy of -2 is doubly degenerate; so while the resulting band structure has six bands, we can only see five in Fig. 5.8.
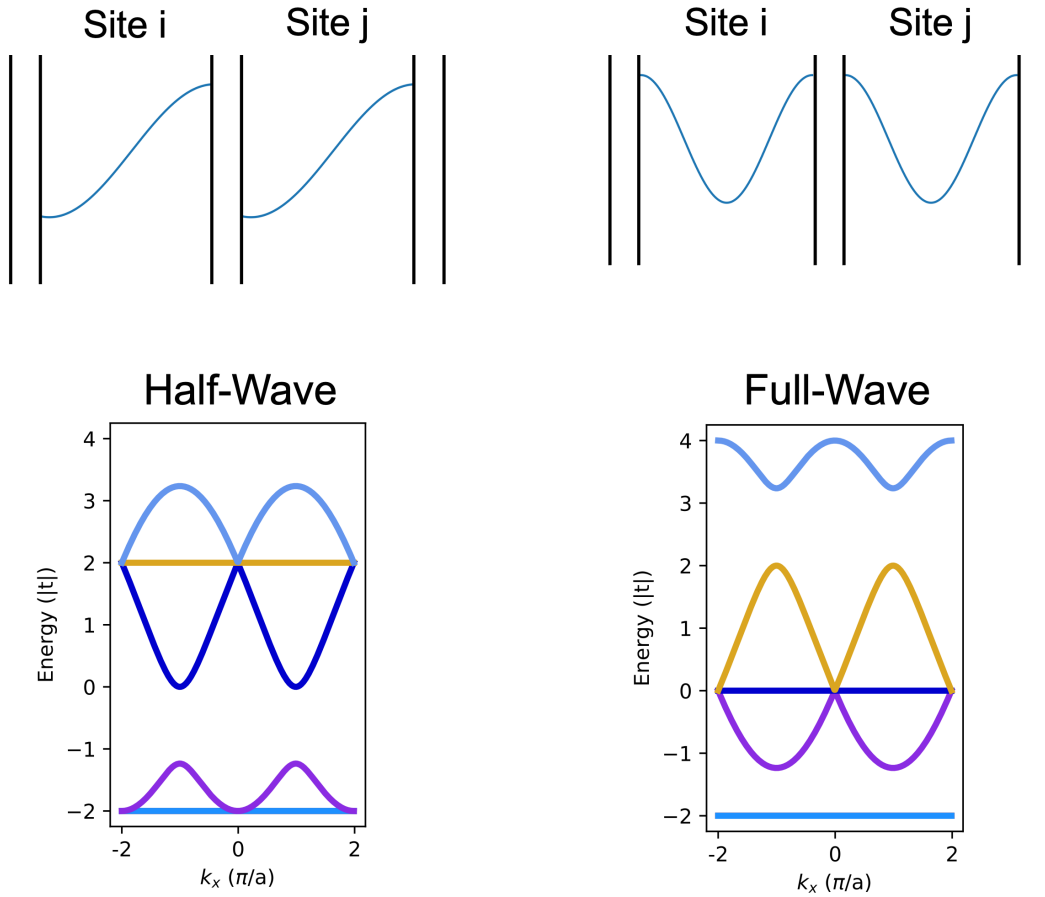
Figure 5.8: **Band Structure of Quasi One-Dimensional Lattice** The panels in the left column show the on-site wave-function for the half-wave modes at the top, and the lattice band structure at half-wave modes at the bottom. The right hand column shows the same for full-wave modes. The half-wave and full-wave modes half opposite hopping signs.

5.3 Data

Over the last year, we have collected promising data from this device. The data demonstrates that it is possible to observe photon-mediated and cross-Kerr interactions in such lattices. This opens up a vista of possibilities for designing lattices that are not constrained to one dimension or flat space.

Transmission Data vs. Flux

We are able to flux-tune the frequency of all three operational qubits, and observe the interaction of the qubits with both the half-wave and full-wave bands of lattice modes. Figs. 5.9 and 5.10 show transmission data, where the bright vertical lines are the lattice modes. We notice that some of these modes are fainter, and some transmit more power. When an eigenmode couples weakly to the input or output port of the device, it becomes difficult to observe. We also notice that the qubit appears in this data, and it looks like a sideways *cosine* function. This is because the qubit frequency changes as flux is swept, and the qubit energy depends on $\cos(\Phi)$ as seen in Ch. 3.2. When a qubit becomes resonant with a mode, the two hybridize. If the frequency of the qubit is tuned through a lattice mode, they will form an avoided crossing. The size of the avoided crossing is set by the coupling strength between the qubit and the mode. It is important to note that as the qubit becomes resonant with each mode, the system is no longer in the dispersive regime. Fig. 5.9 shows transmission data for half-wave modes in magnitude, while Fig. 5.10 shows the same for full-wave modes. The rows correspond to qubits Q2, Q3, and Q1 from top to bottom. The left hand column in both figures contains raw transmission data, and the right hand column includes the differential versions of the same data. The differential data was achieved by first tuning the qubits far away from the modes and taking a single-trace transmission scan of the modes alone. Then, in order to subtract the reference trace from the data, we divide the latter by the former, as transmission data is in logarithmic scale. Lastly, we blank out regions of data where the transmission is smaller than an empirically determined noise floor. This method eliminates features that are insensitive to the qubit and highlights ones that interact with it more strongly. Additionally, it makes looking at tall and short peaks at the same time easier. To understand
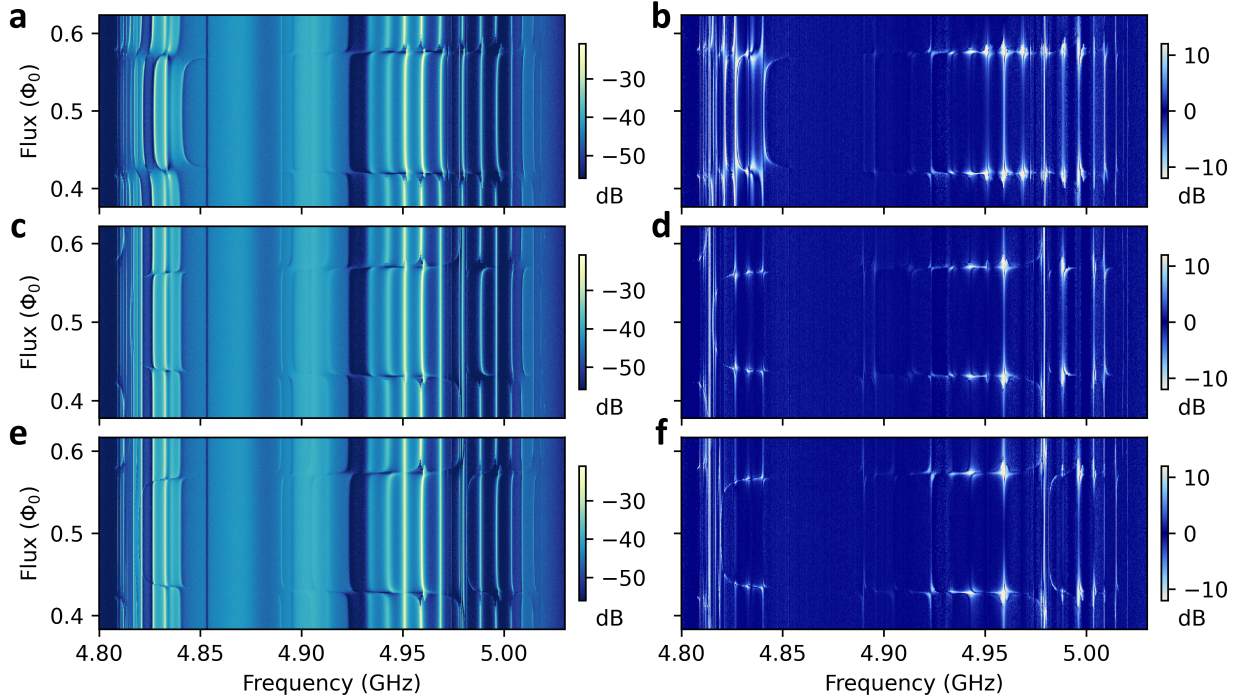
Figure 5.9: **Transmission and Differential Transmission Data at Half-Wave** S21 Transmission data at half-wave modes, with qubit interactions. The rows correspond to Q2 , Q3, and Q1 from top to bottom. The left-hand column shows the raw data, while the right-hand column shows differential data. The raw data includes extra transmission, potentially due to box modes. As these modes do not interact with qubits, they are removed in differential data. Note that we have chosen the color bars for differential datasets to be symmetric around zero. The bands of modes qualitatively match well to the simulated half-wave band structure presented in Fig. 5.8.

transmission data better, we took narrow scans in different regions of the band structure for both sets of modes. For half-wave modes we only took finer data in the region with lower energy bands, as seen in Fig. 5.11, where we used low input powers. The rows correspond to Q2, Q3, and Q1 from top to bottom. Here, we can distinguish avoided crossings between lattice modes and qubits more clearly. We also notice that the three qubits couple differently to the modes. In the right hand column, we focus on the qubit-mode crossings at a lower flux, and get a clearer view of interactions.

We present raw and differential transmission data for the lower band of the half-wave modes in Fig. 5.12. These have higher input powers compared to Fig. 5.11.
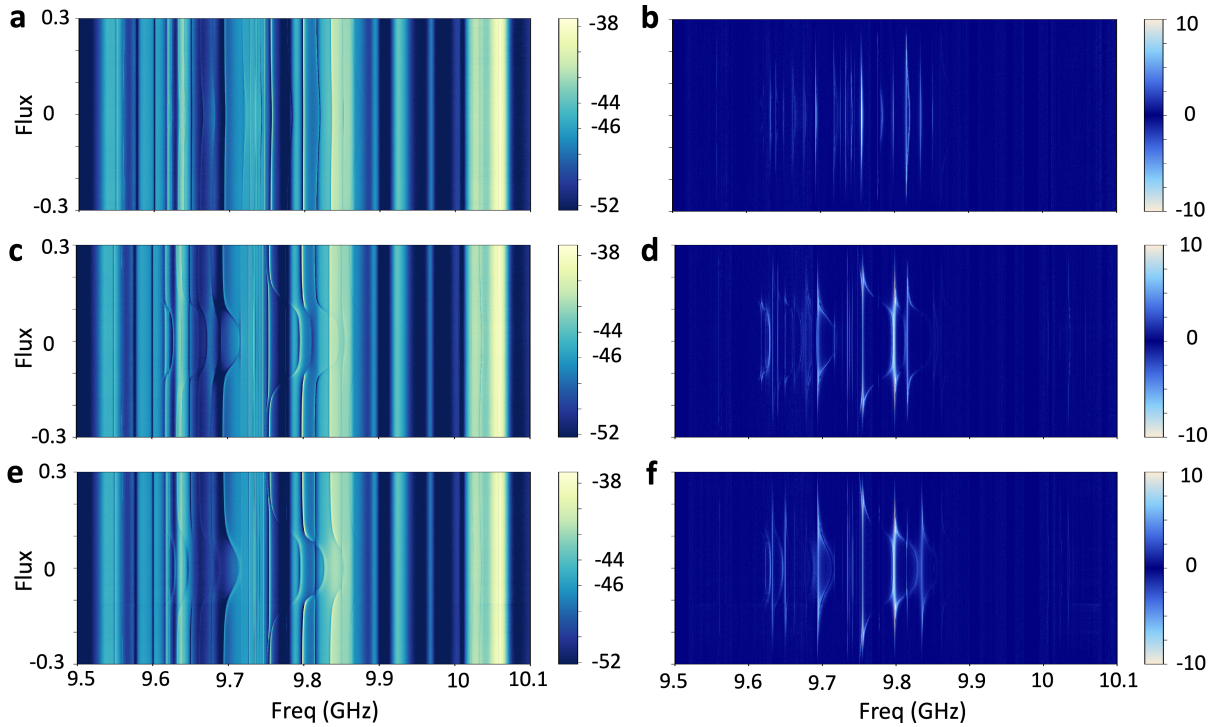
Figure 5.10: **Transmission and Differential Transmission Data at Full-Wave** S21 Transmission data for full-wave modes, with qubits interacting with the modes. The rows correspond to Q2 , Q3, and Q1 from top to bottom. The left-hand column shows the raw data, while the right-hand column shows differential data. The raw data includes leakage transmission, which has been removed in differential data. Note that we have chosen the color bars for differential datasets to be symmetric around zero. The bands of modes qualitatively match well to the simulated full-wave band structure presented in Fig. 5.8.

We collected fine transmission data at all three band regions for full-wave modes and show the results in Fig. 5.13, as it is difficult to observe interactions between the qubits and the modes in the wider transmission data in Fig. 5.10. Rows a, b, and c correspond to Q2, Q3, and Q1, respectively. This finer data especially helps with distinguishing avoided crossings between Q2 and the modes, as the interactions seem to be small compared to the full frequency range of the wider transmission scan. Additionally, we can better observe qubit-mode interactions in the lower flat band and the upper band, as some of the modes are fainter in these regions. We observe that in certain cases the data yields more information and has better visibility in phase rather than in magnitude. For example in Fig. 5.14, it is easier to see the modes in the upper band of the
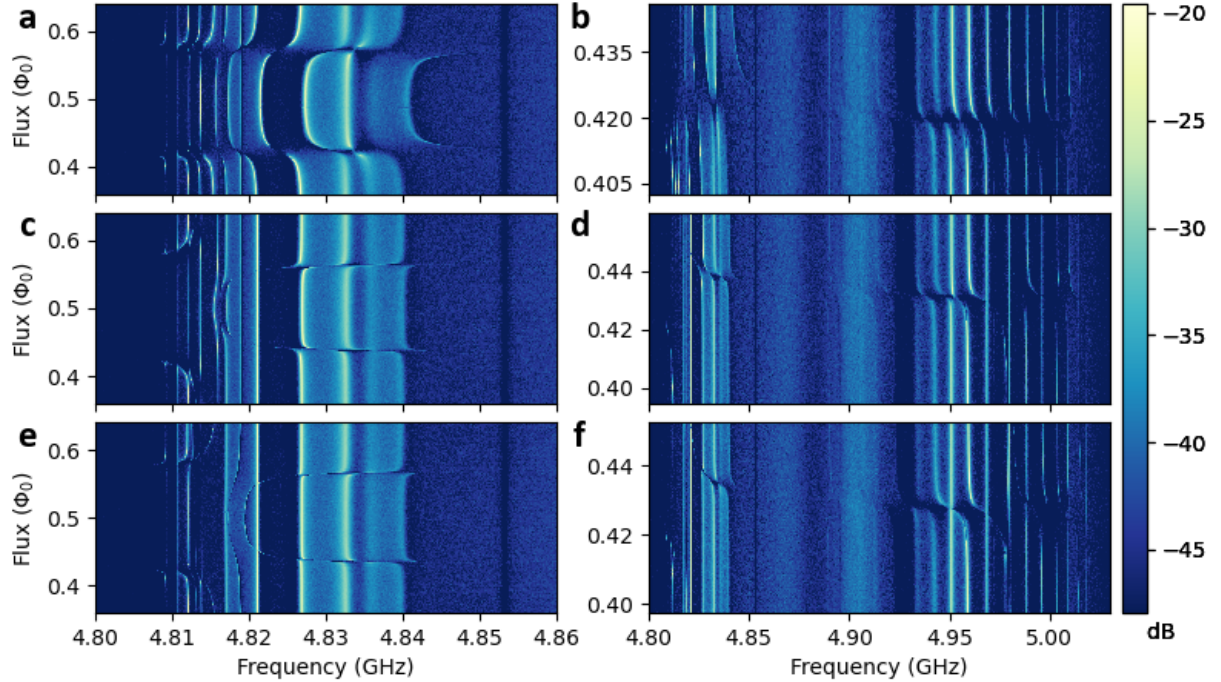
Figure 5.11: **Low Power Half-Wave Transmission** Interaction between half-wave modes and qubits in transmission data, at lower input power. **a, b-** Qubit Q2, **c, d-** Qubit Q3, and **e, f-** Qubit Q1.

full-wave transmission data in phase.

Mode-Mode Spectroscopy

For this device, we found that an unusual non-linear two-tone spectroscopy of the modes yields valuable information about interactions in this device. In this type of measurement, we monitor a cavity mode (usually a strong half-wave mode) and sweep a range of frequencies using the drive tone. Where there is a mode interacting with a qubit at full-wave frequencies, the monitored mode dips due to it shifting. We refer to this measurement as mode-mode spectroscopy. This type of data is especially useful for understanding full-wave modes better, because as we saw in the previous section, some of the modes are quite faint in transmission data, and there is a lot of leakage transmission.
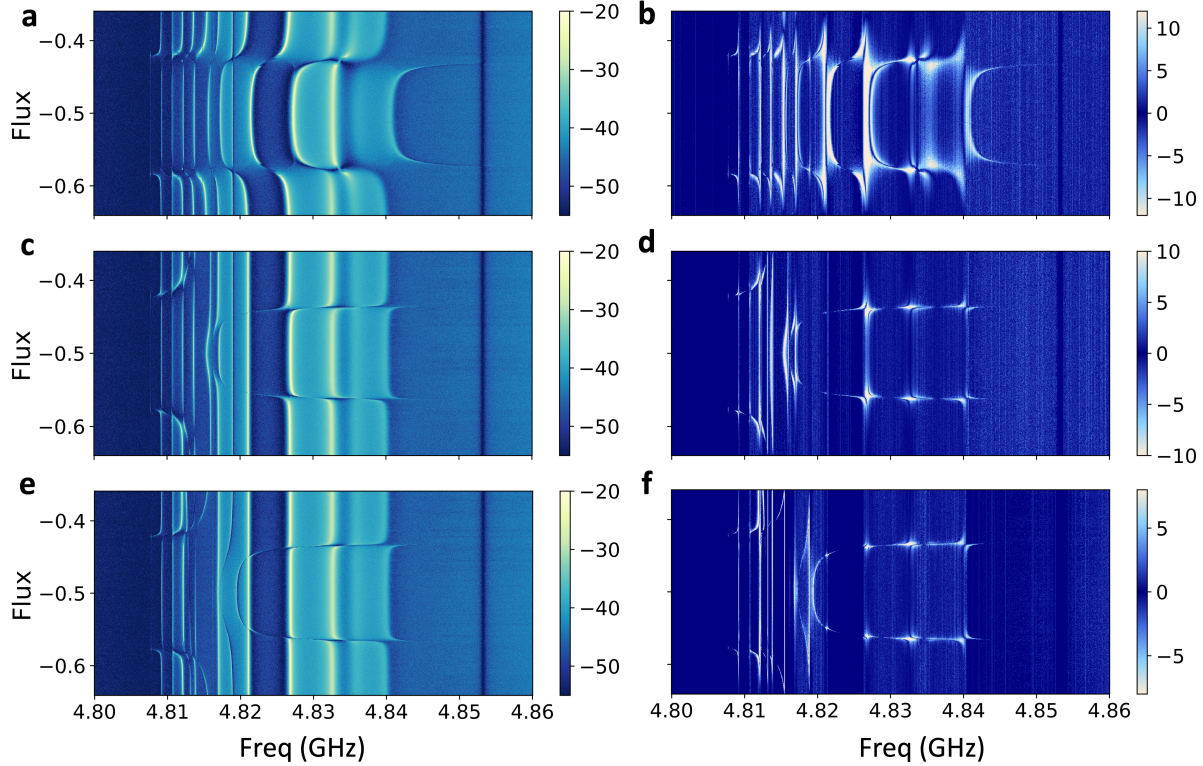
Figure 5.12: **Zoomed In Lower Band Transmission Data at Half-Wave** Fine S21 transmission scan of half-wave modes in the lower band. The left column shows the raw data, while the right column shows differential data. We choose the color bar for the differential data to be symmetric around zero. **a, b** are from qubit Q2 being flux tuned, **c, d** are from Q3, and **e, f** are from Q1. By taking this finer data and zooming in on the modes we can see more clearly the difference in how each qubit couples to the modes, and how the interaction strengths vary between each qubit and a certain mode. For instance, Q1 couples much more weakly to the mode that is slightly above 4.825 GHz compared to Q2 and Q3, as it forms a smaller avoided crossing with the mode.

For the mode-mode spectroscopy data presented in Fig. 5.16-c and Fig. 5.16-d, we have tuned all qubits frequencies to be around 7 GHz, and far away from both full-wave and half-wave modes. In this figure, we are comparing transmission data (with qubit Q3 interacting with modes) with mode-mode data. This method eliminates box modes. In mode-mode spectroscopy we see that some modes only appear at higher powers, while others get power broadened at the same power. However, we can still determine the location of modes accurately from this data. Comparing this data to the simulated fractional DOS presented in Fig. 5.15, we observe good
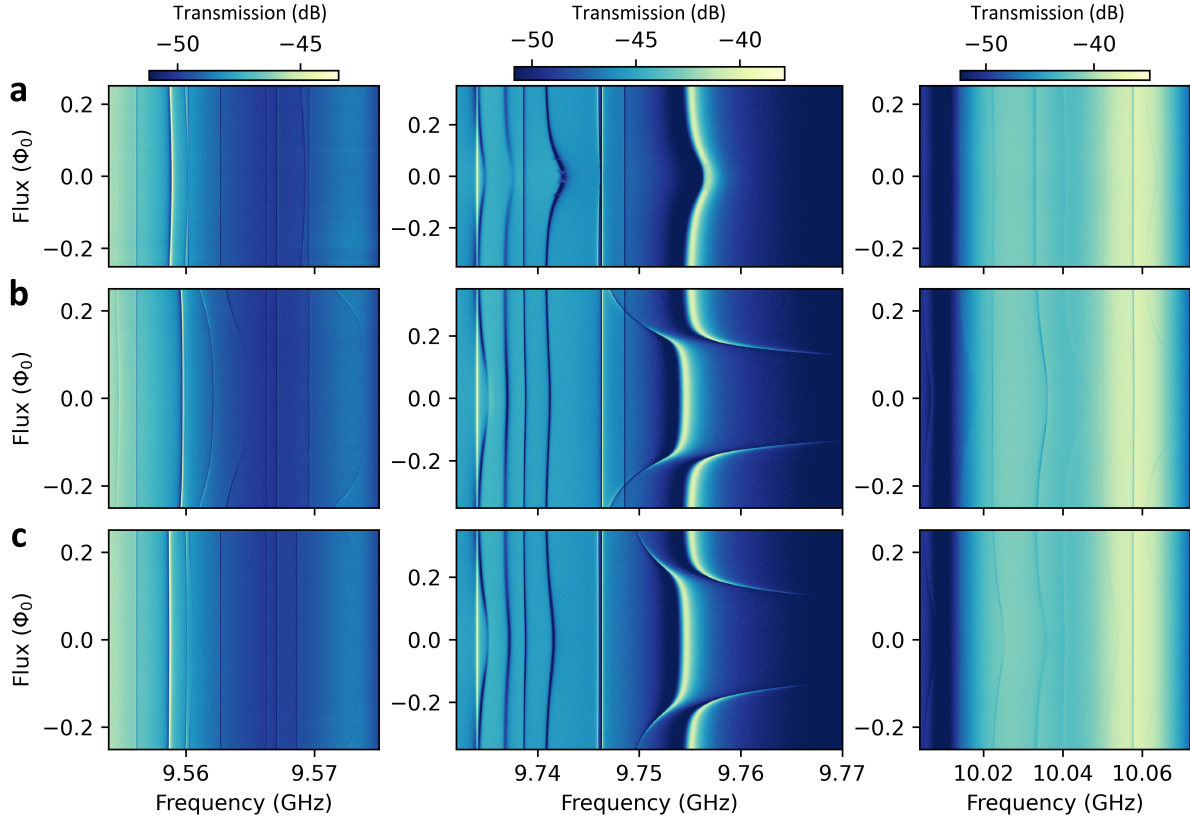
Figure 5.13: **Zoomed In Full-Wave Transmission Data** Fine S21 transmission scans of modes in all full-wave bands. The left column contains modes from the gapped flat band, the middle column is the middle band, which contains an ungapped flat band, and the right column contains the highest energy band. Rows **a, b,** and **c** correspond to qubits Q2, Q3, and Q1, respectively. This scan helps us observe fainter modes and the weaker qubit-mode interactions.

qualitative agreement. We performed this measurement as a function of input power. At higher powers, we enter the punch-out regime discussed in Ch. 3.2, decouple the modes from qubits, and observe a shift in mode frequencies. We see an example of the entering this regime in Fig. 5.17, where at a certain drive power, the mode frequency shifts.

Qubit Spectroscopy vs. Transmission Data

We characterized the qubits for this lattice individually using two-tone spectroscopy measurements, which we described in Ch. 4.3. By overlaying this data on S21 transmission data, we
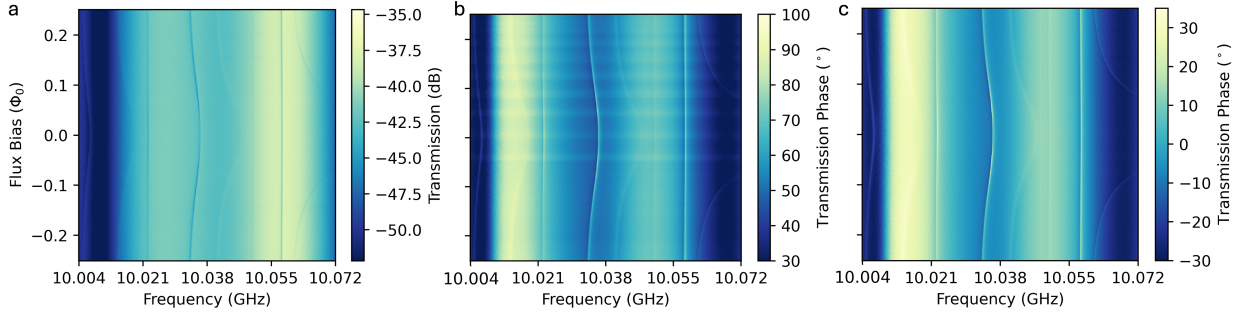
Figure 5.14: **a-** Transmission data in magnitude. **b-** Transmission data in phase is clearer compared to data in magnitude. However, we observe some streaks in the data. These are due to the occasional changes in phase background. **c-** Background subtracted phase data was achieved by subtracting the mean of each row from the same row of data. Here we achieve the best visibility for this band of modes.
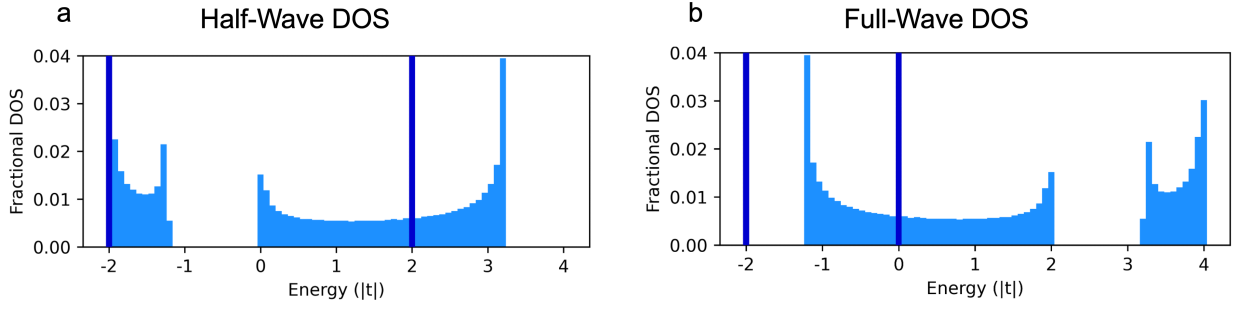

Figure 5.15: **Fractional Density of States for Lattice Modes** The fractional density of states was determined from simulations for both sets of modes in the lattice. Comparison between these plots and transmission data shows good qualitative agreement between theory and experimental data. The location of flat-bands (shown using dark blue lines) and the band gaps are specifically in good agreement between data and simulation.

gain some insight into the behavior of the system. In Fig. 5.18, we show the qubit using two-tone spectroscopy data in orange, and overlay it on half-wave transmission data.

In Fig. 5.19, we see that the qubit, shown using the yellow curved line, does not reach the bottom of the band, and turns around near 9.53 GHz. This implies that this line is not purely qubit in characteristic. It rather is the dressed excitation of the qubit with the lattice. The spectroscopy data in the band-gaps shows the qubit-photon bound state.

We also use qubit spectroscopy data to approximate qubit parameters. By tracking qubit Q2 in a wide frequency range (as seen in Fig. 5.20), we were able to approximate the qubit

88
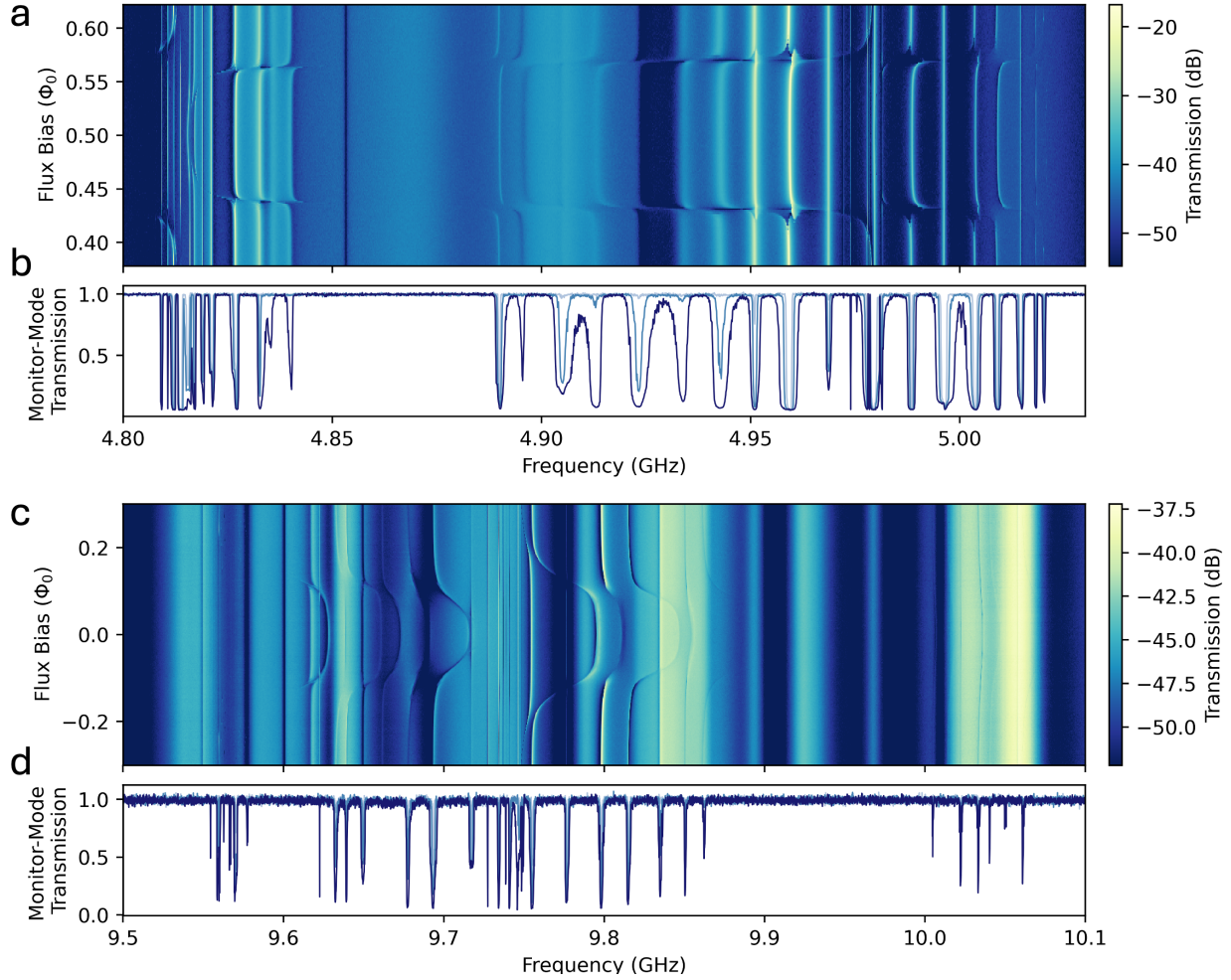
Figure 5.16: **Non-Linear Mode-Mode Spectroscopy a, c-** Transmission data for half-wave and full-wave modes interacting with qubit Q3. We compare mode transmission with mode-mode spectroscopy in **b, d**, with the all three qubits far away around 7 GHz. Only non-linear modes appear in mode-mode spectroscopy. The location of modes is in good qualitative agreement with the simulated band structure.

parameters. We find that $E_C \approx 190$ MHz, and $E_J \approx 7$ GHz. These values do not agree with design values, and need to be investigated further.

Additionally, it is worth noting that qubit spectroscopy is difficult to observe in certain regions. It is important to optimize the qubit and the cavity powers when taking measurements, and to optimize trace averaging times. It is recommended to take a single trace of the data on the VNA for each region, and optimize these parameters before setting up a long scan to produce a

Figure 5.17: **Punch-Out Regime** We send a signal in at a monitor mode around 4.96 GHz, and driving a different mode around 9.695 GHz. As we increase th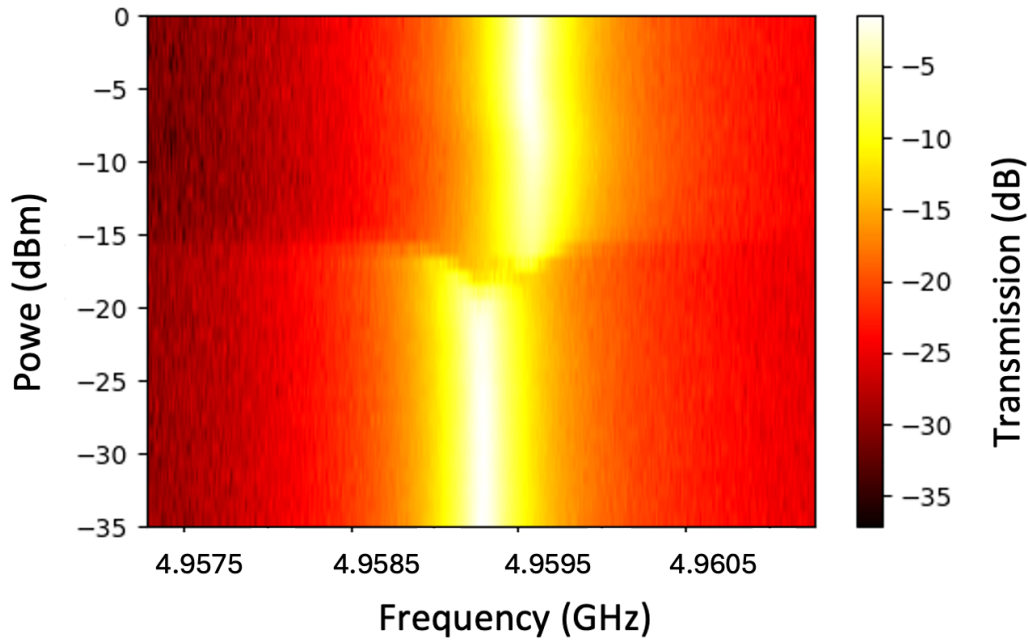e power of the drive mode, shown on the y-axis, we see a sudden shift in the frequency of the monitor mode. This implies that we have entered the punch-out regime, and the mode has shifted to its bare frequency.

plot like the one seen in Fig. 5.20.

Qubit-Qubit Interactions

We have observed qubit-qubit interactions between pairs of qubits. These interactions are mediated by photons. Near full-wave modes, Q2 and Q1 interact in the lower band-gap and in the middle band. They also interact below the band-edge of the half-wave modes. Q2 and Q3 were also seen interacting in the lower band-edge of the full-wave modes. These interactions are shown in Fig. 5.21. We were unable to observe such interactions deeper in the band-gap. For these data sets, we calibrated the flux cross-talk between the qubits. Tuning the flux of each qubit has a small effect on the flux of the other two. Hence, to be able to keep qubits constant in frequency, or tune them to the desired flux point, we used the method described in Appendix C to compensate for

90
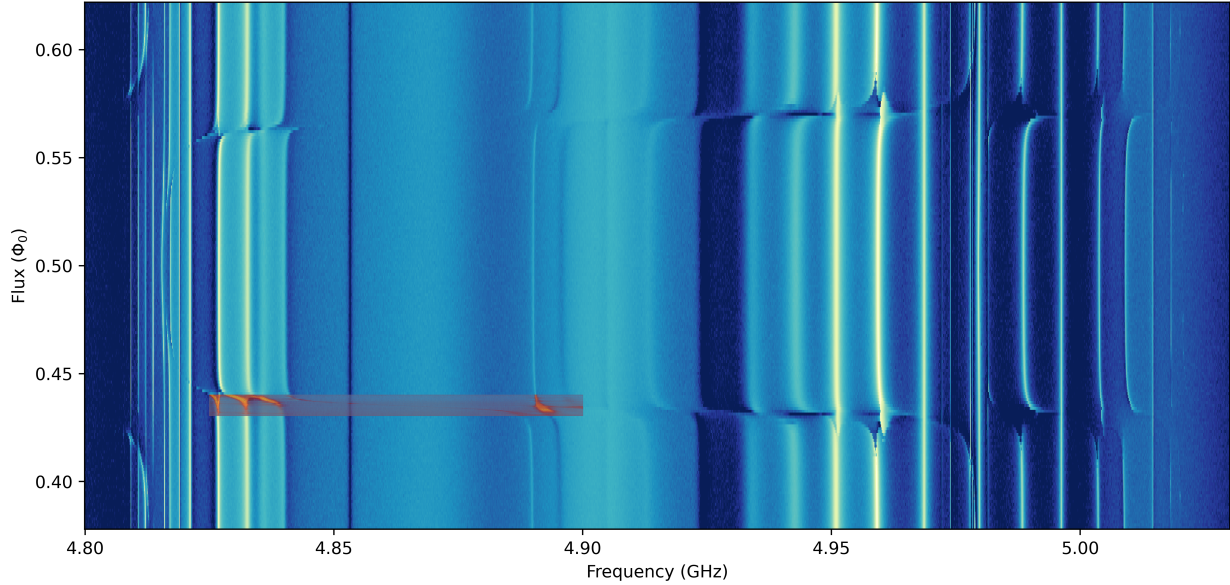
Figure 5.18: **Half-Wave Transmission and Spectroscopy Data for Q3** Two-tone spectroscopy data for qubit Q3 is shown in orange, and the data is overlaid on transmission data.

this cross-talk.

In the data near the half-wave modes (lower left panel) we observe that qubit Q1 has a curvature close to the band-edge of the half-wave modes. This is due to the interaction of the qubit with the modes. We also notice that there are additional fainter lines in these data sets. This is clearest in the upper left subfigure. The presence of these lines may be due to higher order transitions or two-photon bound states. The origin of these lines needs to be investigated further.

Cross-Kerr

In the dispersive regime, we observe qubit-mediated mode-mode interactions, which was explained in Ch. 2.5, and referred to as cross-Kerr interactions. To observe cross-Kerr effects, we choose two modes "a" and "b", as our drive and monitor modes, respectively. We bring a qubit close to the modes, but keep it off-resonance. The qubit will mediate interaction between the modes (see Fig. 5.22). Then, we increase the drive power for mode "a", and observe a shift
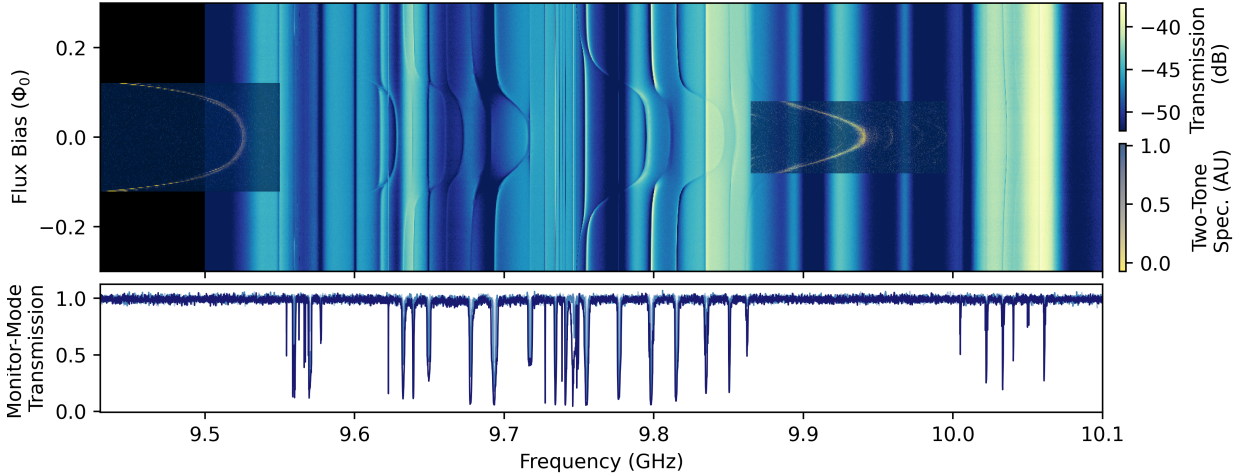
91

Figure 5.19: **Transmission and Spectroscopy Data for Q3** In the upper panel, we see two-tone spectroscopy of the qubit, shown in yellow, overlaid on transmission data. The qubit is not interacting with any of the modes in the 9.9-10 GHz region, implying that those modes are box modes. The mode-mode transmission data in the lower panel confirms that the upper band-gap is in that frequency range, and that no modes in that region couple to the qubit. We also see that the qubit has an avoided crossing with the gapped flat band modes between 9.5 GHz and 9.6 GHz. This implies that while not visible in transmission data, the qubit is interacting strongly with the flat band modes. Note that there is no transmission data available in the black region below 9.5 GHz, as it is below the bands.

in mode "b" due to cross-Kerr. We refer to this measurement as "reverse spectroscopy". We can see a power scan using this type of measurement in Fig. 5.23-**a**. The shift is the signal is due to cross-Kerr, and yields interaction strength. The derivative of the frequency shift with respect to power yields χ. This is because as mentioned in Ch. 2.5, χ depends on the number of photons in the drive mode. Once we know the value of χ, we take a scan to infer the ratio between the qubit coupling with the drive and monitor modes using Eq. 2.48. To do so, we change the qubit detuning from the drive mode, "a", do a power scan similar to the one described above, and find the slope of the cross-Kerr shift for each detuning. Then we plot the slope of the shift for each detuning as a function of detuning itself, as shown in Fig. 5.23-**b**. We observe that smaller detuning between the qubit and the monitor mode results in a stronger interaction. In the data presented in Fig. 5.23, we chose the drive mode to be around 4.94 GHz in frequency, monitor

92
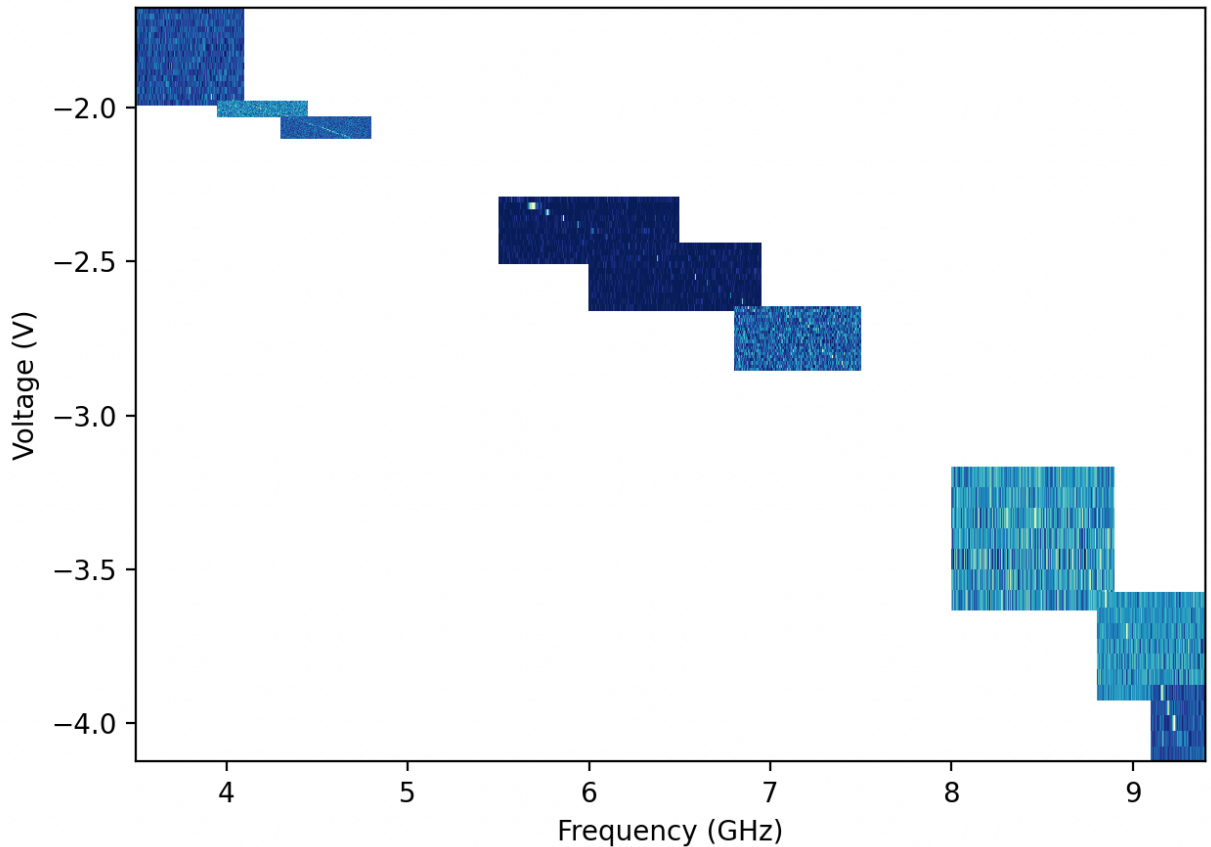
Figure 5.20: **Wide Range Two-Tone Spectroscopy Data for Q2** We tracked qubit Q2 accross a wide range of frequencies. Such scans can help in estimating actual qubit parameters. The qubit is the light discrete line.

mode around 4.96 GHz, and qubit Q1 was chosen as the mediator and placed around 4.6 GHz. Using the method described in this section, we are able to probe modes that are hardly visible in transmission due to their poor coupling to input and output ports of the device. This, of course, is contingent on choosing a mediating qubit that couples to both drive and monitor modes.

In this chapter, we discussed the design and fabrication of a quasi one-dimensional lattice device, as well as the theoretical description of the device. We then presented data from the device, which demonstrates photon-mediated interactions between spins, and cross-Kerr interactions. In Appendix D we will show more results from the device for completeness.
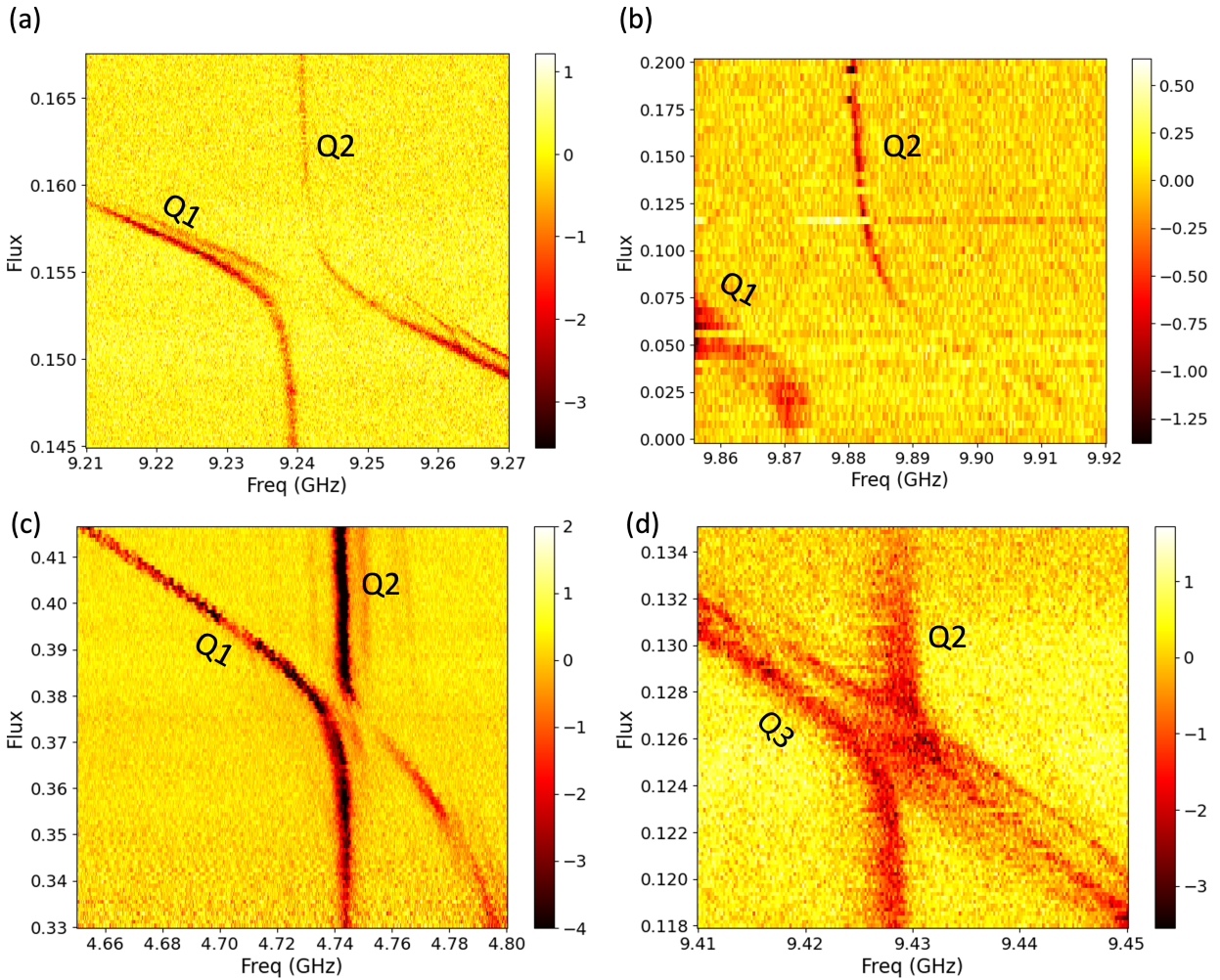
Figure 5.21: **Qubit-Qubit Avoided Crossings** Two-tone spectroscopy of pairs of qubits showing interactions between them. **a, b, c**- We observe avoided crossing between qubits Q1 and Q2 in the lower band-gap of the full-wave modes in **a**, middle band of the full-wave modes in **b**, and below the band-edge of half-wave modes in **c**. **d-** Interaction between Q2 and Q3 in the lower band-edge of full-wave modes.
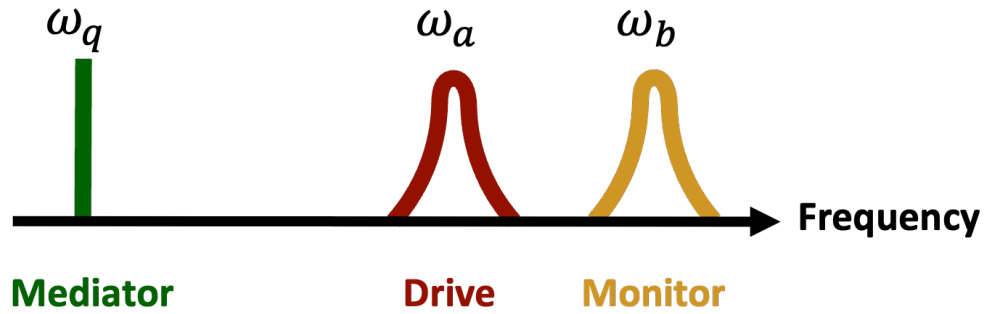
Figure 5.22: **Measuring Cross-Kerr** To measure cross-Kerr, we choose a monitor mode (shown in yellow), and a drive mode (shown in red). We choose a qubit to mediate cross-Kerr and park it off-resonance with respect to the modes (shown in green). We then increase the power in the drive mode (red), and look for a shift in the frequency of the monitor mode (yellow).
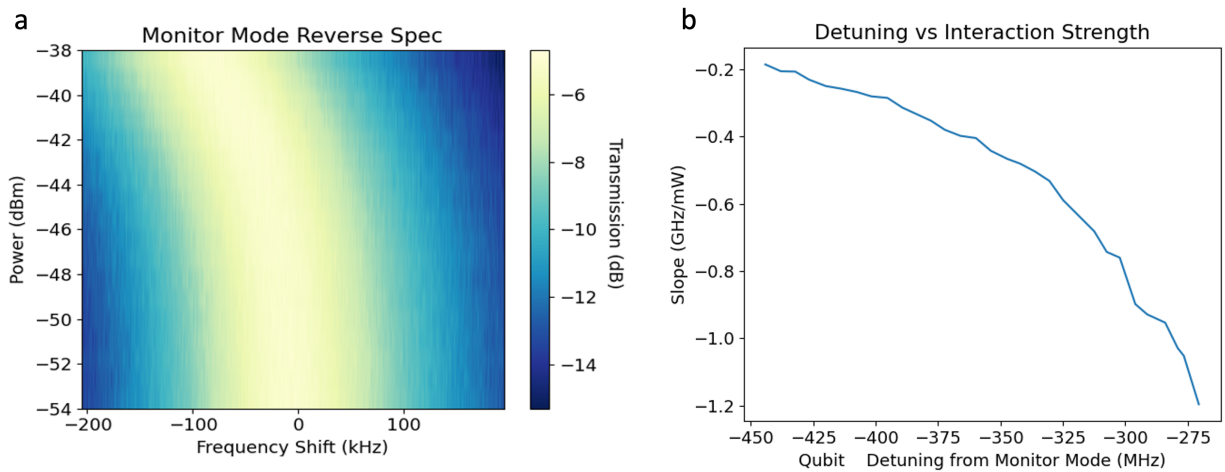
Figure 5.23: **Cross-Kerr Data a-** Reverse spectroscopy of the monitor mode shows a change in its frequency as the power in the drive mode (shown on the y-axis) is increased. The shift in signal is due to cross-Kerr. The monitor and drive modes were chosen to be around 4.96 GHz and 4.94 GHz respectively. **b-** Changing the detuning of the qubit Q1 (interaction mediator) from the monitor mode results in variations in the strength of the interaction between the modes. Smaller detunings yield stronger interactions.

95

Chapter 6:   Conclusion and Outlook

Quantum level interactions between light and matter have been an interesting subject of study for a few decades [24, 25]. In this dissertation, we first studied the Jaynes-Cummings Hamiltonian, which describes a simple level exchange interaction between light and matter. We then explored higher order photon-mediated interactions between qubits, as well as non-linear qubit-mediated interactions between photons.

We designed and fabricated a quasi one-dimensional lattice coupled to qubits to study higher order interactions. In this work, we described the design, fabrication, and measurement of this device. This lattice is of interest due to its unconventional band structure. The flat bands can facilitate strong, short-range interactions between qubits, while the linear and quadratic bands result in long-range, albeit weaker interactions.

We observed cross-Kerr interactions between the photons as well as photon mediated interactions between the qubits in this lattice. These qubit-qubit interactions were observed in flat bands and near band edges. It is important to understand these interactions better and investigate where with respect to the band structure they occur. Additionally, we will examine whether these interactions can be observed between qubits at other lattice sites, for instance qubits Q3 and Q1. It would be interesting to add qubits to unit cells that are far away from each other in later iterations of the device, and observe long-range interactions. Additionally, we are curretnly working

on understanding the cross-Kerr data better, and finding a scheme to fit the data to extract the ratio of the transmon coupling to monitor and drive modes.

The lattice that we introduced contains the simplest modification of the one-dimensional chain. It is a prototype, appropriate for understanding second order interactions in an environment that is not too complex for a first step. In the future, we would like to extend to two-dimensional lattices in flat space and in hyperbolic space [7]. This will allow for studying interactions in two-dimensions, even in a non-Euclidean environment.

Appendix A: Fabrication Recipe

A.1   Dicing a 4 Inch Wafer

- Spin-coat a 4 inch wafer (Tantalum on Sapphire) with AZ1518 at 4000 RPM for 1 minute. Make sure the wafer is metal-side up.

- Bake the wafer at $100°$ C for 4 minutes.

- Stick the wafer metal side up on a blue tape.

- Using the dicing saw to dice the wafer into $1'' \times 1''$ chips using the following parameters:

    - Mode = 60

    - Dim 1 = Dim 2 = 110 mm or larger

    - Index 1 = Index 2 = 25.75 mm

    - Height = 0.05 mm

    - Thickness = 0.6 mm

    - Cut Speed = 0.750 mm/s

    - Increment = 0.125 mm

    Note: It is a good idea to first make a shallow cut on a piece of junk Silicon to make

sure the cut is in the right spot on the camera. You can increase the cut speed to

2 **mm/s for Silicon.**

A.2 Three Solvent Clean

- Soak chips in 1165 for > 1 hour at $80°$ C.

- Sonicate in 1165 for 30 seconds.

- Transfer to a clean beaker of 1165 and sonicate for 30 seconds.

- Transfer to acetone while spraying with acetone.

- Transfer to IPA while spraying with IPA.

- Blow dry with N2.

A.3 Photolithography

You can either use the mask aligner with a photomask or the Heidelberg Maskless Aligner (MLA 150), which is a direct write system that uses your CAD design.

Exposure Using Mask Aligner

- Spin AZ1518 on the chip at 4000 RPM for 1 minute. Do this in the clean room under yellow lights.

- Bake the chip for 4 minutes at $100°$ C.

- Use the mask aligner to expose the chip for 12 seconds. You can use a shorter exposure time if your features are smaller than designed or rounded. For my first lattice device, for instance, I used an 8 second exposure.

Exposure Using Heidelberg MLA 150

- Spin AZ1518 on the chip at 4000 RPM for 1 minute. Do this in the clean room under yellow light.

- Bake the chip for 4 minutes at $100°$ C.

- If you need to transfer your sample to a different room under blue light, use a dark GelPak and cover it in aluminum foil to avoid unwanted exposure.

- Use MLA150 with 375 nm laser for AZ1518.

- Expose pattern with a dose of 290 mJ/cm^2. 320 mJ/cm^2 is a bit overdosed (features are roughly 18% bigger than they should be).

- Use the correct sample size. For 7 mm $\times$ 7 mm samples use the "Maya small 7 x 7" option. Do not place chips that are smaller than 6 mm x 6 mm in MLA 150.

- Center the design manually and carefully.

- Note: Features that contain other features inside them must be in different layers in the CAD design.

Develop Photo Layer

- After exposure, develop in CD-26 MIF for 1 minute.

- Transfer to DI water to stop developing.

- Blow dry with Nitrogen.

- Check under the optical Microscope to make sure features are of the correct size and shape.

Etching

- Etch in Tantalum Etchant (made mainly of HF) for 21 seconds.

- Transfer to DI water to stop the etch.

- Blow dry with N2.

A.4 Prepare for e-Beam Lithography

Dicing into Smaller Chips

- Do the three-solvent clean mentioned in section A.2 to remove excess photoresist.

- Spin AZ1518 on the chip at 4000 RPM for 1 minute.

- Bake the chip at $100°$ C for 4 minutes.

- Use the dicing saw to cut the chip into 7 mm $\times$ 7 mm pieces using the following parameters:

    - Mode = 60

- Dim 1 = Dim 2 = 30 mm

- Index 1 = Index 2 = 7.35 mm

- Height = 0.050 mm

- Thickness = 0.6 mm

- Cut Speed = 0.750 mm/s

- Increment = 0.125 mm

- For 10 mm × 10 mm chips change Index 1 = Index 2 = 10.3 mm.

Three-solvent Clean (see section A.2)

TAMI Clean

- Sonicate in Toluene, Acetone, Methanol, and Acetone for 2 minutes each, in the order mentioned.

- Spray with the next solvent before transferring to the new beaker.

- Blow dry with Nitrogen.

Piranha Clean

- Fill a beaker with 2 parts H2SO4 (Sulfuric Acid).

- Fill a beaker with 1 part H2O2 (Hydrogen Peroxide).

- Slowly and gently pour H2O2 into H2SO4.

! Never mix rapidly. The mixture will get too hot and could shatter your beaker.

! Never do this in reverse. It will blow up!

! Never use carbon fiber or metal tweezers. Use only plastic ones.

! Always cover the work surface with PIG Pads and wear appropriate PPE.

- Leave chips in Piranha for 20 minutes.

- Spray chips with DI water in a separate beaker for 30 seconds.

- Immediately spray with IPA, before the DI water dries on your chip.

- Blow dry with N2.

Spinning e-Beam Resist and Evaporating Anti-charging Layer

- Spin MMA at 5000 RPM for 1 minute.

- Bake at $175°$ C for 2 minutes.

- Spin PMMA at 4000 RPM for 1 minute.

- Bake at $175°$ C for 30 minutes.

- Using the sputterer or the Plassys to coat your chip in a 30 nm thick layer of Aluminum.

A.5   e-Beam Lithography

e-Beam Write

- Use the Elionix with a 0.5 nA beam current.

- Use $500 \ \mu$m write fields and 50,000 dots per field.

- Use 1x1 shot pitch.

- For Manhattan style junctions use $1000 \ \mu$C/cm^2 for the full clear layer dose, and $230 \ \mu$C/cm^2 for the undercut layer.

- For Dolan Bridges use $1500 \ \mu$C/cm^2 for the full clear layer dose, $230 \ \mu$C/cm^2 for the undercut layer.

Developing Manhattans

- Remove the anti-charging layer by soaking the chip in AZ300-MIF for 5 minutes.

- Rinse with DI water.

- Blow dry with N2.

- Develop in MIBK:IPA (1:3) for 50 seconds.

- Soak in IPA for 10 seconds.

- Rinse with DI water.

- Blow dry with N2.

Developing Dolans

- Remove the anti-charging layer by soaking the chip in AZ300-MIF for 5 minutes.

- Mix 3 parts of IPA with 1 part of DI Water in a glass bottle.

- Put the mixture in a chiller set to $6°$ C for 2-3 hours depending on the size of the bottle.

- Fill a large beaker/dish with water and put it in the fridge for 3-4 hours to get it down to $3°$ C. This will be your bath.

- Take the bath out of the fridge, put a clean, empty beaker in it, and wait for the water temperature to get to $5°$ C.

- Put 4 ice cubes in the bath, and pour developer in the clean beaker.

- Develop chip for 2 minutes, while agitating the solution.

- Blow dry with N2.

Note: There is no need to mix a fresh batch of developer every time.

Double-Angle Evaporation for Dolans

- Load your sample in the Plassys, noting the desired evaporation direction. Pump down for ~ 12 hours or more, until the load lock pressure reaches $\sim 9.4e^{-8}$ mBar.

- Perform Argon Ion etch for 45 seconds for each evaporation angle using the following IBG parameters: anode voltage 400 V, emitter current 20 mA, acceleration voltage 80 V.

- Evaporate Ti at 0.2 nm/s for 2 minutes.

- Wait for chamber pressure to drop to low e^{-8} mBar again.

- Evaporate 30 nm of Al at 0.5 nm/s with a $25°$ tilt.

- Oxidize using static oxidation for 10 minutes at 2.33 mBar.

- Evaporate 50 nm of Al at $-25°$ tilt and 0.5 nm/s.

- Oxidize at 40 mBar for 20 minutes.

Double-Angle Evaporation for Manhattans

- Load your sample in the Plassys, noting the desired evaporation direction. Pump down for ~ 12 hours or more, until the load lock pressure reaches $\sim 9.4e^{-8}$ mBar.

- Perform Argon Ion etch for 40 seconds for each evaporation angle using the following parameters for the IBG: anode voltage 400 V, emitter current 20 mA, acceleration voltage 80 V.

- Evaporat Ti at 0.2 nm/s for 2 minutes.

- Move planetary to the first evaporation direction and evaporate 30 nm of Al at 0.5 nm/s.

- Oxidize at 2.33 mBar for 10 minutes.

- Move planetary to the second desired evaporation angle. Evaporate 50 nm Al at 0.5 nm/s.

- Oxidize at 40 mBar for 10 minutes.

Lift-Off

- Soak in 1165 at $80°$ C for 3 hours.

- Spray with IPA to remove excess metal.

- Transfer to a clean 1165 beaker and sonicate for 30 seconds.

- Transfer to IPA while spraying with IPA. Sonicate for 30 seconds.

- Blow dry with N2.

A.6 Packaging

- Probe witness junctions before packaging the chip to make sure E_J is reasonable. Use the Ambegaokar-Baratoff relationship from Eq. 3.22 to find this value.

- Sand down a puck to make sure the chip sticks out of its pocket a bit.

- Clean the PCB prior to wire bonding.

- Wire bond using the following parameters for copper to tantalum bonds:

    - Power 1: 230, Power 2: 210

    - Time 1: 20, Time 2: 20

    - Force 1: Low, Force 2: High

- Wire bond using the following parameters for tantalum to tantalum bonds:

    - Power 1: 220, Power 2: 220

    - Time 1: 20, Time 2: 20

    - Force 1: High, Force 2: High

A.7 Preliminary Air Bridge Recipe

- Prepare the CAD with small rectangles where air bridges will be in contact with the chip, and larger rectangles where the air bridge would exist.

- The approximate dimensions for the air bridge should be aas follows: 4 μm clearance from the feature, 28 μm length, and 8 μm width.

- Dehydrate chip for 1 minute at $100°$ C.

- Spin AZ-1518 at 2000 RPM for 1 minute to have a 3 μm thick layer of resist.

- Bake chip at $100°$ C for 4 minutes.

- Expose smaller contact rectangles at 350 mJ/cm^2.

- Develop chip in CD-26 for 1 minute.

- Stop developing in water.

- Blow dry with N2.

- Reflow resist by heating the chip to $135°$ C for 4 minutes.

- Deposit 300 nm of aluminum

    - First do an Argon ion mill for 2 mins at $9.5e^-4$ mBar with 400 V and 20 mA.

- Spin AZ-1518 at 2000 RPM for 1 minute.

- Expose the entire chip, except for the larger rectangles where the air bridges would be, at 350 mJ/cm^2.

- Expose the edge beads separately at 290 mJ/cm^2 again.

- Develop chip in CD-26 for 1 minute.

- Stop developing in water.

- Blow dry with N2.

- Etch in Aluminum Etchant Type D for 7.5 minutes at $50°$ C.

- Stop the etch in DI water for 3 minutes.

- Strip both layers of resist at $80°$ C in 1165 for 25 minutes.

- Transfer to a fresh beaker of 1165 and soak for 5 minutes at room temperature.

- Soak in Acetone for 20 seconds.

- Soak in IPA for 20 seconds.

- Very carefully and gently blow dry with N2.

- Inspect under optical microscope.

- **Note:** To add/use alignment marks, add an exposure layer when setting up the job in the MLA150 software. Leave the "First Exposure" layer blank, and add your design as well as alignment marks to "Layer 2". Then select "Layer 2" by clicking on it before proceeding to load the substrate.

A.8   Cautionary Tales

- Do not swirl or sonicate chips when removing the anti-charging layer. The anti-charging would peel off instead of dissolving, and would peel of parts of the resist with it (see Fig. A.1). Do take the chips in and out of the developer gently a few times to prevent the formation of bubbles.

- When making air bridges, do not spray the chips with solvents. This naturally makes the air bridges fly off of the chips.

- When making air bridges, be very careful how you blow dry the chips with nitrogen. Do not spray nitrogen on the chip directly from above.

- Always monitor the voltage and the deposition rate when doing an evaporation using the Plassys. This indicates when the crucible is low on material and needs to be refilled.

- Try not to use expired resist and developer. This can change your dosage or developing time.

- Using expired AZ300-MIF could result in the anti-charging layer being removed in chunks and not being properly dissolved.

- If you are in a rush and do not have access to fresh AZ300-MIF, you can use Aluminum Etchant Type D for a short time. If you do so, visually inspect the chip. Once you see that the anti-charging layer is gone, wait an extra 10 seconds before removing the chip from the etchant.

- It is always best to spin resist the same day as your e-beam write (or keep the time between when you spin resist and your write constant across all writes). The resist can harden over time and cause variations in your carefully optimized exposure dose. This is not extremely sensitive, so an additional day will not ruin your doses. But waiting a week longer might have a noticeable effect.

- Do not use SEM on a chip that has resist on it. The beam will melt the resist and distort the features. You will not be able to get accurate information.

- When using the elionix, do not stay on one alignment mark (or any part of the chip) with the beam un-blanked for too long. Again, the beam will melt the resist. You will see cracks or bubles forming.

- When using the elionix, do not re-adjust the beam focus and stigma after having determined the height at which the write will be performed. This will make the beam be out of focus.
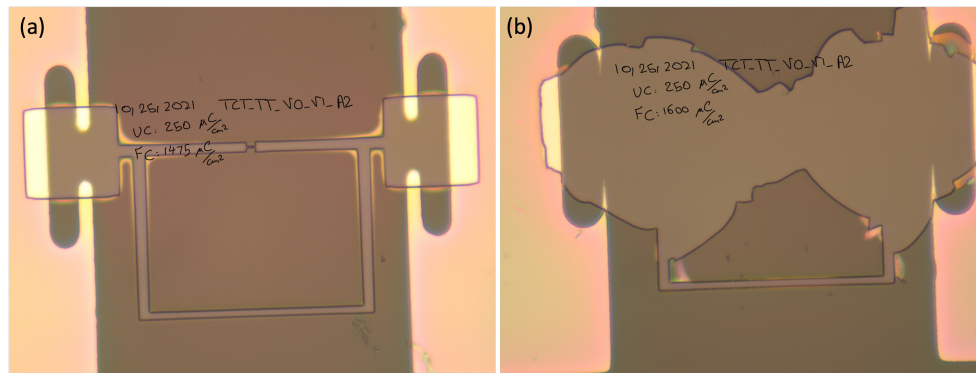

Figure A.1: **Sonicating when Removing Anti-Charging Layer** These chips were used for performing dose tests for Dolan bridges. **a-** While the junctions were not successful, the contact squares had no issues. The anti-charging layer was removed without sonication or swirling the chip, and the pattern was developed after. **b-** This chip was sonicated in AZ300-MIF, as the anti-charging layer was not coming off. Sonication peeled off most of the resist with it. Note: The anti-charging layer might not dissolve if the developer used for etching the pattern has expired, or if the aluminum was contaminated during evaporation.

Appendix B: Frequency Disorder Compensation

In the quasi one-dimensional lattice, the desired half-wave frequency for the resonators is 5 GHz. That number allows us to measure the full-wave modes around 10 GHz using a VNA. That means that each resonator has to be 12.456 mm in length. In order to fit the resonators of that length on such a small chip, we had to bend the resonators. However, bending the resonators has a second-order affect on the resonant frequency due to the specific shape of each resonator. We investigate such affects as the resonators need to be perfectly resonant to minimize disorder in the lattice. This is because the flat-band is highly sensitive to disorder. Hence, we made two chips to measure the frequency of each type of resonator individually and make sure they are equal. The test devices are shown in Fig. B.1.

We measured the resonator frequencies to be 4.8957 ± 0.001 GHz for 3 types of resonators (in Fig. B.1, these are the bottom left resonator and the two resonators on the right). At 4.8778 GHz, the fourth type (top left in the same figure), which is the resonator connecting unit cells, was a bit lower in frequency compared to the rest. We calculated the correction to the length and removed 45.48 μm from those resonators. The frequency of that resonator is given by $\nu_1 = \frac{\beta}{\lambda_1}$, where β is a constant consisting of factors of $1/2$ and ϵ_{eff} (the effective permittivity of the sample). Let's call the target frequency ν_0. The length should be λ_0, but it is too long by an
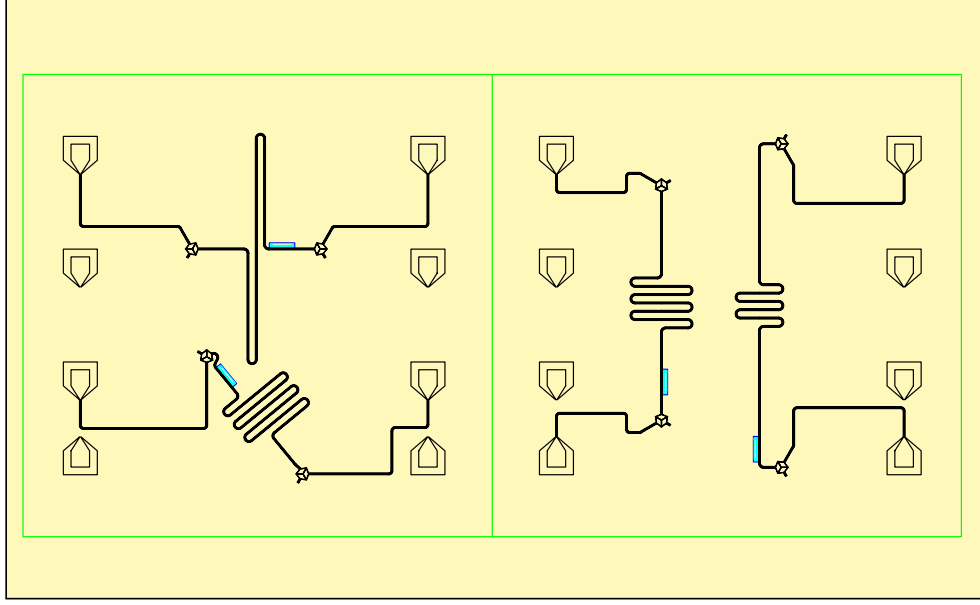
Figure B.1: **CAD design for the test chips** These chips test the frequency of each resonator shape used in the main quasi one-dimensional lattice device. These tests were conducted to minimize and compensate for the variations in frequency when designing the full lattice chip.

amount d. So the current length is $\lambda_1 = \lambda_0 + d$. So we can write

$$\nu_1 = \frac{\beta}{\lambda_0 + d} = \frac{\beta}{\lambda_0} \left(\frac{1}{1 + \frac{d}{\lambda_0}} \right). \tag{B.1}$$

Using Taylor series expansion we find that $\frac{1}{1 + \frac{d}{\lambda_0}} = 1 - \frac{d}{\lambda_0}$. Thus, we can find the correction to the length using the following calculation.

$$
\begin{aligned}
\nu_1 - \nu_0 &\approx \beta \left(\frac{1}{\lambda_0} \left(1 - \frac{d}{\lambda_0} \right) - \frac{1}{\lambda_0} \right) \\
&= -\frac{\beta}{\lambda_0} \frac{d}{\lambda_0} \\
&\approx -\nu_0 \frac{d}{\lambda} \\
&\Rightarrow d \approx \lambda \frac{-\nu_1 - \nu_0}{\nu_0},
\end{aligned}
\tag{B.2}
$$

which as mentioned above, yields that the resonator is $45.48\ \mu$m too long. The main device

contains all the correct lengths.

This bend effect on the frequency that we observed when comparing the four resonators is consistent with simulations performed by Theo Gifford, who was an undergraduate student in the Kollár lab. Based on simulations, he found that the distance between bends in a resonator affects the change in frequency per bend. He also found that the radius of the bends "affects the change in frequency per bend".

Appendix C: Flux Calibration

To calculate the cross-talk between two qubits, we write the following matrix equation [81]

$$
\begin{pmatrix} M_{11} & M_{12} \\ M_{21} & M_{22} \end{pmatrix} \times \begin{pmatrix} V_1 \\ V_2 \end{pmatrix} - \begin{pmatrix} \phi_1^\star \\ \phi_2^\star \end{pmatrix} = \begin{pmatrix} \Phi_1 \\ \Phi_2 \end{pmatrix}.
\tag{C.1}
$$

This equation helps us find a Φ_1 and Φ_2, which are flux points that we can tune the qubits to in order to see them cross one another. To find the matrix M, we calculated the individual elements $M_{ij} = \partial \Phi_i / \partial V_j$ [81].

$$
\frac{\partial \Phi_i}{\partial V_j} = \frac{\partial f_i}{\partial V_j} \bigg/ \frac{\partial f_i}{\partial \Phi_i},
\tag{C.2}
$$

where f_i is the frequency of qubit i, V_i is its voltage, and Φ_i is its flux. But [81]

$$
\frac{\partial f_i}{\partial \Phi_i} = \frac{\partial f_i}{\partial V_i} \bigg/ \frac{\partial \Phi_i}{\partial V_i}.
\tag{C.3}
$$

For $i = j$, $\partial \Phi_i / \partial V_i$ is the inverse of the flux quantum for qubit i. It is easy to take scans similar to the ones in Fig. 5.9 with a larger voltage range, and calculate the flux quantum, $\partial \Phi_i / \partial V_i$, for qubit i. For the cross-talk terms, where $i \neq j$, we take two spectroscopy scans for each qubit. The first data set comes from setting $V_j = 0$, and monitoring f_i while varying V_i. The slope of this scan is equal to $\partial f_i / \partial V_i$. Equipped with this information and the value of the flux quantua,

we can calculate $\partial f_i / \partial \Phi_i$. Then for the second scan, we set the voltage of qubit i to a value that places the qubit in a nice regime based on the information gained from the last data set. We then vary V_j and monitor the change in qubit i. The slope of such a scan yields $\partial f_i / \partial V_j$. Now we have all the information necessary to find all M_{ij}.

Then we multiply the matrix M by V_1 and V_2, which are the voltage values for qubits 1 and 2 respectively. $\begin{pmatrix} \phi_1^\star \\ \phi_2^\star \end{pmatrix}$ is given by the voltage offset when calculating the flux quanta, as the zero flux point is generally not located at $V = 0$.

We modified this method to calculate the cross-talk between all three qubits, Q2, Q3, and Q1. Using this method, it is possible to keep one qubit constant in frequency, while another qubit is swept. It is important to keep in mind that this calibration must be done every time the device is cooled down. This is due to the device aging when it is cycled through the dilution fridge and exposed to oxygen when it is not cold and under vacuum. The aging process can change the R_n and therefore the E_J of the qubits.

Note: The python code for flux-calibration was written by my colleague, Kellen O'Brien, and is available upon request.

Appendix D: Additional Data from Quasi One-Dimensional Lattice

Here, we will present additional data from the lattice device introduces in Ch. 5. The device was cycled in the dilution refrigerator several times, due to repairs and modifications. The transmission data we presented in Ch. 5 for half-wave and full-wave modes are from the fifth time this device was cooled down. It is instructive to compare half-wave transmission data across multiple cool downs, as done in Fig. D.1. During the first cool down of the device, we noticed some parasitic modes. We added more wire bonds to the device (roughly doubled the number of ground plane bonds) between the first and the second cool down. Some parasitic modes, such as the one around 4.8 GHz, were eliminated. However, two bright package modes appeared around 4.875 GHz and 4.925 GHz, which masked some lattice modes. Before the fourth cool down, we replaced the low-frequency HEMT with a high-frequency HEMT to be able to measure full-wave modes. We also noticed that the package modes got dimmer and narrower as the device packaging aged due to copper oxidation. During the fifth cool down, we noticed periodic-looking streaks in our data, which we discussed in Ch. 4.5. We secured all loose connections using lead shot bags, which eliminated the streaky noise in fifth cool down. The majority of the data sets presented in Ch. 5 are from the fifth cool down. In the fifth cool down, we started converting flux bias line voltages into fluxes and taking measurements by varying values for fluxes. This change is apparent in Fig. D.1-**d**.
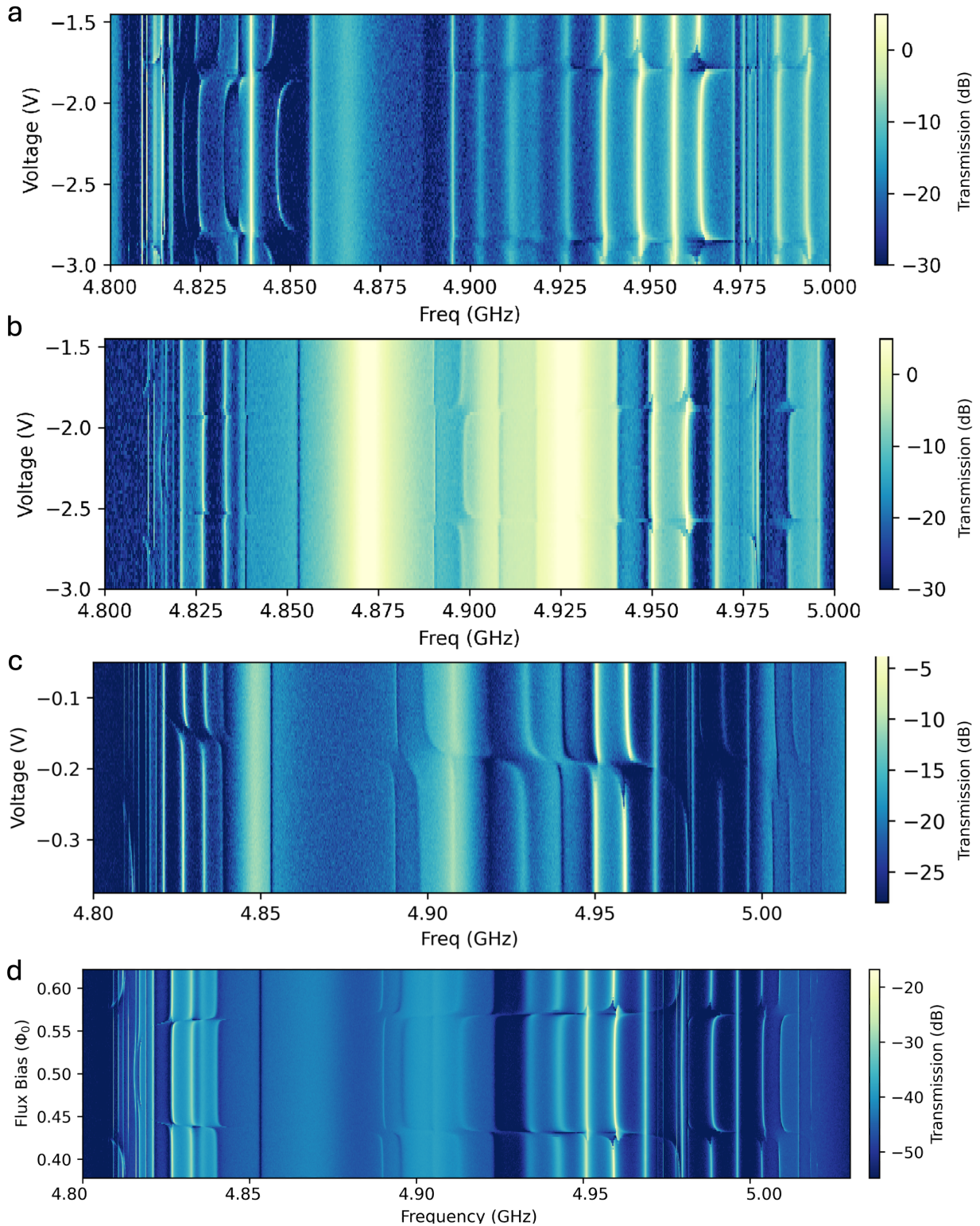
Figure D.1: **Half-Wave Transmission Data Across Various Cool Downs a-** First cool down **b-** Second cool down **c-** Fourth cool down **d-** Fifth cool down. See description in text. Note: data sets do not utilize the same qubit.

We looked at qubit spectroscopy overlaid on half-wave transmission data for qubit Q3 in Fig. 5.18. We have collected similar data for qubits Q2 and Q1 near the lower band of the half-wave modes. Fig. D.2 shows qubit spectroscopy for qubit Q2 in blue, and Fig. D.3 shows the same for qubit Q1.
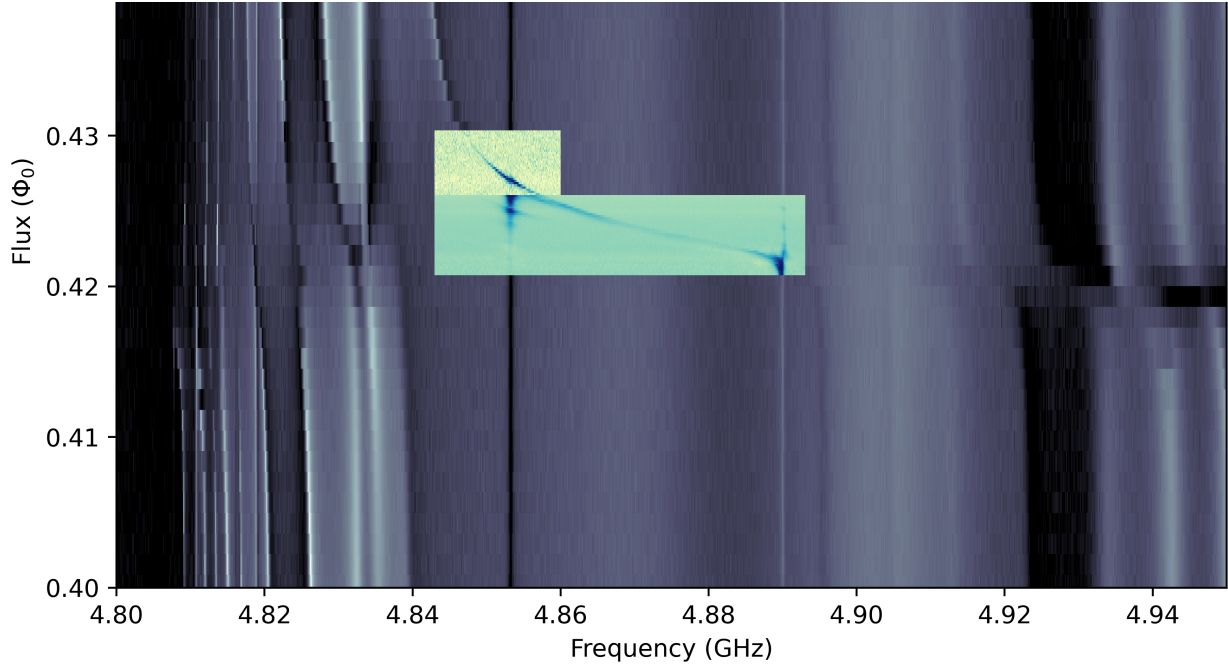

Figure D.2: **Half-Wave Transmission and Spectroscopy Data for Q2** Two-tone spectroscopy data for qubit Q2 is shown in blue, and it is overlaid on transmission data, shown in gray. The qubit is tracked into the lower band-gap.

We introduced mode-mode spectroscopy in Ch. 5.3, and presented results in Fig. 5.16. We collected the same type of data as we varied the power. As we see in Fig. D.4, more modes appear as we increase the input power, while others get power broadened. This confirms that the coupling to input and output ports of the device varies between modes.
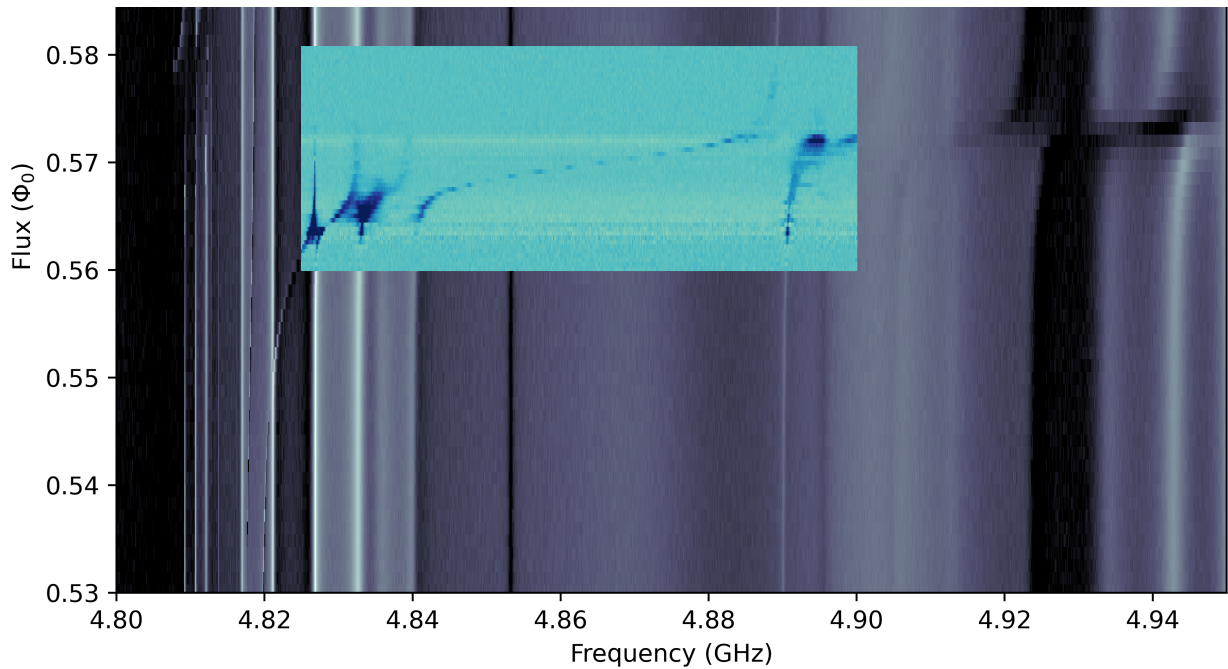
Figure D.3: **Half-Wave Transmission and Spectroscopy Data for Q1** Two-tone spectroscopy data for qubit Q1 is shown in blue, and the spectroscopy data is overlaid on transmission data, which is shown in gray. The qubit is tracked into the lower band-gap.

Figure D.4: **Varying Mode-Mode Spectroscopy Power** Mode-mode spectroscopy for half-wave modes on the left, and for full wave modes on the right. Input power of the drive tone was varied, and is shown on the y-axis. Certain modes appear at higher powers, while others get power broadened.

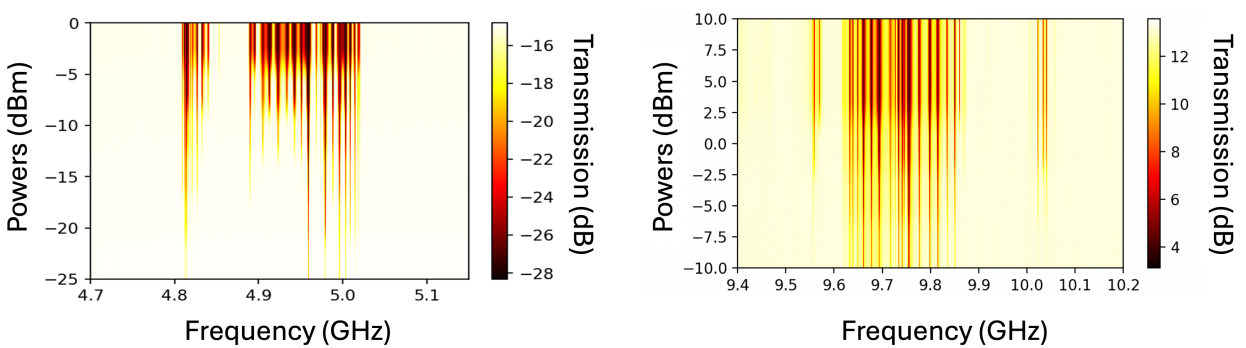# Bibliography

[1] Andrew J Daley, Immanuel Bloch, Christian Kokail, Stuart Flannigan, Natalie Pearson, Matthias Troyer, and Peter Zoller. Practical quantum advantage in quantum simulation. *Nature*, 607(7920):667–676, 2022.

[2] Alejandro González-Tudela, Andreas Reiserer, Juan José García-Ripoll, and Francisco J. García-Vidal. Light–matter interactions in quantum nanophotonic devices. *Nature Reviews Physics*, Jan 2024.

[3] Andrew A Houck, Hakan E Türeci, and Jens Koch. On-chip quantum simulation with superconducting circuits. *Nature Physics*, 8(4):292–299, 2012.

[4] J. Majer, J. M. Chow, J. M. Gambetta, Jens Koch, B. R. Johnson, J. A. Schreier, L. Frunzio, D. I. Schuster, A. A. Houck, A. Wallraff, A. Blais, M. H. Devoret, S. M. Girvin, and R. J. Schoelkopf. Coupling superconducting qubits via a cavity bus. *Nature*, 449(7161):443–447, Sep 2007.

[5] D. L. Underwood, W. E. Shanks, Jens Koch, and A. A. Houck. Low-disorder microwave cavity lattices for quantum simulation with photons. *Phys. Rev. A*, 86:023837, Aug 2012.

[6] Alicia J. Kollár, Mattias Fitzpatrick, Peter Sarnak, and Andrew A. Houck. Line-Graph Lattices: Euclidean and Non-Euclidean Flat Bands, and Implementations in Circuit Quantum Electrodynamics. *Communications in Mathematical Physics*, 376(3):1909–1956, Jun 2020.

[7] Alicia J. Kollár, Mattias Fitzpatrick, and Andrew A. Houck. Hyperbolic lattices in circuit quantum electrodynamics. *Nature*, 571(7763):45–50, Jul 2019.

[8] Yanbing Liu and Andrew A Houck. Quantum electrodynamics near a photonic bandgap. *Nature Physics*, 13(1):48–52, Aug 2017.

[9] Yanbing Liu. *Reservoir engineering in circuit quantum electrodynamics*. Phd thesis, Princeton University, 2016.

[10] Sajeev John and Jian Wang. Quantum optics of localized light in a photonic band gap. *Phys. Rev. B*, 43:12772–12789, Jun 1991.

[11] Steven M. Girvin. Circuit QED: superconducting qubits coupled to microwave photons. In Michel Devoret, Benjamin Huard, Robert Schoelkopf, and Leticia F. Cugliandolo, editors, *Quantum Machines: Measurement and Control of Engineered Quantum Systems*, pages 113–256. Oxford University PressOxford, 1 edition, Jun 2014.

[12] David Isaac Schuster. *Circuit Quantum Electrodynamics*. Phd thesis, Yale University, 2007.

[13] Philip Krantz, Morten Kjaergaard, Fei Yan, Terry P. Orlando, Simon Gustavsson, and William D. Oliver. A Quantum Engineer's Guide to Superconducting Qubits. *Applied Physics Reviews*, 6(2):021318, Jun 2019. arXiv:1904.06560 [cond-mat, physics:physics, physics:quant-ph].

[14] Philippe Grangier, Juan Ariel Levenson, and Jean-Philippe Poizat. Quantum non-demolition measurements in optics. *Nature*, 396(6711):537–542, Dec 1998.

[15] D. A. Steck. *Quantum and Atom Optics*. University of Oregon, 2007.

[16] Neereja M. Sundaresan, Rex Lundgren, Guanyu Zhu, Alexey V. Gorshkov, and Andrew A. Houck. Interacting qubit-photon bound states with superconducting circuits. *Phys. Rev. X*, 9:011–021, Feb 2019.

[17] Neereja M. Sundaresan. *Strong Coupling of Qubits to Spectrally Structures Media Using Superconducting Qubits*. Phd thesis, Princeton University, 2018.

[18] Matthew Elliott, Jaewoo Joo, and Eran Ginossar. Designing Kerr interactions using multiple superconducting qubit types in a single circuit. *New Journal of Physics*, 20(2):023037, Feb 2018.

[19] M. Göppl, A. Fragner, M. Baur, R. Bianchetti, S. Filipp, J. M. Fink, P. J. Leek, G. Puebla, L. Steffen, and A. Wallraff. Coplanar Waveguide Resonators for Circuit Quantum Electrodynamics. *Journal of Applied Physics*, 104(11):113904, Dec 2008. arXiv:0807.4094 [cond-mat].

[20] Jens Koch, Terri M. Yu, Jay Gambetta, A. A. Houck, D. I. Schuster, J. Majer, Alexandre Blais, M. H. Devoret, S. M. Girvin, and R. J. Schoelkopf. Charge-insensitive qubit design derived from the Cooper pair box. *Physical Review A*, 76(4):042319, Oct 2007. Publisher: American Physical Society.

[21] Alexandre Blais, Steven M. Girvin, and William D. Oliver. Quantum information processing and quantum optics with circuit quantum electrodynamics. *Nature Physics*, 16(3):247–256, Mar 2020.

[22] Alfred Perot and Charles Fabry. On the application of interference phenomena to the solution of various problems of spectroscopy and metrology. *Astrophys. J.*, 9:87, Feb 1899.

[23] L. Frunzio, A. Wallraff, D. Schuster, J. Majer, and R. Schoelkopf. Fabrication and characterization of superconducting circuit qed devices for quantum computation. *IEEE Transactions on Appiled Superconductivity*, 15(2):860–863, Jun 2005.

[24] David Wineland. Nobel lecture. *Nobel Prize Outreach*, 2012.

[25] Serge Haroche. Nobel lecture. *Nobel Prize Outreach*, 2012.

[26] J. McKeever, A. Boca, A. D. Boozer, R. Miller, J. R. Buck, A. Kuzmich, and H. J. Kimble. Deterministic generation of single photons from one atom trapped in a cavity. *Science*, 303(5666):1992–1994, Mar 2004.

[27] M. Brune, F. Schmidt-Kaler, A. Maali, J. Dreyer, E. Hagley, J. M. Raimond, and S. Haroche. Quantum rabi oscillation: A direct test of field quantization in a cavity. *Phys. Rev. Lett.*, 76:1800–1803, Mar 1996.

[28] Lev S. Bishop, J. M. Chow, Jens Koch, A. A. Houck, M. H. Devoret, E. Thuneberg, S. M. Girvin, and R. J. Schoelkopf. Nonlinear response of the vacuum rabi resonance. *Nature Physics*, 5(2):105–109, Dec 2008.

[29] Alexandre Blais, Arne L. Grimsmo, S. M. Girvin, and Andreas Wallraff. Circuit quantum electrodynamics. *Rev. Mod. Phys.*, 93:025005, May 2021.

[30] S. Haroche, M. Brune, and J. M. Raimond. From cavity to circuit quantum electrodynamics. *Nature Physics*, 16(3):243–246, Mar 2020.

[31] David Zueco, Georg M. Reuther, Sigmund Kohler, and Peter Hänggi. Qubit-oscillator dynamics in the dispersive regime: Analytical theory beyond the rotating-wave approximation. *Phys. Rev. A*, 80:033846, Sep 2009.

[32] D. F. Walls and G. J. Milburn. *Quantum Optics*. Springer Berlin Heidelberg, 2008.

[33] Alexandre Blais, Ren-Shou Huang, Andreas Wallraff, Steven M. Girvin, and Robert J. Schoelkopf. Cavity quantum electrodynamics for superconducting electrical circuits: An architecture for quantum computation. *Phys. Rev. A*, 69:062320, Jun 2004.

[34] Maxime Boissonneault, J. M. Gambetta, and Alexandre Blais. Dispersive regime of circuit QED: Photon-dependent qubit dephasing and relaxation rates. *Physical Review A*, 79(1):013819, Jan 2009. Publisher: American Physical Society.

[35] A. Wallraff, D. I. Schuster, A. Blais, L. Frunzio, R.-S. Huang, J. Majer, S. Kumar, S. M. Girvin, and R. J. Schoelkopf. Strong coupling of a single photon to a superconducting qubit using circuit quantum electrodynamics. *Nature*, 431(7005):162–167, Sep 2004. Number: 7005 Publisher: Nature Publishing Group.

[36] Jay Gambetta, Alexandre Blais, D. I. Schuster, A. Wallraff, L. Frunzio, J. Majer, M. H. Devoret, S. M. Girvin, and R. J. Schoelkopf. Qubit-photon interactions in a cavity: Measurement-induced dephasing and number splitting. *Physical Review A*, 74(4):042318, Oct 2006. Publisher: American Physical Society.

[37] David Tong. *Lectures on Applications of Quantum Mechanics: 2. Band Structure*. University of Cambridge, 2017.

[38] Sebastian Schmidt and Jens Koch. Circuit qed lattices: Towards quantum simulation with superconducting circuits. *Annalen der Physik*, 525(6):395–412, Apr 2013.

[39] Steven M. Girvin and Kun Yang. *Modern Condensed Matter Physics*. Cambridge University Press, 2019.

[40] E. Y. Tsymbal. *Physics 927 Lecture Notes, Section 11: Methods for Calculating Band Structure*. University of Nebraska - Lincoln, 2011.

[41] Yuval Oreg. *Lecture Notes: Concepts of Condensed Matter Physics*. Weizmann Institut of Science, 2018.

[42] A Nunnenkamp, Jens Koch, and S M Girvin. Synthetic gauge fields and homodyne transmission in jaynes–cummings lattices. *New Journal of Physics*, 13(9):095008, sep 2011.

[43] Tao Shi, Ying Hai Wu, Alejandro González-Tudela, and J Ignacio Cirac. Effective many-body hamiltonians of qubit-photon bound states. *New Journal of Physics*, 20(10):105005, Oct 2018.

[44] Giuseppe Calajo, Francesco Ciccarello, Darrick Chang, and Peter Rabl. Atom-field dressed states in slow-light waveguide QED. *Physical Review A*, 93(3):033833, Mar 2016. arXiv:1512.04946 [quant-ph].

[45] A. Goban, C.-L. Hung, S.-P. Yu, J.D. Hood, J.A. Muniz, J.H. Lee, M.J. Martin, A.C. Mc-Clung, K.S. Choi, D.E. Chang, O. Painter, and H.J. Kimble. Atom–light interactions in photonic crystals. *Nature Communications*, 5(1), May 2014.

[46] Gerhard Kirchmair, Brian Vlastakis, Zaki Leghtas, Simon E. Nigg, Hanhee Paik, Eran Ginossar, Mazyar Mirrahimi, Luigi Frunzio, S. M. Girvin, and R. J. Schoelkopf. Observation of quantum state collapse and revival due to the single-photon Kerr effect. *Nature*, 495(7440):205–209, Mar 2013. Number: 7440 Publisher: Nature Publishing Group.

[47] Stojan Rebić, Jason Twamley, and Gerard J. Milburn. Giant kerr nonlinearities in circuit quantum electrodynamics. *Phys. Rev. Lett.*, 103:150503, Oct 2009.

[48] Jeffrey Wack. *Superconducting Coplanar Waveguides: Shape and Frequency*. Bachelors thesis, University of Maryland, College Park, 2022.

[49] Vladimir E. Manucharyan, Jens Koch, Leonid I. Glazman, and Michel H. Devoret. Fluxonium: Single cooper-pair circuit free of charge offsets. *Science*, 326(5949):113–116, Oct 2009.

[50] C. Gardiner and P. Zoller. *The Quantum World of Ultra-Cold Atoms and Light Book II: The Physics of Quantum-Optical Devices*. Cold Atoms. Imperial College Press, 2015.

[51] M. Tinkham. *Introduction to Superconductivity*. Dover Books on Physics Series. Dover Publications, 2004.

[52] John Bardeen, Leon N. Cooper, and John Robert Schrieffer. Theory of superconductivity. *Phys. Rev.*, 108:1175–1204, Dec 1957.

[53] B. T. Matthias, T. H. Geballe, and V. B. Compton. Superconductivity. *Rev. Mod. Phys.*, 35:1–22, Jan 1963.

[54] Julian Eisenstein. Superconducting elements. *Rev. Mod. Phys.*, 26:277–291, Jul 1954.

[55] Charles Kittel. *Introduction to Solid State Physics*. Wiley, 2004.

[56] Brian D. Josephson. Possible new effects in superconductive tunnelling. *Physics Letters*, 1(7):251–253, Jul 1962.

[57] Alexandre Blais, Arne L. Grimsmo, S. M. Girvin, and Andreas Wallraff. Circuit quantum electrodynamics. *Rev. Mod. Phys.*, 93:025005, May 2021.

[58] Vinay Ambegaokar and Alexis Baratoff. Tunneling between superconductors. *Phys. Rev. Lett.*, 10:486–489, Jun 1963.

[59] John Clarke and Frank K Wilhelm. Superconducting quantum bits. *Nature*, 453(7198):1031–1042, Jun 2008.

[60] Y. Nakamura, Yu. A. Pashkin, and J. S. Tsai. Coherent control of macroscopic quantum states in a single-cooper-pair box. *Nature*, 398(6730):786–788, apr 1999.

[61] Michael J. Peterer, Samuel J. Bader, Xiaoyue Jin, Fei Yan, Archana Kamal, Theodore J. Gudmundsen, Peter J. Leek, Terry P. Orlando, William D. Oliver, and Simon Gustavsson. Coherence and decay of higher energy levels of a superconducting transmon qubit. *Phys. Rev. Lett.*, 114:010501, Jan 2015.

[62] John Clarke. Chapter 2 - squids: Principles, noise, and applications. In Steven T. Ruggiero and David A. Rudman, editors, *Superconducting Devices*, pages 51–99. Academic Press, 1990.

[63] Nathan K. Langford. Circuit qed - lecture notes, 2013. arXiv 1310.1897.

[64] Michel H. Devoret and John M. Martinis. *Implementing Qubits with Superconducting Integrated Circuits*, pages 163–203. Springer US, Boston, MA, 2005.

[65] John M. Martinis, S. Nam, J. Aumentado, K. M. Lang, and C. Urbina. Decoherence of a superconducting qubit due to bias noise. *Phys. Rev. B*, 67:094510, Mar 2003.

[66] S. M. Anton, J. S. Birenbaum, S. R. O'Kelley, V. Bolkhovsky, D. A. Braje, G. Fitch, M. Neeley, G. C. Hilton, H.-M. Cho, K. D. Irwin, F. C. Wellstood, W. D. Oliver, A. Shnirman, and John Clarke. Magnetic flux noise in dc squids: Temperature and geometry dependence. *Phys. Rev. Lett.*, 110:147002, Apr 2013.

[67] Roger H. Koch, David P. DiVincenzo, and John Clarke. Model for $1/f$ flux noise in squids and qubits. *Phys. Rev. Lett.*, 98:267003, Jun 2007.

[68] Peter James Joyce O'Malley. *Superconducting qubits: dephasing and quantum chemistry*. Phd thesis, University of California, Santa Barbara, 2016.

[69] Sal J. Bosman, Mario F. Gely, Vibhor Singh, Daniel Bothner, Andres Castellanos-Gomez, and Gary A. Steele. Approaching ultrastrong coupling in transmon circuit QED using a high-impedance resonator. *Physical Review B*, 95(22):224515, Jun 2017.

[70] W. E. Shanks, D. L. Underwood, and A. A. Houck. A scanning transmon qubit for strong coupling circuit quantum electrodynamics. *Nature Communications*, 4(1):1991, Jun 2013. Number: 1 Publisher: Nature Publishing Group.

[71] Jens Koch, Andrew A. Houck, Karyn Le Hur, and S. M. Girvin. Time-reversal-symmetry breaking in circuit-QED-based photon lattices. *Physical Review A*, 82(4):043811, Oct 2010. Publisher: American Physical Society.

[72] Herbert 1922-2005. Goldstein, Charles P. Poole, and John L. Safko. *Classical mechanics*. Addison Wesley, San Francisco, 3rd ed. edition, 2002. Section: xviii, 638 pages : illustrations ; 24 cm.

[73] Aaron Somoroff, Quentin Ficheux, Raymond A. Mencia, Haonan Xiong, Roman Kuzmin, and Vladimir E. Manucharyan. Millisecond Coherence in a Superconducting Qubit. *Physical Review Letters*, 130(26):267001, Jun 2023. Publisher: American Physical Society.

[74] Zijun Chen, Anthony Megrant, Julian Kelly, Rami Barends, Joerg Bochmann, Yu Chen, Ben Chiaro, Andrew Dunsworth, Evan Jeffrey, Joshua Y. Mutus, Peter J. J. O'Malley, Charles Neill, Pedram Roushan, Daniel Sank, Amit Vainsencher, James Wenner, Theodore C. White, Andrew N. Cleland, and John M. Martinis. Fabrication and characterization of aluminum airbridges for superconducting microwave circuits. *Applied Physics Letters*, 104(5):052602, Feb 2014.

[75] United States. Bureau of Standards. *Bulletin of the Bureau of Standards*. Number v. 4 in Bulletin of the Bureau of Standards. U.S. Government Printing Office, 1908.

[76] A. T. A. M. de Waele. Basic Operation of Cryocoolers and Related Thermal Machines. *Journal of Low Temperature Physics*, 164(5):179–236, Sep 2011.

[77] David M. Pozar. *Microwave Engineering, 4th Edition*. Wiley, 2011.

[78] Howard Wiseman. Complementarity in spontaneous emission: Quantum jumps, staggers and slides. In Howard J. Carmichael, Roy J. Glauber, and Marlan O. Scully, editors, *Directions in Quantum Optics*, pages 347–357, Berlin, Heidelberg, 2001. Springer Berlin Heidelberg.

[79] Zlatko K Minev, Thomas G McConkey, Jeremy Drysdale, Priti Shah, Dennis Wang, Marco Facchini, Grace Harper, John Blair, Helena Zhang, Nick Lanzillo, Sagarika Mukesh, Will Shanks, Chris Warren, and Jay M Gambetta. Qiskit Metal: An Open-Source Framework for Quantum Device Design & Analysis, 2021.

[80] J. S. Douglas, H. Habibian, C.-L. Hung, A. V. Gorshkov, H. J. Kimble, and D. E. Chang. Quantum many-body models with cold atoms coupled to photonic crystals. *Nature Photonics*, 9(5):326–331, apr 2015.

[81] Ruichao Ma, Brendan Saxberg, Clai Owens, Nelson Leung, Yao Lu, Jonathan Simon, and David I. Schuster. A dissipatively stabilized mott insulator of photons. *Nature*, 566(7742):51–57, Feb 2019.